An Approximation for the Twenty-One-Moment Maximum-Entropy Model of Rarefied Gas Dynamics

Fabien Giroux

Thesis submitted to the University of Ottawa
in partial Fulfillment of the requirements for the
Ph.D. in Mechanical Engineering

Mechanical Engineering
University of Ottawa

Abstract

The use of moment-closure methods to predict continuum and moderately rarefied flow offers many modelling and numerical advantages over traditional methods. The maximum-entropy family of moment closures offers models described by hyperbolic systems of balance laws. In particular, the twenty-one moment model of the maximum-entropy hierarchy offers a hyperbolic treatment of viscous flows exhibiting heat transfer. This twenty-one moment model has the ability to provide accurate solutions where the Navier-Stokes equations lose physical validity due to the solution being too far from local equilibrium. Furthermore, its first-order hyperbolic nature offers the potential for improved numerical accuracy as well as a decreased sensitivity to mesh quality. Unfortunately, higher-order maximum-entropy closures cannot be expressed in closed form. The only known affordable option is to propose approximations. Previous approximations to the fourteen-moment maximum-entropy model have been proposed [M^{c}Donald and Torrilhon, 2014]. Although this fourteen-moment model also predicts viscous flow with heat transfer, the necessary moments to close the system renders it more difficult to approximate accurately than the twenty-one moment model. The proposed approximation for the fourteen-moment model also has realizable states for which hyperbolicity is lost.

Unfortunately, the velocity distribution function associated with the twenty-one moment model is an exponential of a fourth-order polynomial. Such a function cannot be integrated in closed form, resulting in closing fluxes that can only be obtained through complex numerical methods. The goal of this work is to present a new approximation to the closing fluxes that respect the maximum-entropy philosophy as closely as possible. Preliminary results show that a proposed approximation is able to provide shock predictions that are in good agreement with the Boltzmann equation and surpassing the prediction of the Navier-Stokes equations. Furthermore, Couette flow results as well as lid-driven cavity flows are computed using a novel approach to Knudsen layer boundary conditions. A dispersion analysis as

well as an investigation of the hyperbolicity of the model is also shown. The Couette flow results are compared against Navier-Stokes and the free-molecular analytical solutions for a varying Knudsen number, for which the twenty-one moment model show good agreement over the domain. The shock-tube problem is also computed for different Knudsen numbers. The results are compared with the one obtained by directly solving the BGK equation. Finally, the lid-driven cavity flow computed with the twenty-one moment model shows good agreement with the direct simulation Monte-Carlo (DSMC) solution.

Contents

List of Figures

Chapter 1

Introduction

In engineering, during the design process, solutions to gas flows are necessary in order to optimize performance and efficiency as well as evaluate design criteria. A theoretical or analytical solution to a given flow of a certain complexity is often not possible without making simple assumptions. That is because of the high complexity of the physics involved, as well as geometry. Conversely, obtaining solutions through experiments, such as the use of wind tunnels, is highly expensive and requires a lot of time and resources, especially if an iterative design strategy is used. The use of computational methods to solve complex gas flows through discretization of governing equations allows one to obtain solutions that can be used in the design process. Doing so allows for a process that is less expensive and can be performed in less time. It also allows for further optimization of performance through auxiliary numerical methods. The efficiency and performance of computational methods depends on the mesh used, the numerical discretization used as well as the choice of governing equations. A less accurate numerical discretization will yield solutions faster but with less accuracy while a more accurate discretization method will yield more accurate solutions but in a more time expensive manner. It is important to choose the proper numerical discretization based on the desired output and the governing equation in used. A proper choice of the governing equations is also important. Depending on the characteristics of the flow and scale of the problem, different physics are needed and the proper governing equation have to be used.

Gas flows can be categorized by the ratio between the length scale of the problem and the distance between inter-particle collisions, known as the mean free path. The Knudsen

number is the non-dimensional number associated with this ratio. In gas flows where the mean free path of particles is much smaller than the length scale of the problem, the Knudsen number is small and the flow regime is described as continuum. Conversely, when the mean free path is much larger than the length scale of the problem, the Knudsen number is large and the flow is considered to be in the rarefied regime. The transition regime contain flows where the mean free path and the length scale of the problem are of similar scales. Gas flows in the transition or rarefied regime are relatively common in engineering or scientific applications. For example, microscale flows, high altitude flight and space capsule re-entry all occur in these regimes. The accurate prediction of gas flow is crucial for these applications. Moderately rarefied gas flow with Knudsen number between 0.1 and 10 are very challenging to predict. For this type of flow, non-equilibrium effect can strongly influence flow behaviour [21]. Particle-based models, such as direct simulation Monte-Carlo (DSMC) [4], and models based on directly solving the Boltzmann equation, such as discrete-velocity methods [33], have had success predicting non-equilibrium flows in strongly rarefied regimes. Unfortunately, these methods often carry a prohibitively expensive computational cost in the transition regime. In particular, DSMC methods exhibit slow convergence and noise in their solutions that is proportional to the speed of sound. This makes DSMC a less suitable method for low speed flows, where the amplitude of the noise is much larger than the scale of the solution. Fortunately, moment-closures offer potential advantages in both the continuum and the rarefied-flow regimes, as compared to existing methods [15, 28, 36]. Moment closures are based on an assumed form of the distribution function describing the phase-space probability distribution of gas particles. The set of partial differential equations (PDEs) associated with moment-closure methods are significantly less expensive to solve then particle-based and direct-discretization methods. Moment-closures offer a set of first-order hyperbolic balance laws that can accurately predict viscous flow with heat-transfer in both the continuum and rarefied regimes. Their first-order nature promise numerical advantages, such as a decreased sensitivity to mesh quality during numerical solution [30]. This is advantageous when dealing with complex geometries that are typical of practical problems. The requirement for the evaluation of only first derivatives also offers the possibility for an extra order of spacial accuracy for a given stencil.

The two most popular families of traditional moment-closure methods are the Grad hierarchy [15] and the maximum-entropy hierarchy [11, 28, 36]. The Grad closures, unfortunately, have a very restricted region of hyperbolicity and are not always robust or accurate enough for flows that are far from equilibrium. The Grad closures are also not guaranteed to predict a strictly positive distribution function describing particle velocities. The maximum-entropy

hierarchy of closures can more robustly give flow predictions that are far from equilibrium and promises a globally hyperbolic system whenever the entropy-maximization problem can be solved. They also guaranteed a strictly positive distribution function. However, the latter hierarchy suffers from two disadvantages. First, the associated distribution function for closures that offer a treatment of viscous flow with heat transfer is an exponential of a fourth-order polynomial. It is impossible to integrate such a function in closed form, leading to the impossibility to obtain the closing fluxes in closed form. A very expensive iterative procedure is needed to compute the closing fluxes at every flux calculation. Such a procedure is far too expensive to yield a practical computational tool. The second issue is that there are physically realizable moment states for which the entropy-maximization problem does not have a solution. In those regions, closing fluxes are singular [23, 24]. Recently, an approximation to the fourteen-moment model, the first model in the maximum-entropy hierarchy capable of predicting heat-transfer, has been proposed by M$^{\text{c}}$Donald and Torrilhon [31]. The closing fluxes are approximated through an interpolation between realizability boundaries with the objective of preserving the hyperbolicity of the model. The use of an approximation substitutes the use of the previously mentioned expensive iterative procedure. Unfortunately, the closing fluxes containing the heat flux tensor are challenging to approximate and the proposed approximation is weak. Even more devastating is that approximations to higher-order closing fluxes are dependent on the weak approximation of the heat flux tensor.

Recently, a number of new families of moment closures have been proposed. Many of these new closures are inspired by either the Grad or maximum-entropy families. For example, Struchtrup and Torrilhon have proposed regularized extensions for the thirteen-moment Grad closure [39]. This technique was further extended to the regularization of Grad's twenty-moment model [34]. These closures aim to extend the physical validity of the Grad closures through the addition of higher-order derivatives at the cost of the hyperbolic, first-order structure. Alternatively, Cai *et al.* have proposed a hyperbolization technique that leads to robustly hyperbolic Grad-style closures at the expense of balance-law form [8, 9]. A similar technique has been explored and applied by Köllermeier and Torrilhon [27]. New quadrature-based moment methods (QBMM) techniques such as HyQMOM have been proposed by Fox, in which quadrature point with associated weights are used to close the system of moments in a manner that preserves hyperbolicity [12]. Finally, the φ-divergence closures, proposed by Abdelmalik and van Brummelen take inspiration from the maximum-entropy hierarchy [1]. The closed-form closures shown in the present work are an approximation to the maximum-entropy closures based on an interpolation technique between realizability boundaries.

1.1 Thesis Goals

The main goal of this thesis is to propose a new three-dimensional approximation for the closing fluxes of the twenty-one-moment closure and present its advantages in approximating this closure over the fourteen-moment closure. The weakness of the fourteen-moment model approximation stems from the lack of information known regarding the closing flux containing the heat-flux tensor. The twenty-one moment model contains all entries of the heat-flux tensor in its solution vector and therefore no approximation of this term is needed. The trade-off is that more entries of higher-order tensors need to be approximated. However, more information is also known about them. The evaluation of the success of the proposed approximation is done through a study of the regions of hyperbolicity as well as a dispersion analysis of the resulting equations. The development of a novel treatment of solid-wall boundary condition is another objective of this work. The performance and accuracy of the model is tested through the simulation of multi-dimensional cases for the first time and compared against classical methods.

1.2 Thesis Structure

This work presents a review of kinetic theory and moment closures for gases, focusing on the maximum-entropy hierarchy of moment-closures. Following this is an overview of the previously proposed fourteen-moment closure by M^{c}Donald and Torrilhon [31], discussing its limited ability in approximating the closing fluxes, in particular issues are identified with the heat-flux tensor. Then a presentation of the newly proposed approximation for the twenty-one moment model with a study of its realizability space, its hyperbolicity, as well as a dispersion analysis. A new approach to solid wall boundary condition for moment methods in general is proposed as well. Finally, numerical results are presented to support the evaluation of the performance of the proposed model.

Chapter 2

Kinetic Theory and Moment Closure

2.1 The Knudsen Number

In traditional fluid mechanics models, the fluid is generally assumed to be continuum. This assumption is valid granted that the scale of the problem being solved is much greater than the scale of the inter-particles interactions. In this case, the inter-particles interaction occur on such a small scale that they "average out" over the scale of the problem. The fluid can then be treated as a continuum, since there is no need to track particles individually. In the event where the length scale of the problem is of similar or smaller scale than the inter-particles interaction, then, the assumption of continuum cannot be used. In such case, the microscopic structure of the fluid needs to be considered to properly model the flow.

The Knudsen number is used to characterize the regime of the problem. It is defined to be the ratio of mean free path of a particle, λ, and the characteristic length of the problem,

$$\mathrm{Kn} = \frac{\lambda}{l}\,. \tag{2.1}$$

The correlation between the Knudsen number and the flow regimes is shown in Figure 2.1. In the continuum regime, the length scale of the particle interaction is small compared to the scale of the problem and classical fluid-mechanic models, such as the Navier-Stokes equations, are valid. In the free-molecular regime, the scale of the particle interaction is much larger

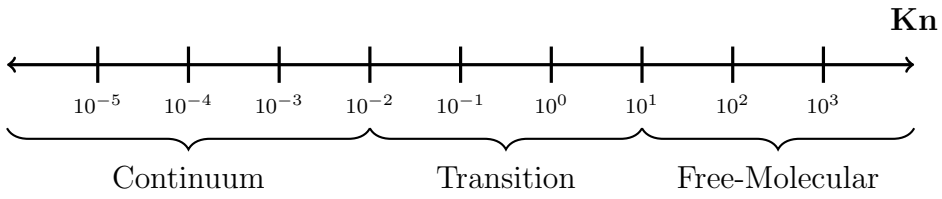

Figure 2.1: Flow regimes with respect to the Knudsen number

than the scale of the problem. In the absence of acceleration fields, particles travel in straight lines without interacting with each other. While classical methods cannot predict flows in this regime it is often affordable to do so through particle-based methods [4]. In the transition regime, the scale of the particle interaction becomes comparable to the length scale of the problem. In this case, the inter-particle interaction are important in the prediction of the flow, yet classical method cannot reliably predict the solution. While particle-based methods can accurately predict flows in this regime, they can become prohibitively expensive when a large number of particles are present. This is especially true for low-speed flows. Moment-closure methods offer a good alternative in accurately predicting flows in this regime.

2.2 The Distribution Function

In the kinetic theory of gases, a statistical representation of the gas is used. Instead of tracking every single particle in space, a velocity distribution function, $\mathcal{F}(x_i, v_i, t)$, is used. This function describes the phase-space density of particles in the neighborhood of a position, x_i, with a velocity, v_i, at a time, t. The most commonly known distribution function is the Maxwell-Boltzmann distribution,

$$\mathcal{M} = \frac{\rho}{m}\left(\frac{\rho}{2\pi p}\right)^{\frac{3}{2}} \exp\left(-\frac{\rho}{2p}(v_i - u_i)(v_i - u_i)\right), \tag{2.2}$$

where ρ is the mass density of the gas, p is the pressure, m is the particle mass, u_i is the flow bulk velocity and v_i is the particle velocity. The random velocity, $c_i = v_i - u_i$, is defined as the difference between the particle velocity and the local flow bulk velocity. The Maxwell-Boltzmann distribution statistically represent gases that are in local equilibrium. It can be shown that any distribution of particles will be driven toward the Maxwell-Boltzmann distribution by inter-particle collision. Once the Maxwell-Boltzmann distribution is reached, the inter-particle collisions no longer have an effect on the form of the distribution function.

For non-equilibrium gases, the associated distribution function can vastly differ from the Maxwell-Boltzmann distribution.

It is possible to relate traditional macroscopic properties to the distribution function describing a gas by taking velocity moments of the distribution. This is done by multiplying the distribution function by a velocity weight and integrating over all velocity space. For example,

$$\begin{aligned} \rho &= \iiint_{\infty} m\mathcal{F} dv_i = \langle m\mathcal{F} \rangle \ , \\ \rho u_i &= \langle m v_i \mathcal{F} \rangle \ , \\ P_{ij} &= \langle m c_i c_j \mathcal{F} \rangle \ , \\ Q_{ijk} &= \langle m c_i c_j c_k \mathcal{F} \rangle \ , \\ R_{ijkl} &= \langle m c_i c_j c_k c_l \mathcal{F} \rangle \ , \\ S_{ijklm} &= \langle m c_i c_j c_k c_l c_m \mathcal{F} \rangle \ . \end{aligned} \tag{2.3}$$

Here, $P_{ij} = p\delta_{ij} - \tau_{ij}$ represent the anisotropic pressure tensor, defined as the difference between the thermodynamic pressure, p, and the deviatoric stresses, τ_{ij}. For monatomic gases, the thermodynamic pressure is obtained by averaging the diagonal entries of the anisotropic pressure tensor, $p = P_{ii}/3$. The third-order tensor, Q_{ijk}, is the generalized heat-flux tensor. The classical heat-flux in a given direction is equivalent to half of the corresponding trace of the heat-flux tensor, $q_i = \frac{1}{2}Q_{ijj}$. For convenience, the notation $\langle\ \rangle$ is used to represent the integral over all velocity space. Higher-order moments, such as R_{ijkl} and S_{ijklm}, do not have any familiar physical meaning, but represent local high-order statistics of particles velocities. In this way, moments of any arbitrary order can be defined.

The moments obtained using the full particle velocity, v_i, as velocity weights are referred to as full moments. Similarly, moments obtained using the random velocity, c_i, as velocity weights are referred to as random moments. The two can be correlated by using the expression for the random velocity. For example, the full uncontracted second order moment can be correlated to the random second order moment,

$$\begin{aligned} \langle m v_i v_j \mathcal{F} \rangle &= \langle m \left(u_i + c_i\right) \left(u_j + c_j\right) \mathcal{F} \rangle \\ &= \langle m u_i u_j \mathcal{F} \rangle + \cancelto{0}{\langle m u_i c_j \mathcal{F} \rangle} + \cancelto{0}{\langle m c_i u_j \mathcal{F} \rangle} + \langle m c_i c_j \mathcal{F} \rangle \\ &= \rho u_i u_j + P_{ij} \ . \end{aligned}$$

2.3 The Boltzmann Equation

The time evolution of the distribution function is governed by the Boltzmann equation,

$$\frac{\partial \mathcal{F}}{\partial t} + v_i \frac{\partial \mathcal{F}}{\partial x_i} + \frac{\partial \left(a_i \mathcal{F}\right)}{\partial v_i} = \frac{\delta \mathcal{F}}{\delta t} \,. \tag{2.4}$$

The three terms on the left-hand side, represent the time evolution of the distribution function, the effect of particles convection and the effect of acceleration forces on the dristribution function, respectively, in their order of appearance. The term on the right-hand side of Eq. (2.4) is the collision operator, which models the effect of inter-particles interaction on the distribution function. By assuming that the collisions are only binary collisions of identical particles, that these collisions are occurring on a scale that is much smaller than the mean free path of the particles and by assuming that a single collision does not noticeably affect the distribution function and that, finally, particles velocities are statistically independent, it is possible to express the collision term as,

$$\frac{\delta \mathcal{F}}{\delta t} = \left\langle \int_0^{2\pi} \int_0^{\pi} \left(\mathcal{F}' \mathcal{F}_1' - \mathcal{F} \mathcal{F}_1\right) g \sigma \sin\chi d\chi d\epsilon \right\rangle_{v_i'} \,. \tag{2.5}$$

In this integral, $\mathcal{F}$ and $\mathcal{F}_1$ are the distribution functions of the two particles undergoing a collision at particle velocities v_i and v_{1i}, while $\mathcal{F}'$ and $\mathcal{F}_1'$ are the distribution functions of the two particles post collision with particle velocities v_i' and v_{1i}'. The particles relative speed pre-collision is expressed as $g = |v_i - v_{1i}|$, σ is the differential collision cross-section, χ is the deflection angle and finally ϵ is a solid angle integrated around a particle undergoing collisions [38, 14].

The expression shown in Eq. (2.5) contains a high-dimensional integral and usually cannot be evaluated in closed form. However, it is known to conserve mass, momentum and energy, and to increase the entropy monotonically until the distribution function becomes a Maxwellian. For many applications, it is possible to use a simplifying approximation to the collision operator, such as the relaxation-time BGK model, as first proposed by Bhatnagar *et al.* [3],

$$\frac{\delta \mathcal{F}}{\delta t} = -\frac{\mathcal{F} - \mathcal{M}}{\tau} \,, \tag{2.6}$$

where τ is a characteristic relaxation time and $\mathcal{M}$ is the Maxwell-Boltzmann distribution with the same mass, momentum and energy densities. The BGK model moves the distribution

function, $\mathcal{F}$, towards equilibrium at a time scale, τ. The time scale, τ, is correct in the case where $\mathrm{Kn} \to 0$ and $\mathrm{Kn} \to \infty$, but is only approximate for everything in between.

The collision term can be shown to satisfy the second law of thermodynamics by taking a moment of the Boltzmann equation using the velocity weight,

$$M = -k \ln \frac{\mathcal{F}}{y}\,, \tag{2.7}$$

leading to,

$$\frac{\partial}{\partial t}\left\langle -k \ln \frac{\mathcal{F}}{y}\mathcal{F} \right\rangle + \frac{\partial}{\partial x_i}\left\langle -k \ln \frac{\mathcal{F}}{y} v_i \mathcal{F} \right\rangle + \frac{\partial}{\partial v_i}\left\langle -k \ln \frac{\mathcal{F}}{y} a_i \mathcal{F} \right\rangle = \left\langle -k \ln \frac{\mathcal{F}}{y} \frac{\delta \mathcal{F}}{\delta t} \right\rangle . \tag{2.8}$$

By neglecting the acceleration and further defining the variable $S = \left\langle -k \ln \frac{\mathcal{F}}{y}\mathcal{F} \right\rangle$, $\Psi_i = \left\langle -k \ln \frac{\mathcal{F}}{y} v_i \mathcal{F} \right\rangle$ and by defining the production term on the right hand side to be Φ, the expression can be written as,

$$\frac{\partial S}{\partial t} + \frac{\partial \Psi_i}{\partial x_i} = \Phi\,. \tag{2.9}$$

By further assuming an isolated system where the flux of S is therefore zero and the equation transforms to,

$$\frac{\partial S}{\partial t} = \Phi\,. \tag{2.10}$$

By observation of the production term, Φ, after substituting Eq. (2.5) into the right-hand side of Eq. (2.8), it can be seen that it is always greater than zero,

$$\Phi = \frac{k}{4}\left\langle \left\langle \int_0^{2\pi}\int_0^{\pi} \ln \frac{\mathcal{F}'\mathcal{F}_1'}{\mathcal{F}\mathcal{F}_1} \left(\mathcal{F}'\mathcal{F}_1' - \mathcal{F}\mathcal{F}_1\right) g\sigma \sin\chi d\chi d\epsilon \right\rangle_{v_i'} \right\rangle_{v_i} \geq 0\,, \tag{2.11}$$

since g and σ are always greater than zero, χ is non zero for the integration interval $0 \leq \chi \leq \pi$ and the terms $\frac{\mathcal{F}'\mathcal{F}_1'}{\mathcal{F}\mathcal{F}_1}$ and $(\mathcal{F}'\mathcal{F}_1' - \mathcal{F}\mathcal{F}_1)$ are only negative at the same time. In fact, S represent the entropy and if the production term, Φ is always greater than zero in Eq. (2.10), then entropy is always generated and the second law of thermodynamics is satisfied [5].

2.4 Maxwell's Equation of Change

Even with the simplified collision operator, the Boltzmann equation remains very high dimensional, with three dimensions in physical space, three dimensions in velocity and one time dimension. Directly solving this equation requires numerical discretization in physical space and in velocity space, resulting in a prohibitively expensive method. Fortunately, for most practical problems, the wealth of information given by solving the Boltzmann equation is not necessary. In most case, it is sufficient to only solve for a desired set of macroscopic properties that are of interest. A vector, $\boldsymbol{W}$, is defined to contain the velocity weights associated with the macroscopic properties of interest. The solution vector, $\boldsymbol{U}$, contain the macroscopic properties of interest such that,

$$\boldsymbol{U} = \langle m\boldsymbol{W}\mathcal{F} \rangle \ .$$

A set of equations for the macroscopic properties, or moments, of interest can be derived by taking velocity moments of the Boltzmann equation.

$$\left\langle m\boldsymbol{W}(v_i) \left(\frac{\partial \mathcal{F}}{\partial t} + v_i \frac{\partial \mathcal{F}}{\partial x_i} + \frac{\partial \left(a_i \mathcal{F} \right)}{\partial v_i} \right) \right\rangle = \left\langle m\boldsymbol{W}(v_i) \frac{\delta \mathcal{F}}{\delta t} \right\rangle \ .$$

In this work the particle acceleration, a_i, is taken to be zero due to the absence of external fields acting on the particles, however, it can be easily incorperated. The collision term is also substituted by the BGK model shown in Eq. (2.6),

$$\left\langle m\boldsymbol{W}(v_i) \left(\frac{\partial \mathcal{F}}{\partial t} + v_i \frac{\partial \mathcal{F}}{\partial x_i} \right) \right\rangle = \left\langle -m\boldsymbol{W}(v_i) \frac{\mathcal{F} - \mathcal{M}}{\tau} \right\rangle \ .$$

Since the particle velocity, v_i, is independent of the location in space, x_i, and since the velocity weight vector is strictly a function of the particle velocity, both can be put into the derivative. Doing so result in Maxwell's equation of change,

$$\frac{\partial}{\partial t} \langle m\boldsymbol{W}(v_i)\mathcal{F} \rangle + \frac{\partial}{\partial x_i} \langle m v_i \boldsymbol{W}(v_i)\mathcal{F} \rangle = -\frac{1}{\tau} \left[\langle m\boldsymbol{W}(v_i)\mathcal{F} \rangle - \langle m\boldsymbol{W}(v_i)\mathcal{M} \rangle \right] \ . \tag{2.12}$$

The number of equation in the system is the same as the size of the velocity weight vector, or as the number of macroscopic properties of interest. For simplicity, Eq. (2.12) is often written as,

$$\frac{\partial \boldsymbol{U}}{\partial t} + \frac{\partial \boldsymbol{F_i}}{\partial x_i} = \boldsymbol{S} \, , \tag{2.13}$$

where $\boldsymbol{U}$ is the solution vector, $\boldsymbol{F_i}$ is the flux, and $\boldsymbol{S}$ is the collision source term.

By using the chain rule, Eq. (2.13) can be rewritten as,

$$\frac{\partial \boldsymbol{U}}{\partial t} + \frac{\partial \boldsymbol{F_i}}{\partial \boldsymbol{U}} \frac{\partial \boldsymbol{U}}{\partial x_i} = \boldsymbol{S}\,, \tag{2.14}$$

where $\frac{\partial \boldsymbol{F_i}}{\partial \boldsymbol{U}}$ is the flux Jacobian. The eigenvalues of the flux Jacobian correspond to the wavespeeds of the system of PDEs. If the eigenvalues of the Jacobian are strictly real, then the system is said to be hyperbolic and information propagates at finite speeds.

2.5 Moment Closure

Unfortunately, taking velocity-moment of the Boltzmann equation cannot naturally lead to a closed system of equations. This is because the time evolution of a given moment always depends on the spacial divergence of a moment that is one order higher in velocity. Also, the collision operator is not always closed. An infinite number of moment equation would therefore be needed to produce a closed system.

One method used to obtain a closed system of equation is to assume the form of the distribution function. This allows one to relate the higher-order moments to the lower-order moments of interest. This assumed distribution function must have the same number of free parameters, $\boldsymbol{\alpha}$, as there are moments in the solution vector (macroscopic properties of interest). The free parameters are chosen so that they are in agreement with the known moments of interest, as given by Eq. (2.3). It then becomes possible to integrate the closing fluxes, since the distribution function is now known. The obtained closing fluxes naturally become a function of the known moments.

2.5.1 The Euler Equations

The well-known compressible Euler equations describe inviscid, adiabatic gas flows. As an illustrative example, they are described here in the moment-closure framework. A set of five moment equations can be obtained by using the generating velocity weight vector,

$\boldsymbol{W}(v_i) = [1, v_i, v_i v_i]$,

$$\frac{\partial}{\partial t}\langle m\mathcal{F}\rangle + \frac{\partial}{\partial x_i}\langle mv_i\mathcal{F}\rangle = -\frac{1}{\tau}\left[\langle m\mathcal{F}\rangle - \langle m\mathcal{M}\rangle\right] , \tag{2.15}$$

$$\frac{\partial}{\partial t}\langle mv_i\mathcal{F}\rangle + \frac{\partial}{\partial x_j}\langle mv_iv_j\mathcal{F}\rangle = -\frac{1}{\tau}\left[\langle mv_i\mathcal{F}\rangle - \langle mv_i\mathcal{M}\rangle\right] , \tag{2.16}$$

$$\frac{\partial}{\partial t}\langle mv_iv_i\mathcal{F}\rangle + \frac{\partial}{\partial x_j}\langle mv_iv_iv_j\mathcal{F}\rangle = -\frac{1}{\tau}\left[\langle mv_iv_i\mathcal{F}\rangle - \langle mv_iv_i\mathcal{M}\rangle\right] . \tag{2.17}$$

Note that the number of velocity weights is equal to the number of unknown in the Maxwellian which are ρ, u_i and p. By using the relations between the macroscopic properties and the velocity moments of the distribution function, the previous set of equations can be rewritten in terms of the properties of interest,

$$\frac{\partial}{\partial t}\left[\rho\right] + \frac{\partial}{\partial x_i}\left[\rho u_i\right] = 0 , \tag{2.18}$$

$$\frac{\partial}{\partial t}\left[\rho u_i\right] + \frac{\partial}{\partial x_j}\left[\rho u_iu_j + P_{ij}\right] = 0 , \tag{2.19}$$

$$\frac{\partial}{\partial t}\left[\rho u_iu_i + P_{ii}\right] + \frac{\partial}{\partial x_j}\left[\rho u_iu_iu_j + 2u_iP_{ij} + u_jP_{ii} + Q_{jii}\right] = -\frac{P_{ii} - 3p}{\tau} . \tag{2.20}$$

At this point, a form of the distribution has not been chosen. Equations (2.18) to (2.20) are true in general. As explained previously, the spacial divergence term in Eqs. (2.16) and (2.17) or Eqs. (2.19) and (2.20) contains moments, P_{ij} and Q_{jii}, that are not part of the known properties of interest and therefore render the system unclosed. The system can be closed by choosing a form for the distribution function, relating the closing moment to the lower-order moments, that are known. If one chooses the distribution function to be the exponential of a second-order polynomial,

$$\mathcal{F} = e^{\alpha_0 + \alpha_i v_i + \beta v_i v_i} , \tag{2.21}$$

then the number of free-coefficient is equal to the number of unknown in the Euler equation. The reason for this choice of form of the distribution function will become apparent in further sections. The free-coefficients can be obtained by solving the following equations relating the macroscopic properties of interest to the weighted integrals of the distribution function,

$$\rho = \langle m\mathcal{F}\rangle ,$$
$$\rho u_i = \langle mv_i\mathcal{F}\rangle ,$$

$$\rho u_i u_i + 3p = \langle m v_i v_i \mathcal{F} \rangle \ ,$$

yielding,

$$\begin{aligned}
\alpha_0 &= \ln\left[\frac{\rho}{m}\left(\frac{\rho}{2p\pi}\right)^{\frac{3}{2}}\right] - \frac{\rho}{2p} u_i u_i \,, \\
\alpha_i &= \frac{\rho u_i}{p} \,, \\
\beta &= -\frac{\rho}{2p} \,.
\end{aligned}$$

By substituting the obtained values for α_0, α_i and β into Eq. (2.21) the Maxwell-Boltzmann distribution is obtained. By using this distribution to calculate the closing fluxes, the well-known Euler equations for a monatomic gas are recovered,

$$\frac{\partial}{\partial t}\left[\rho\right] + \frac{\partial}{\partial x_i}\left[\rho u_i\right] = 0 \tag{2.22}$$

$$\frac{\partial}{\partial t}\left[\rho u_i\right] + \frac{\partial}{\partial x_j}\left[\rho u_i u_j + p\delta_{ij}\right] = 0 \tag{2.23}$$

$$\frac{\partial}{\partial t}\left[\rho u_i u_i + 3p\right] + \frac{\partial}{\partial x_j}\left[\rho u_i u_i u_j + 5p u_j\right] = 0 \,. \tag{2.24}$$

Here, Eq. (2.24) is double the traditional energy equation. It is written this way for consistency with other closures shown in this work. As known, the Euler equations are only valid for inviscid flows with no heat-transfer. This demonstrate the need of a more complex distribution function with a larger associated velocity weight vector in order to model more macroscopic properties, such as viscosity and heat transfer.

2.5.2 Choice of The Distribution Function

There exist a large variety of techniques related to the choice of the distribution function. The next sections discusses some of the most common techniques proposed. The choice of technique used directly impacts the system of moment equations that will be obtained. Some traditional techniques, like the Grad closure, are based on distribution functions that are a perturbation around a Maxwellian. Alternatively, the maximum-entropy technique relies on using the distribution function that maximizes the entropy, a measure of likelihood, of the distribution. Some more recent techniques, such as the ϕ-divergences technique, are

inspired by the maximum-entropy closure and are based around an approximation method. Finally, some more contrasting methods are based on weighted quadratures method to yield a distribution function.

2.5.3 The Grad Closure

The most well-known hierarchy of moment closures is the Grad closures [15]. For these closures, the proposed distribution function consist of a Hermite polynomial expansion around the Maxwellian,

$$\mathcal{F} = (\alpha_0 H_0 + \alpha_i H_i + \alpha_{ij} H_{ij} + \cdots)\,\mathcal{M}\,. \tag{2.25}$$

That is, the distribution function is assumed to be a polynomial expansion around an equilibrium Maxwellian. This Maxwellian may be a "global", constant distribution or may be the Maxwellian with the local density, bulk velocity, and pressure. In Eq. (2.25), $[\alpha_0, \alpha_i, \alpha_{ij}, \cdots]$ are the coefficients and are dependent on space and time, while $[H_0, H_i, H_{ij}, \cdots]$ are Hermite polynomials. These polynomials are defined as,

$$H_{i_1,i_2,\cdots,i_N} = \frac{1}{\mathcal{M}} \frac{\partial^N}{\partial c_{i_1} \partial c_{i_2} \cdots \partial c_{i_N}} \mathcal{M}\,, \tag{2.26}$$

where N is the order of the polynomial. If a global Maxwellian is used, these polynomials will be constant. If the Maxwellian adapts to the local gas condition, so will the Hermite polynomials. These polynomials form an orthogonal basis with respect to the Maxwellian distribution function, that is

$$\iiint_{\infty} H_{i_1,i_2,\cdots,i_N}(c_i) H_{i_1,i_2,\cdots,i_M}(c_i) \mathcal{M}(c_i) dc_x dc_y dc_z = 0\,, \tag{2.27}$$

when the Hermite polynomials are different. The Hermite polynomial H_0 is equal to 1. The coefficients multiplying the Hermite polynomials, $\boldsymbol{\alpha}$, are chosen so that the distribution function is consistent with the moments of interest. The number of polynomial/coefficient must be equal to the number of moments of interest. The first four Hermite polynomials have the form

$$H_0 = 1\,, \tag{2.28}$$

$$H_i = -\frac{\rho}{p} c_i \,, \tag{2.29}$$

$$H_{ij} = \frac{\rho^2}{p^2} c_i c_j - \frac{\rho}{p} \delta_{ij} \,, \tag{2.30}$$

$$H_{ijj} = -\frac{\rho^3}{p^3} c_i c_j c_j + 5 \frac{\rho^2}{p^2} c_i \,. \tag{2.31}$$

If the moments of interest are $\boldsymbol{V} = [\rho, u_i, p]$, which are the moments corresponding to the Euler equation, then the following Grad distribution function with the Hermite polynomial H_0, H_i and H_{ii} is obtained,

$$\mathcal{F} = \left(\alpha_0 - \alpha_i \frac{\rho}{p} c_i + \alpha_{ii} \left(\frac{\rho^2}{p^2} c_i c_i - 3 \frac{\rho}{p} \right) \right) \mathcal{M} \,. \tag{2.32}$$

The coefficients α_0, α_i and α_{ii} need to be found so that the moments of interest of the distribution function are satisfied. This leads to

$$\alpha_0 = 1 \,, \tag{2.33}$$

$$\alpha_i = 0 \,, \tag{2.34}$$

$$\alpha_{ii} = 0 \,. \tag{2.35}$$

The resulting distribution function is simply the Maxwellian shown earlier. When using this distribution, the Euler equations are again recovered. This shows that the Euler equations are the lowest-order member of the Grad hierarchy of closures. To model a wider set of macroscopic properties, more Hermite polynomials and closure coefficients are required. The Grad 13-moment closure has the ability to model viscous stresses and heat-transfer. This distribution has the general form,

$$\mathcal{F}_{G13} = \left(\alpha_0 + \alpha_i H_i + \alpha_{ij} H_{ij} + \alpha_{ijj} H_{ijj} \right) \mathcal{M} \,, \tag{2.36}$$

where the system of equations is generated using the velocity weight vector $\boldsymbol{W} = [1, v_i, v_i v_j, v_i v_j v_j]$. The corresponding moments of interest are $\boldsymbol{V} = [\rho, u_i, P_{ij}, Q_{ijj}]$. In this case, the obtained coefficients are,

$$\alpha_0 = 1 \,, \tag{2.37}$$

$$\alpha_i = 0 \,, \tag{2.38}$$

$$\alpha_{ij} = \frac{P_{ij} - p\delta_{ij}}{2\rho}\,, \tag{2.39}$$

$$\alpha_{ijj} = -\frac{Q_{ijj}}{10\rho}\,, \tag{2.40}$$

when this distribution function is inserted into Maxwell's equation of change, a set of thirteen PDEs is obtained,

$$\frac{\partial}{\partial t}\left[\rho\right] + \frac{\partial}{\partial x_i}\left[\rho u_i\right] = 0 \tag{2.41}$$

$$\frac{\partial}{\partial t}\left[\rho u_i\right] + \frac{\partial}{\partial x_j}\left[\rho u_i u_j + P_{ij}\right] = 0 \tag{2.42}$$

$$\begin{aligned}&\frac{\partial}{\partial t}\left[\rho u_i u_j + P_{ij}\right] \\ &+ \frac{\partial}{\partial x_k}[\rho u_i u_j u_k + u_i P_{jk} + u_j P_{ik} + u_k P_{ij} \\ &\quad + \frac{1}{5}\left(Q_{ill}\delta_{jk} + Q_{jll}\delta_{ik} + Q_{kll}\delta_{ij}\right)] = -\frac{3P_{ij} - P_{kk}\delta_{ij}}{3\tau}\end{aligned} \tag{2.43}$$

$$\begin{aligned}&\frac{\partial}{\partial t}\left[\rho u_i u_j u_j + u_i P_{jj} + 2u_j P_{ij} + Q_{ijj}\right] \\ &+ \frac{\partial}{\partial x_k}\Bigg[\rho u_i u_j u_j u_k + 2u_i u_j P_{jk} + u_i u_k P_{jj} + u_j u_j P_{ik} + 2u_j u_k P_{ij} \\ &\quad + u_i Q_{kjj} + u_k Q_{ijj} + 2u_j \frac{1}{5}\left(Q_{ill}\delta_{jk} + Q_{jll}\delta_{ik} + Q_{kll}\delta_{ij}\right) + \left(7\frac{p}{\rho}P_{ik} - 2\frac{p^2}{\rho}\delta_{ik}\right)\Bigg] \\ &\quad = -\frac{3Q_{ijj} + 2\left(3P_{ik}u_k - P_{kk}u_i\right)}{3\tau}\end{aligned} \tag{2.44}$$

The first equation is simply the conservation of mass, the following three are the conservation of momentum. The next six describe the conservation of energy decomposed in modes associated with different directions. Finally the last three describe the evolution of the energy flux, including the heat transfer tensor.

Although Grad's technique yield a closed set of locally hyperbolic equations, the assumed distribution function is not guaranteed to be positive. Because the polynomial multiplying the Maxwellian could be negative, the distribution could show a negative probability for some particle velocities, which is not physical. Furthermore, there are realizable moments arbitrarily close to equilibrium for which the closed system of equation is not hyperbolic [10]. This happens when the eigenvalues of the corresponding flux Jacobian are complex. Consequently, the system is ill-posed and a solution is not guaranteed. Finally, the addition

of more polynomials and closure coefficient does not necessarily translate to a system of equation yielding more accurate solution [43].

2.5.4 The φ-Divergences Closure

A more recent closure inspired from the maximum-entropy hierarchy has been proposed by Abdelmalik and van Brummelen [1]. The φ-divergences closure is based on an approximation of the exponential function. The standard limit definition for the exponential is expressed as,

$$\exp(f) = \lim_{n\to\infty}\left(1+\frac{f}{n}\right)^n \approx \left(1+\frac{f}{N}\right)^N , \tag{2.45}$$

where f is an arbitrary function. Unfortunately, in the limit where $v \to \pm\infty$, the truncated exponential and its derivatives do not decay to zero. This is essential in order to obtain finite macroscopic properties. Furthermore, for values of N that are odd, the truncated exponential can possibly be negative. To preserve the properties mentioned above, a modified approximation of the exponential is required. One such approximation is the q-exponential [44],

$$\widetilde{\exp}_q(f) = [1+(1-q)f]_+^{1/(1-q)} , \tag{2.46}$$

where $q \neq 1$ and $[f]_+ = \frac{1}{2}f + \frac{1}{2}|f|$ is the non-negative part of a function. The q-exponential and the truncated limit definition of the exponential are related when $1-q = \frac{1}{N}$,

$$\widetilde{\exp}_q(f) = \left[1+\frac{f}{N}\right]_+^N . \tag{2.47}$$

The proposed distribution function for the φ-divergences closure is

$$\mathcal{F}_N = \mathcal{M}\ \widetilde{\exp}_q(\boldsymbol{\alpha}^{\boldsymbol{T}}\boldsymbol{W}) = \mathcal{M}\left(1+\frac{\boldsymbol{\alpha}^{\boldsymbol{T}}\boldsymbol{W}}{N}\right)_+^N , \tag{2.48}$$

where $\boldsymbol{\alpha}$ and $\boldsymbol{W}$ are the free coefficient and the velocity weights respectively and $\mathcal{M}$ is a Maxwellian distribution that pre-factors the q-exponential approximation. Pre-factoring by a Maxwellian ensure a decay to zero of the distribution function as $v \to \pm\infty$. While this pre-factored Maxwellian is independent of the moments it can be dependent on space and time. The independence of the Maxwellian on the moments preserve the symmetry of the flux Jacobian and the hyperbolicity of the system. The values for the free-coefficients, $\boldsymbol{\alpha}$, are found by performing a Newton search using the moments. This closure leads to a

hyperbolic set of equations with a strictly positive distribution function. This is nice because it is a "bridge" between Grad and Maximum-Entropy. When a value of $N = 1$ is chosen, a Grad distribution is recovered. Conversely, when a value of $N \to \infty$ is chosen, the resulting distribution function correspond to the one that maximizes entropy.

2.5.5 Quadrature-Based Moment Methods

Another technique to close a system of moment equations, is quadrature-based moment closure. Quadrature-based methods were first introduced by McGraw [32] in the context of aerosol dynamics description. Since then, Fox has developed more advanced quadrature method of moments (QMOM) for both one-dimensional and multi-dimensional distributions [29]. This method is based on the approximation of the velocity distribution function by a set of weighted quadrature points,

$$\mathcal{F} \approx \sum_{\gamma=1}^{N} \omega_\gamma \delta(v_i - \xi_{\gamma,i}) \,, \tag{2.49}$$

where $\xi_{\gamma,i}$ is the location of the γ^{th} quadrature point in velocity space and ω_γ is its associated weight. This allows one to express moments of the distribution function as a weighted sum of all quadrature points,

$$\langle mw(v_i)\mathcal{F} \rangle \approx \sum_{\gamma=1}^{N} mw(\xi_{\gamma,i})\omega_\gamma \,. \tag{2.50}$$

A choice for the number and location of quadrature points must be done, the technique involved to do so for one-dimensional distributions differs vastly from the one used for multi-dimensional distributions.

One-Dimensional Quadrature-Based Distribution Functions

For one-dimensional distribution functions, the number of quadrature points needed is directly related to the number of known macroscopic moments. In order to use N quadrature points, one needs $2N$ moments, since there is $2N$ unknowns, N quadrature locations and N

associated weights. It is possible to write a set of $2N$ equations for this relation,

$$U_i = \left\langle m v^i \mathcal{F} \right\rangle = \sum_{\gamma=1}^{N} m \omega_\gamma \xi_\gamma^i \,. \tag{2.51}$$

However, solving these relations directly has proven challenging due to the high degree of some of the polynomials. One approach to solving for the locations of the quadratures and their weights is to first define the following matrices,

$$\boldsymbol{H} = \begin{bmatrix} U_0 & U_1 & \cdots & U_{N-1} \\ U_1 & U_2 & \cdots & U_N \\ \vdots & \vdots & \ddots & \vdots \\ U_{N-1} & U_N & \cdots & U_{2N-2} \end{bmatrix} \quad \text{and} \quad \boldsymbol{J} = \begin{bmatrix} U_1 & U_2 & \cdots & U_N \\ U_2 & U_3 & \cdots & U_{N+1} \\ \vdots & \vdots & \ddots & \vdots \\ U_N & U_{N+1} & \cdots & U_{2N-1} \end{bmatrix} , \tag{2.52}$$

which are composed of the $2N$ known moments and are both symmetric. It is possible to rewrite these matrices as,

$$\boldsymbol{H} = \boldsymbol{R}\boldsymbol{W}\boldsymbol{R}^T \quad \text{and} \quad \boldsymbol{J} = \boldsymbol{R}\boldsymbol{\Lambda}\boldsymbol{W}\boldsymbol{R}^T \,, \tag{2.53}$$

where the matrix $\boldsymbol{R}$ is defined as

$$\boldsymbol{R} = \begin{bmatrix} 1 & 1 & \cdots & 1 \\ \xi_0 & \xi_1 & \cdots & \xi_{N-1} \\ \xi_0^2 & \xi_1^2 & \cdots & \xi_{N-1}^2 \\ \vdots & \vdots & \ddots & \vdots \\ \xi_0^{N-1} & \xi_1^{N-1} & \cdots & \xi_{N-1}^{N-1} \end{bmatrix} , \tag{2.54}$$

and where the diagonal matrices $\boldsymbol{W}$ and $\boldsymbol{\Lambda}$ are defined as

$$\boldsymbol{W} = \begin{bmatrix} w_1 & 0 & \cdots & 0 \\ 0 & w_2 & \cdots & 0 \\ \vdots & \vdots & \ddots & \vdots \\ 0 & 0 & \cdots & w_{N-1} \end{bmatrix} \quad \text{and} \quad \boldsymbol{\Lambda} = \begin{bmatrix} \xi_0 & 0 & \cdots & 0 \\ 0 & \xi_1 & \cdots & 0 \\ \vdots & \vdots & \ddots & \vdots \\ 0 & 0 & \cdots & \xi_{N-1} \end{bmatrix} . \tag{2.55}$$

The expressions shown in Eq. (2.53) are just the matrix form of the equation shown in Eq. (2.51). By multiplying the matrix $\boldsymbol{J}$ by the inverse of matrix $\boldsymbol{H}$ it is possible to obtain an expression where the weights, w_α, are not present. This makes it possible to solve directly

for the location of the quadrature points without knowing the associated weights.

$$\begin{aligned}\boldsymbol{J}\boldsymbol{H}^{-1} &= \boldsymbol{R}\boldsymbol{\Lambda}\boldsymbol{W}\boldsymbol{R}^{T}\left(\boldsymbol{R}\boldsymbol{W}\boldsymbol{R}^{T}\right)^{-1} \\ &= \boldsymbol{R}\boldsymbol{\Lambda}\boldsymbol{W}\boldsymbol{R}^{T}\boldsymbol{R}^{-T}\boldsymbol{R}^{-1}\boldsymbol{W}^{-1} \\ &= \boldsymbol{R}\boldsymbol{\Lambda}\boldsymbol{R}^{-1}\,, \end{aligned} \tag{2.56}$$

where $\boldsymbol{R}$ and $\boldsymbol{R}^{-1}$ would be the right and left eigenvectors of the $\boldsymbol{J}\boldsymbol{H}^{-1}$ matrix respectively while $\boldsymbol{\Lambda}$ would be the eigenvalues. It is then possible to find the quadrature points since their locations correspond to the eigenvalues of the obtained matrix,

$$\det(\boldsymbol{J}\boldsymbol{H}^{-1} - \xi\boldsymbol{I}) = 0\,. \tag{2.57}$$

Once the locations of the quadrature points as a function of the known moments is obtained, it is possible to find their associated weights by simply solving N of the $2N$ equations shown in Eq. (2.51), which are now all linear. With the quadrature points locations and weights calculated, any higher-order moments can also be expressed as shown in Eq. (2.51).

Multi-Dimensional Quadrature-Based Distribution Function

In the case of multi-dimensional distribution functions, the quadrature points cannot be obtained through a direct method, as is possible for one-dimensional distribution functions. When the distribution function spans multiple dimensions, a choice of quadrature points with strictly positive weights appears to be challenging. Furthermore, the obtained model is not guaranteed to be hyperbolic. A method must be used to solve for the quadrature points while insuring positive weights, realizability, and hyperbolicity. Such methods have been proposed by Fox [29], the most successful ones being the conditional quadrature method of moments (CQMOM) [46] and the extended quadrature method of moments (EQMOM) [47]. These methods preserve all previously mentioned desired properties in a way that is not extensively expensive to compute.

Though quadrature-based moment closures, and the other techniques shown in this chapter, continue to be developed, the choice in this work is to follow the maximum-entropy hierarchy of closures due to their history of modelling accuracy and mathematical elegance. Details of these methods are shown in the next chapter.

Chapter 3

The Maximum-Entropy Hierarchy

One promising technique for the selection of the assumed distribution function is based on entropy-maximization [11, 28, 36]. In this technique, $\mathcal{F}$ is chosen so that the entropy is maximized while the known moments are respected. For monatomic perfect gases, the entropy density is known to be the moment associated with the velocity weight, $M = -(\ln \mathcal{F} - 1)$. Mathematically this maximization problem is expressed as,

$$\max_{\mathcal{F}} \langle -(\mathcal{F} \ln \mathcal{F} - \mathcal{F}) \rangle \qquad \text{such that} \qquad \boldsymbol{U} = \langle \boldsymbol{W} \mathcal{F} \rangle \ . \tag{3.1}$$

This optimization problem is usually solved using the method of Lagrange multipliers. A vector of Lagrange multipliers, $\boldsymbol{\alpha}$, is defined and the constrained maximization is recast as an expanded unconstrained problems, where one searches for a critical point of,

$$\mathcal{L} = \langle -((\mathcal{F} \ln \mathcal{F} - \mathcal{F}) \rangle - \boldsymbol{\alpha}^T (\boldsymbol{U} - \langle \boldsymbol{W} \mathcal{F} \rangle) \ . \tag{3.2}$$

The critical point of the Lagrangian function is defined as the point where $\frac{\partial \mathcal{L}}{\partial \mathcal{F}} = 0$,

$$\begin{aligned} \frac{\partial \mathcal{L}}{\partial \mathcal{F}} &= \langle -\ln \mathcal{F} \rangle + \boldsymbol{\alpha}^T \langle \boldsymbol{W} \rangle = 0 \\ &= \left\langle \ln \mathcal{F} - \boldsymbol{\alpha}^T \boldsymbol{W} \right\rangle = 0 \end{aligned} \tag{3.3}$$

By observation of Eq. (3.3), it is trivial that it is satisfied if the distribution function is of the form,

$$\mathcal{F}_{\text{M.E.}} = e^{\boldsymbol{\alpha}^T \boldsymbol{W}}, \tag{3.4}$$

where $\boldsymbol{\alpha}$ is the vector of closure coefficients, which are also the Lagrange multipliers, and $\boldsymbol{W}$ is the vector of velocity weights of the closure.

The distribution function associated with this technique ensures a positive number density for all velocity space. Closures of this type also have an elegant proof of hyperbolicity for the resulting PDEs when a distribution function of the form given in Eq. (3.4) can be found that is consistent with the moments of interests [28]. This can be shown by defining a density potential, $h(\boldsymbol{\alpha})$, and a flux potential, $f_i(\boldsymbol{\alpha})$,

$$h(\boldsymbol{\alpha}) = \left\langle e^{\boldsymbol{\alpha}^T \boldsymbol{W}} \right\rangle \qquad\qquad j_i(\boldsymbol{\alpha}) = \left\langle v_i e^{\boldsymbol{\alpha}^T \boldsymbol{W}} \right\rangle . \tag{3.5}$$

Taking the first derivative of these potentials with respect to the coefficient vector, $\boldsymbol{\alpha}$, leads to,

$$h_{,\boldsymbol{\alpha}}(\boldsymbol{\alpha}) = \left\langle \boldsymbol{W} e^{\boldsymbol{\alpha}^T \boldsymbol{W}} \right\rangle = \boldsymbol{U} \qquad\qquad j_{i,\boldsymbol{\alpha}}(\boldsymbol{\alpha}) = \left\langle v_i \boldsymbol{W} e^{\boldsymbol{\alpha}^T \boldsymbol{W}} \right\rangle = \boldsymbol{F}_i \,, \tag{3.6}$$

where the index $,\boldsymbol{\alpha}$ denotes the first derivative with respect to $\boldsymbol{\alpha}$. Equation (2.13) can be rewritten as

$$\frac{\partial h_{,\boldsymbol{\alpha}}}{\partial t} + \frac{\partial j_{i,\boldsymbol{\alpha}}}{\partial x_i} = \boldsymbol{S} \,. \tag{3.7}$$

By taking the second derivative of the potentials with respect to $\boldsymbol{\alpha}$,

$$h_{,\boldsymbol{\alpha},\boldsymbol{\alpha}}(\boldsymbol{\alpha}) = \left\langle \boldsymbol{W}\boldsymbol{W}^T e^{\boldsymbol{\alpha}^T \boldsymbol{W}} \right\rangle = \frac{\partial \boldsymbol{U}}{\partial \boldsymbol{\alpha}} \qquad\qquad j_{i,\boldsymbol{\alpha},\boldsymbol{\alpha}}(\boldsymbol{\alpha}) = \left\langle v_i \boldsymbol{W}\boldsymbol{W}^T e^{\boldsymbol{\alpha}^T \boldsymbol{W}} \right\rangle = \frac{\partial \boldsymbol{F}_i}{\partial \boldsymbol{\alpha}} \,, \tag{3.8}$$

and by using the chain rule, Eq. (3.7) can be written as a transport equation for the closure coefficients, $\boldsymbol{\alpha}$,

$$h_{,\boldsymbol{\alpha},\boldsymbol{\alpha}} \frac{\partial \boldsymbol{\alpha}}{\partial t} + j_{i,\boldsymbol{\alpha},\boldsymbol{\alpha}} \frac{\partial \boldsymbol{\alpha}}{\partial x_i} = \boldsymbol{S} \,. \tag{3.9}$$

The hessian matrix, $h_{,\boldsymbol{\alpha},\boldsymbol{\alpha}}$, is positive definite since,

$$\boldsymbol{N}^T h_{,\boldsymbol{\alpha},\boldsymbol{\alpha}} \boldsymbol{N} = \boldsymbol{N}^T \left\langle \boldsymbol{W}\boldsymbol{W}^T e^{\boldsymbol{\alpha}^T \boldsymbol{W}} \right\rangle \boldsymbol{N} = \left\langle \boldsymbol{N}^T \boldsymbol{W}\boldsymbol{W}^T \boldsymbol{N} e^{\boldsymbol{\alpha}^T \boldsymbol{W}} \right\rangle = \left\langle \left(\boldsymbol{N}^T \boldsymbol{W}\right)^2 e^{\boldsymbol{\alpha}^T \boldsymbol{W}} \right\rangle > 0 \,, \tag{3.10}$$

for any non-zero vector $\boldsymbol{N}$. By the positive definiteness of $h_{,\boldsymbol{\alpha},\boldsymbol{\alpha}}$ and the symmetry of $j_{i,\boldsymbol{\alpha},\boldsymbol{\alpha}}$, Eq. (3.9) has the Godunov form of a symmetric hyperbolic system for $\boldsymbol{\alpha}$ [13].

In addition to its mathematical elegance, one strong physical argument for the choice of this technique is that the distribution with the maximum entropy is statistically the most likely distribution for a given set of known moments [35]. If one must select a distribution based on incomplete information, the most likely one is a good choice.

When working with maximum-entropy closures, the velocity weights must be chosen such that they meet three conditions [28]. They must contain the weight associated with the Euler equations as a subset, since they represent the equilibrium state. They must also be translationally and rotationally invariant to ensure that the associated set of equations maintain these invariants. Finally, they must be chosen such that the distribution function is finite for all velocity space, even when the particle velocity goes to infinity, so that moments of the distribution function remain finite. The satisfaction of these conditions leads to a positive distribution function that generates a set of equations that are hyperbolic in nature. The first four members of the maximum-entropy hierarchy in three-dimensions are,

$$N = 5 \qquad \boldsymbol{W} = [1, v_i, v_i v_i] \qquad \boldsymbol{V} = [\rho, u_i, p] \;, \tag{3.11}$$

$$N = 10 \qquad \boldsymbol{W} = [1, v_i, v_i v_j] \qquad \boldsymbol{V} = [\rho, u_i, P_{ij}] \;, \tag{3.12}$$

$$N = 14 \qquad \boldsymbol{W} = [1, v_i, v_i v_j, v_i v_j v_j, v_i v_i v_j v_j] \qquad \boldsymbol{V} = [\rho, u_i, P_{ij}, Q_{ijj}, R_{iijj}] \;, \tag{3.13}$$

$$N = 21 \qquad \boldsymbol{W} = [1, v_i, v_i v_j, v_i v_j v_k, v_i v_i v_j v_j] \qquad \boldsymbol{V} = [\rho, u_i, P_{ij}, Q_{ijk}, R_{iijj}] \;, \tag{3.14}$$

where N is the number of equations, $\boldsymbol{W}$ is the velocity weight vector and $\boldsymbol{V}$ is the vector of moments of interest.

The first two members of the maximum-entropy hierarchy are the 5-moment and 10-moment closures. In both cases the distribution function is an exponential of a second-order polynomial. The 5-moment closure leads to the well known compressible Euler equations. The 10-moment closure, with the distribution function

$$\mathcal{F} = \frac{\rho}{m\left(2\pi\right)^{3/2}\left(\det\Theta\right)^{1/2}} \exp\left(-\frac{1}{2}\Theta_{ij}^{-1} c_i c_j\right) \;, \qquad \text{where} \qquad \Theta_{ij} = \frac{P_{ij}}{\rho} \;, \tag{3.15}$$

leads to a system of ten hyperbolic equations capable of predicting compressible viscous gas flow without heat-transfer. This closure has been proven to be very accurate and successful for flow prediction in both the continuum and transition regimes [2, 6, 7, 16, 41]. However, its inability to model heat transfer limits its application to situations where this effect is negligible. The next two members of this family are the 14-moment and 21-moment closures. The distribution functions associated with these two closures are an exponential of a fourth-order polynomial, allowing for some skewness or asymmetry in the distribution function and therefore granting the closure the ability to predict non-zero heat-transfer. Unfortunately, due to the fourth-order nature of the polynomial, $\boldsymbol{\alpha}^{\boldsymbol{T}}\boldsymbol{W}$, it is impossible to integrate the

closing fluxes in closed form. To obtain the closing fluxes at each flux calculation, one needs to use an iterative procedure that require repeated numerical integration over all velocity space. This iterative procedure consists of solving the entropy-maximization problem numerically in order to solve for the coefficient, $\boldsymbol{\alpha}$, contained in the distribution function and then numerically integrate the closing fluxes. Commonly, a Newton search is used to solve this problem, for which convergence appears to be challenging in some instances. This procedure is prohibitively expensive and cannot practically be used as it requires many 3D numerical integrations on infinite domains whenever a flux is needed.

In the case of the 14-moment closure, an approximation for the closing fluxes has been previously proposed by M$^{\text{c}}$Donald and Torrilhon [31]. The approximation is robust and hyperbolic for a one-dimensional gas, however, its extension to three-dimensions is not as robust and loses hyperbolicity for some physically realizable states. Further investigation and experience with this fourteen-moment closure has revealed that proposed fits for the heat-flux tensor are quite poor. Even more bothersome is the fact that the expressions for the other higher-order fluxes rely directly on the approximation for the heat-flux tensor. Thus, errors in the fit for Q_{ijk} seriously pollute all closing fluxes. By moving to a twenty-one-moment closure, the entire uncontracted heat-flux tensor is added to the solution vector. Also, when the interpolation technique is applied to this expanded closure, closing fluxes do not couple together—they only depend on entries in the solution vector. Therefore, errors in one flux cannot pollute the approximations for other terms. It is therefore expected that a more accurate and robust closure with twenty-one moments could be easier to construct. This is the main goal of this thesis.

3.1 Numerically Solving the Entropy-Maximization Problem

It was mentioned that, in the event where the distribution function cannot be integrated in closed-form, it is necessary to use an iterative procedure to numerically solve for the values of the free-coefficients, $\boldsymbol{\alpha}$ associated with a target state, $\boldsymbol{U}_{\text{target}}$. For this purpose, the Newton iterative method is used to optimize the associated cost function,

$$\min_{\boldsymbol{\alpha}} J(\boldsymbol{\alpha})\,, \tag{3.16}$$

with the iterative step,

$$\boldsymbol{\alpha}_{n+1} = \boldsymbol{\alpha}_n - \left[\frac{\partial^2 J(\boldsymbol{\alpha})}{\partial \boldsymbol{\alpha} \partial \boldsymbol{\alpha}}\right]^{-1} \frac{\partial J(\boldsymbol{\alpha})}{\partial \boldsymbol{\alpha}} \,. \tag{3.17}$$

If the cost function, $J(\boldsymbol{\alpha})$, is convex, then there exists a unique solution to the optimization problem. In the context of the entropy-maximization problem, the cost function is,

$$J(\boldsymbol{\alpha}) = \langle m\mathcal{F}(\boldsymbol{\alpha})\rangle - \boldsymbol{\alpha}^T \boldsymbol{U}_{\text{target}} \,, \tag{3.18}$$

where $\mathcal{F}$ is the chosen distribution function and $\boldsymbol{\alpha}$ are the free-coefficients consistent with the solution vector U_{target}. The first and second derivatives of the cost function, $J(\boldsymbol{\alpha})$, with respect to $\boldsymbol{\alpha}$ are,

$$\frac{\partial J(\boldsymbol{\alpha})}{\partial \boldsymbol{\alpha}} = \langle m\boldsymbol{W}\mathcal{F}(\boldsymbol{\alpha})\rangle - \boldsymbol{U}_{\text{target}} \,, \tag{3.19}$$

$$\frac{\partial^2 J(\boldsymbol{\alpha})}{\partial \boldsymbol{\alpha} \partial \boldsymbol{\alpha}} = \left\langle m\boldsymbol{W}\boldsymbol{W}^T\mathcal{F}(\boldsymbol{\alpha})\right\rangle \,. \tag{3.20}$$

As shown in Eq. (3.10), the Hessian of the cost function is positive definite and in this case proves the convexity of the cost function $J(\boldsymbol{\alpha})$. Since Newton's method converges to the critical point, where the first derivative is zero, it can be seen by inspection of Eq. (3.19) that, at convergence,

$$\langle m\boldsymbol{W}\mathcal{F}(\boldsymbol{\alpha})\rangle = \boldsymbol{U}_{\text{target}} \,, \tag{3.21}$$

and the correct free-coefficients are therefore obtained. Once the numerical iterative method completed, it is then possible to numerically the distribution function to obtain the closing fluxes. In order to initiate the iterative process described in Eq. (3.17), an initial guess for the values of $\boldsymbol{\alpha}$ must be provided. The initial values for $\boldsymbol{\alpha}$ are often chosen to be the one associated with the Gaussian distribution function described in Eq. (3.15).

Even though the convexity of the cost function guarantees a unique solution, this technique cannot be used to calculate the closing fluxes at each time step. To start, many iterations are necessary, each requiring integration over the entire velocity domain, rendering the method computationally expensive. Furthermore, in some instances convergence to a solution can be impossible due to ill-conditioning caused by very large first and second derivatives.

Chapter 4

A Closed-Form Approximation for the Closing Fluxes of the Fourteen-Moment Closure

The following section summarizes the work of M^{c}Donald and Torrilhon [31] on the development of a closed-form approximation for the fourteen-moment closure of the maximum-entropy hierarchy. The approximation for the twenty-one moment model is, in part, based on this work. It is also important to present this closure in order to better show its issues and the motivation behind the current move to the twenty-one moment closure. This closure is the first in the maximum-entropy hierarchy to contain a treatment for heat-transfer. For this closure, the vector of generating weights is $\boldsymbol{W} = [1, v_i, v_i v_j, v_i v_j v_j, v_i v_i v_j v_j]$, which leads to the following system of equations,

$$\frac{\partial}{\partial t}\left[\rho\right] + \frac{\partial}{\partial x_i}\left[\rho u_i\right] = 0 \tag{4.1}$$

$$\frac{\partial}{\partial t}\left[\rho u_i\right] + \frac{\partial}{\partial x_j}\left[\rho u_i u_j + P_{ij}\right] = 0 \tag{4.2}$$

$$\frac{\partial}{\partial t}\left[\rho u_i u_j + P_{ij}\right] + \frac{\partial}{\partial x_k}\left[\rho u_i u_j u_k + u_i P_{jk} + u_j P_{ik} + u_k P_{ij} + Q_{ijk}\right] = C_{ij} \tag{4.3}$$

$$\frac{\partial}{\partial t}\left[\rho u_i u_j u_j + u_i P_{jj} + 2 u_j P_{ij} + Q_{ijj}\right] \tag{4.4}$$

$$
\begin{aligned}
&+\frac{\partial}{\partial x_l}[\rho u_i u_j u_j u_l + 2u_i u_j P_{jl} + u_i u_l P_{jj} + u_j u_j P_{il} + 2u_j u_l P_{ij} \\
&\quad + u_i Q_{ljj} + u_l Q_{ijj} + 2u_j Q_{ijl} + R_{iljj}] = C_{ijj} \\
&\frac{\partial}{\partial t}\left[\rho u_i u_i u_j u_j + 2u_i u_i P_{jj} + 4u_i u_j P_{ij} + 4u_i Q_{ijj} + R_{iijj}\right] \\
&+\frac{\partial}{\partial x_k}[\rho u_i u_i u_j u_j u_k + 2u_i u_i u_k P_{jj} + 4u_i u_i u_j P_{jk} + 4u_i u_j u_k P_{ij} + 2u_i u_i Q_{kjj} \\
&\quad + 4u_i u_k Q_{ijj} + 4u_i u_j Q_{ijk} + 4u_i R_{ijjk} + u_k R_{iijj} + S_{iijjk}] = C_{iijj}
\end{aligned}
\tag{4.5}
$$

The necessary closing fluxes for the fourteen-moment model (those present in the flux, but not the solution vector) are shown in red in Eq. (4.1)–(4.5). A closed-form approximation is necessary for those moments in order to close the system.

4.1 Region of Physical Realizability of the 14-Moment Closure

To begin investigating expressions for the closing fluxes, it is first useful to evaluate what region in moment space corresponds to physically realizable states. Physical realizability requires the existence of a positive distribution function consistent with a given set of moments. This allows one to restrict the size of the region for which an approximation to the closing fluxes is needed. Solving a Hamburger problem gives a necessary, but unfortunately not sufficient condition, for the physical realizability region [17]. This analysis is done by defining a matrix

$$
\boldsymbol{Y} = \left\langle m\boldsymbol{M}\boldsymbol{M}^T\mathcal{F}\right\rangle = \begin{bmatrix}
\rho & 0 & 0 & 0 & P_{ii} \\
0 & P_{xx} & P_{xy} & P_{xz} & Q_{xii} \\
0 & P_{xy} & P_{yy} & P_{yz} & Q_{yii} \\
0 & P_{xz} & P_{yz} & P_{zz} & Q_{zii} \\
P_{ii} & Q_{xii} & Q_{yii} & Q_{zii} & R_{iijj}
\end{bmatrix},
$$

where $\boldsymbol{M} = [1, v_x, v_y, v_z, \boldsymbol{v}^2]^T$. For this treatment, it is assumed that the gas is viewed from a frame of reference in which the bulk velocity is zero, $u_i = 0$. A necessary condition for physical realizability is that this matrix be positive definite. This is because, for a positive

distribution function, $\mathcal{F}$, it is necessary that the matrix, $\boldsymbol{Y}$, be positive definite, as

$$\boldsymbol{N}^T\boldsymbol{Y}\boldsymbol{N} = \boldsymbol{N}^T\left\langle m\boldsymbol{M}\boldsymbol{M}^T\mathcal{F}\right\rangle\boldsymbol{N} = \left\langle m\boldsymbol{N}^T\boldsymbol{M}\boldsymbol{M}^T\boldsymbol{N}\mathcal{F}\right\rangle = \left\langle m\left(\boldsymbol{N}^T\boldsymbol{M}\right)^2\mathcal{F}\right\rangle > 0\,, \tag{4.6}$$

for any vector $\boldsymbol{N}$. The positive definiteness of the matrix is ensured when the density, ρ, is bigger than zero, the pressure tensor, P_{ij}, is positive definite and when

$$R_{iijj} \geq Q_{kii}\left(P^{-1}\right)_{kl}Q_{ljj} + \frac{P_{ii}P_{jj}}{\rho}\,. \tag{4.7}$$

Although this analysis typically provides only a necessary condition on realizability, extensive experience suggests that this indeed describes all of physically realizable states in the case of the fourteen-moment closure. Moment states that do not respect the condition given by Eq. (4.7) are states that are not physically realizable. That is, they do not correspond to *any* positive distribution.

4.2 The Junk Subspace

Along with the physical realizability region, it is also important to investigate which physically realizable state can be realized by the assumed form of the distribution function. Junk has shown that there exists a subspace of physically realizable states that cannot be realized by an assumed distribution function of a form that maximizes entropy [23]. Since the equilibrium state resides on the boundary of the Junk subspace, it is important to consider it in the development of an approximation. For the fourteen-moment closure in three-dimensional space, it is known that the Junk subspace is given by

$$Q_{ijj} = 0 \qquad R_{iijj} > \frac{2P_{ji}P_{ij} + P_{ii}P_{jj}}{\rho}\,. \tag{4.8}$$

When all entries of the heat-flux vector are zero, there is a maximum value for the fourth-order moment. The distribution function at this maximum value corresponds to the assumed form from the ten-moment Gaussian closure of maximum-entropy. Moment states with a larger value for the fourth-order moment present a singularity in their closing flux and cannot be calculated. That is, the value of the fifth-order closing fluxes go from positive infinity on one side of the Junk subspace to negative infinity on the other side.

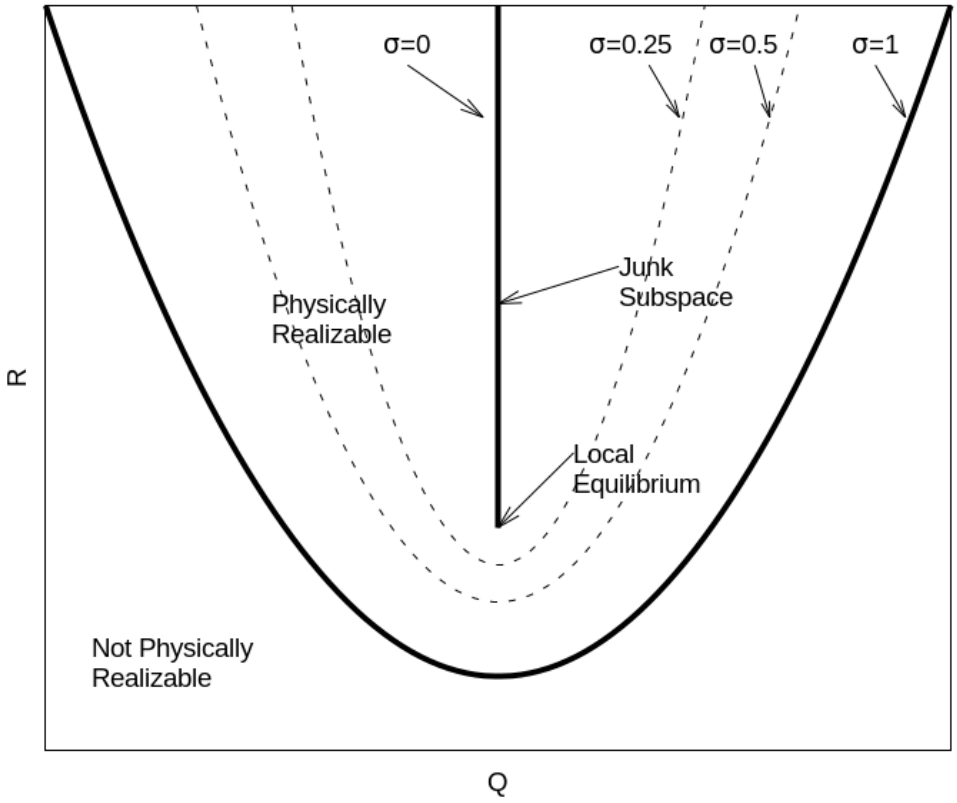

Figure 4.1: Low-dimensional representation of physically realizable moment space of the fourteen-moment model

4.3 Parabolic Mapping of Moment Space

A parabolic mapping between the Junk subspace and the physical realizability boundary was found to be useful in the development of expressions for the approximate closing fluxes. A new variable, σ, is defined such that it is equal to zero at the Junk subspace and one at the physical realizability limit. A low-dimensional representation of realizable moment space is illustrated in Figure 4.1, when $\sigma = 1$ the parabola overlaps the realizability boundary, and as σ is reduced the corresponding parabola moves up on the R axis and shrinks in the direction of the Q axis until it lays over the Junk subspace as $\sigma = 0$. The mapping variable, σ, is defined through the expression

$$R_{iijj} = \frac{1}{\sigma} Q_{kii} \left(P^{-1}\right)_{kl} Q_{ljj} + \frac{2(1-\sigma)P_{ij}P_{ji} + P_{ii}P_{jj}}{\rho}\,, \tag{4.9}$$

leading to

$$\sigma = \frac{A + \sqrt{A^2 + 8\rho P_{ij} P_{ji} Q_{kii} \left(P^{-1}\right)_{kl} Q_{ljj}}}{4 P_{ij} P_{ji}} \,, \tag{4.10}$$

where,

$$A = 2 P_{ij} P_{ji} + P_{ii} P_{jj} - \rho R_{iijj} \,.$$

4.4 Closing Fluxes on the Physical Realizability Boundary

Numerical investigation has shown that, on the physical realizability boundary, the distribution function is non-zero only on a sphere in velocity space [31]. An example distribution on this boundary is shown in Figure 4.2.

It is possible to center the sphere at the origin by performing a simple Galilean transformation on the velocity frame of reference. This involves simply shifting the sphere in velocity space so that it is centered at the origin. The new shifted frame of reference is denoted by the hat notation in the following. If the sphere was originally centered at a velocity, $\boldsymbol{v_c}$, the new velocity in the shifted frame of reference is $\hat{\boldsymbol{v}} = \boldsymbol{v} - \boldsymbol{v_c}$. Such a transformation does not impact the moments of the distribution function generated with random velocity weights. The only macroscopic property that is impacted is the bulk velocity. Since the distribution is only non-zero on a sphere it is now possible to relate higher-order contracted moments to lower-order moments. This is because any $\hat{\boldsymbol{v}}^2$ terms in higher-order contracted moments can be taken out of the integral, since they are constant on the sphere. For example,

$$\hat{U}_{ii} = \left\langle m \hat{\boldsymbol{v}}^2 \mathcal{F} \right\rangle = \hat{\boldsymbol{v}}^2 \left\langle m \mathcal{F} \right\rangle = \hat{\boldsymbol{v}}^2 \rho \,,$$

where $\hat{\boldsymbol{v}}^2$ is the square of the radius of the spherical distribution function in velocity space. The new shifted bulk velocity can also be found easily since,

$$\hat{U}_{ijj} = \left\langle m \hat{\boldsymbol{v}}_{\boldsymbol{i}} \hat{\boldsymbol{v}}^2 \mathcal{F} \right\rangle = \hat{\boldsymbol{v}}^2 \left\langle m \hat{v}_i \mathcal{F} \right\rangle = \hat{\boldsymbol{v}}^2 \rho \hat{u}_i \,,$$

which can be solve to find that,

$$\hat{u}_j = -\frac{1}{2} \left(P^{-1}\right)_{ij} Q_{ikk} \,.$$

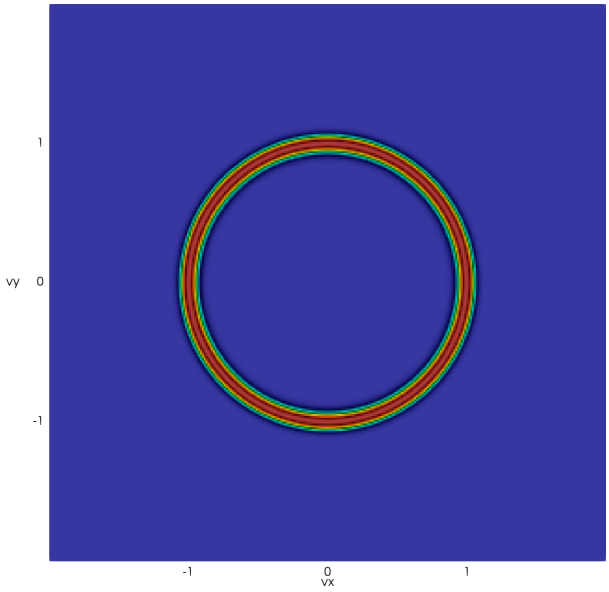

(a) $\rho = 1$, $u_x = u_y = u_z = 0$, $P_{xx} = 1/3$, $P_{yy} = P_{zz} = 1/3$, $Q_{xii} = 0$, $Q_{yii} = Q_{zii} = 0$

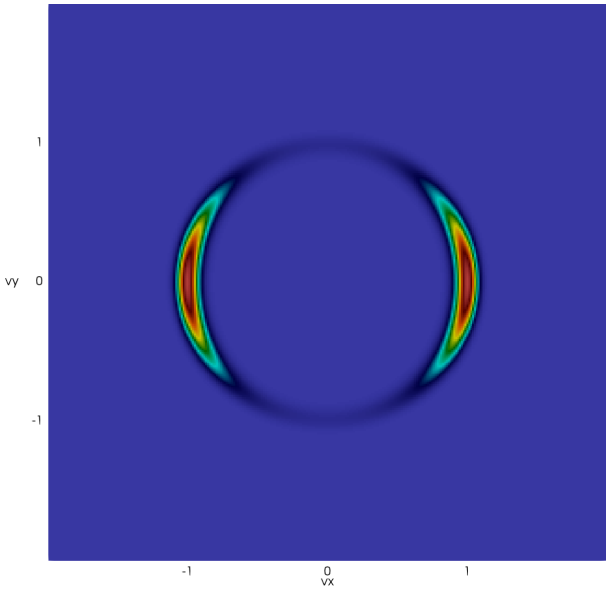

(b) $\rho = 1$, $u_x = u_y = u_z = 0$, $P_{xx} = 2/3$, $P_{yy} = P_{zz} = 1/6$, $Q_{xii} = 0$, $Q_{yii} = Q_{zii} = 0$

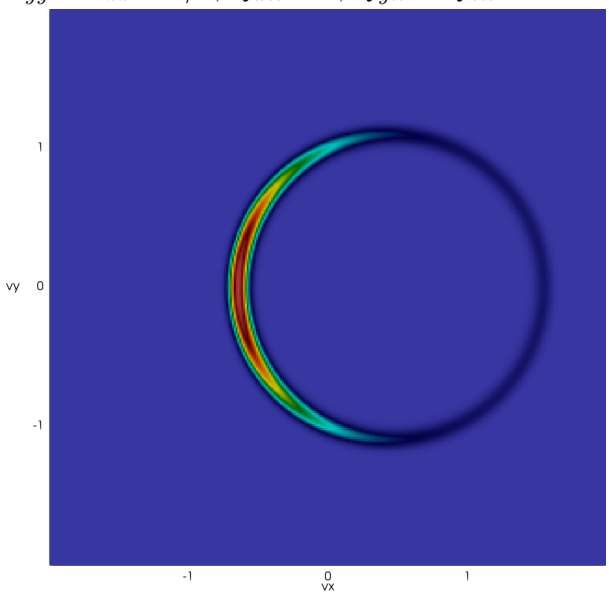

(c) $\rho = 1$, $u_x = u_y = u_z = 0$, $P_{xx} = 1/3$, $P_{yy} = P_{zz} = 1/3$, $Q_{xii} = 0.3$, $Q_{yii} = Q_{zii} = 0$

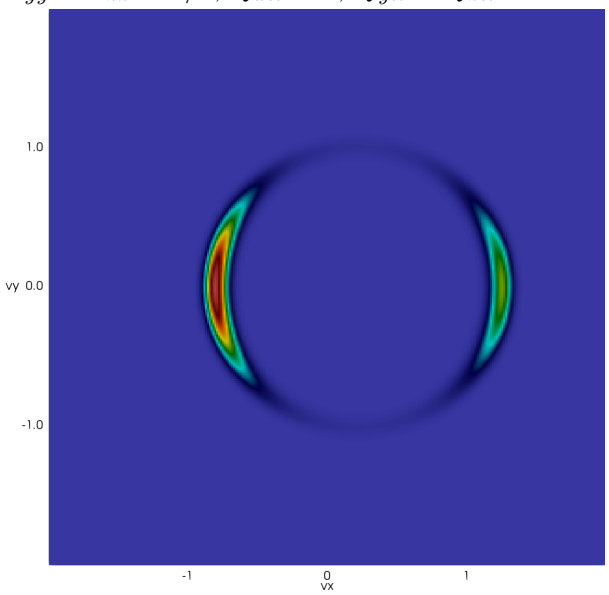

(d) $\rho = 1$, $u_x = u_y = u_z = 0$, $P_{xx} = 2/3$, $P_{yy} = P_{zz} = 1/6$, $Q_{xii} = 0.3$, $Q_{yii} = Q_{zii} = 0$

Figure 4.2: Examples of distribution functions on the physical realizability boundary.

Through the same technique it is also possible to obtain expressions for R_{ijkk} and S_{ijjkk} on the boundary of physical realizability as

$$R_{ijkk} = Q_{ijl}\left(P^{-1}\right)_{lm} Q_{mkk} + \frac{P_{ij}P_{kk}}{\rho}\,, \tag{4.11}$$

$$S_{ijjkk} = P^{-1}_{kn}P^{-1}_{lm}Q_{npp}Q_{mjj}Q_{ikl} + 2\frac{P_{jj}Q_{ikk}}{\rho}\,. \tag{4.12}$$

Unfortunately, since the closing flux Q_{ijk} is not a contracted moment, it is impossible to use this technique to find an expression for this tensor on the physical realizability boundary. This has been the major disadvantage of using only fourteen moments.

4.5 Closing Fluxes at the Gaussian Level

At the Gaussian level, the lower boundary of the Junk subspace, it is possible to integrate R_{ijkk} analytically as

$$R_{ijkk} = \frac{1}{\rho}\left(P_{ij}P_{kk} + 2P_{ik}P_{kj}\right)\,. \tag{4.13}$$

Since, for the Gaussian distribution function, all odd random velocity moments are zero, the closed-form expression for Q_{ijk} and S_{ijjkk} at this point is zero. It is however possible to find derivatives. This is shown in detail in the work of M$^{\text{c}}$Donald and Torrilhon [31] and yields,

$$\begin{aligned}\frac{\partial Q_{ijk}}{\partial Q_{mnn}} &= \left[2P_{il}\left(P^2\right)_{jk} + 2P_{kl}\left(P^2\right)_{ij} + 2P_{jl}\left(P^2\right)_{ik}\right]B^{-1}_{lm} \\ &= K_{ijkm}\,,\end{aligned}$$

$$\begin{aligned}\frac{\partial S_{ijjkk}}{\partial Q_{mnn}} = \frac{1}{\rho}\Bigg[&2P_{il}\left(P_{\alpha\alpha}\right)^3 + 12P_{il}\left(P^3\right)_{\alpha\alpha} + 14\left(P^2\right)_{\alpha\alpha}\left(P^2\right)_{il} + 20P_{\alpha\alpha}\left(P^3\right)_{il} \\ &+ 20\left(P^4\right)_{il} - 2\left(P^2\right)_{\alpha\alpha}P_{\beta\beta}P_{il} - 6\left(P_{\alpha\alpha}\right)^2\left(P^2\right)_{il}\Bigg]B^{-1}_{lm} \\ = W_{im}\,,\end{aligned}$$

where,

$$B_{lm} = 2P_{lm}\left(P^2\right)_{\alpha\alpha} + 4\left(P^3\right)_{lm}\,.$$

It is then possible to approximate the value of Q_{ijk} and S_{ijjkk} near a Gaussian as,

$$Q_{ijk} = K_{ijkm} Q_{mnn} \tag{4.14}$$

$$S_{ijjkk} = W_{im} Q_{mnn} \,. \tag{4.15}$$

4.6 Closing-Flux Approximations

By using the expressions for the closing fluxes at the realizability boundary and at the Gaussian level, as well as the parabolic mapping, it is possible to develop expressions for them in all moment space. The approximations for the closing fluxes chosen by M$^{\text{c}}$Donald and Torrilhon are

$$Q_{ijk} = K_{ijkm} Q_{mnn} \tag{4.16}$$

$$R_{ijkk} = \frac{1}{\sigma} Q_{ijl} \left(P^{\text{-}1}\right)_{lm} Q_{mkk} + \frac{2(1-\sigma) P_{ik} P_{kj} + P_{ij} P_{kk}}{\rho} \tag{4.17}$$

$$S_{ijjkk} = \frac{1}{\sigma^2} P^{\text{-}1}_{kn} P^{\text{-}1}_{lm} Q_{npp} Q_{mjj} Q_{ikl} + 2\sigma^{\frac{1}{2}} \frac{P_{jj} Q_{ikk}}{\rho} + \left(1 - \sigma^{\frac{1}{2}}\right) W_{im} Q_{mnn} \,. \tag{4.18}$$

These expressions were developed to match as closely as possible the exact closing fluxes for an axisymmetric distribution function in velocity space and one-dimension in physical space. Unfortunately, since no expression is obtained for Q_{ijk} at the realizability boundary, the approximation for that closing flux is simply a linear extrapolation from the expression at the Gaussian level, as shown in Eq. (4.16).

4.7 Limitation of the Fourteen-Moment Approximations

The approximations proposed by M$^{\text{c}}$Donald and Torrilhon unfortunately suffer from one main weakness. Only a small amount of information is known about the closing flux, Q_{ijk}, leading to a poorer approximation. This is illustrated in Figure 4.3. This figure shows the ratio of Q_{xxx} over Q_{xii} in moment space for a value of $\sigma = 0.55$. The previously proposed approximation does not well represent the third-order closing flux. As seen in

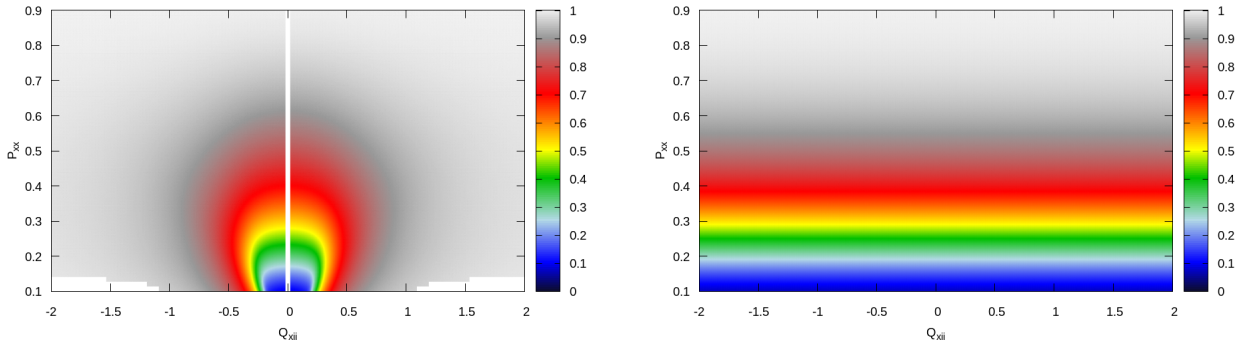

(a) Exact maximum-entropy closing flux Q_{xxx}

(b) Approximated closing flux Q_{xxx}

Figure 4.3: Comparison between the true maximum-entropy closing flux, $\frac{Q_{xxx}}{Q_{xii}}$, and the proposed approximation.

Eqs. (4.17) and (4.18), the approximation for the closing fluxes R_{ijkk} and S_{ijjkk} depend strongly on the approximation for Q_{ijk}. Therefore a poor approximation for the third-order closing flux renders the approximations for all higher-order closing fluxes poor as well. In Figure 4.4, it is shown that, when using the exact value for Q_{xxx} in the calculation of R_{xxii} and S_{xiijj}, the result is in close agreement with the exact solution for the respective closing flux. The closing fluxes obtained by solving the entropy-maximization problem are shown in Figures 4.4a and 4.4b while the closing-fluxes calculated using the proposed approximation are shown in Figures 4.4c and 4.4d. In Figures 4.4e and 4.4f the closing-fluxes calculated using the proposed approximation but with the exact value for Q_{xxx} is shown. The inaccurate prediction of the closing fluxes yields a model that is not representative of the associated distribution function and often leads to complex eigenvalues of the flux Jacobian. The loss of hyperbolicity and accuracy is detrimental to the efficiency of the model in predicting non-equilibrium flows. The lack of an accurate expression for Q_{ijk} at the realizability boundary, as well as the limited amount of information known about this closing flux and its form, makes the development of an accurate approximation challenging. In the twenty-one-moment closure, all entries of the heat-flux tensor are part of the solution vector and the need of an approximation is removed. In this closure, the approximations for the closing fluxes are all independent of each other. This means that a weakness in one approximation does not spread to approximations for other closing fluxes. This gives motivation that the 21-moment closure may be easier to approximate accurately.

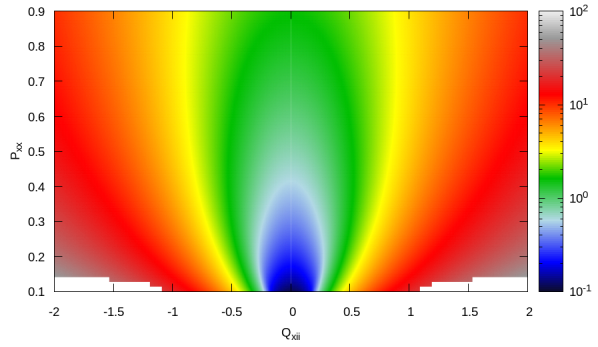

(a) Exact maximum-entropy closing flux R_{xxii}

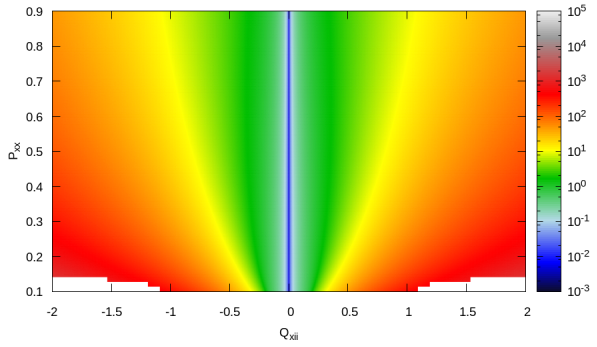

(b) Exact maximum-entropy closing flux S_{xiijj}

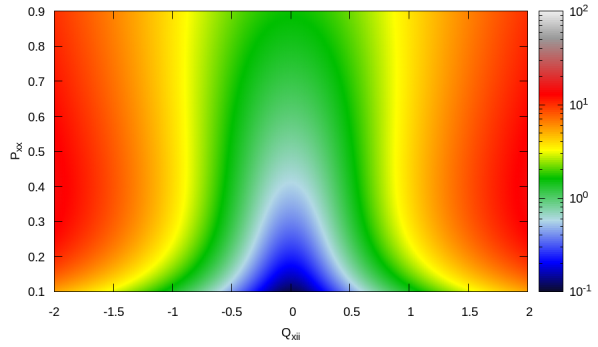

(c) Approximated closing flux R_{xxii}

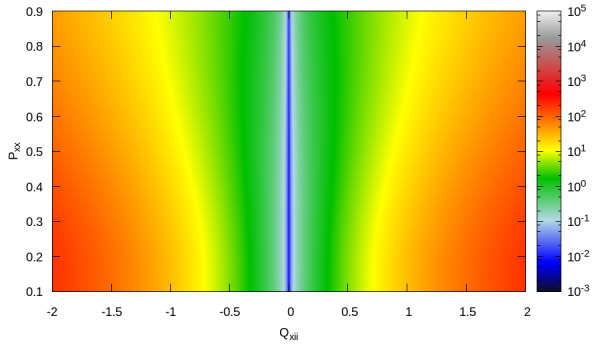

(d) Approximated closing flux S_{xiijj}

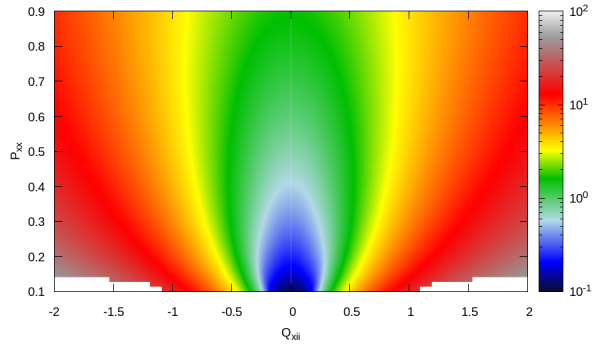

(e) Approximated closing flux R_{xxii} using the correct value for Q_{xxx}

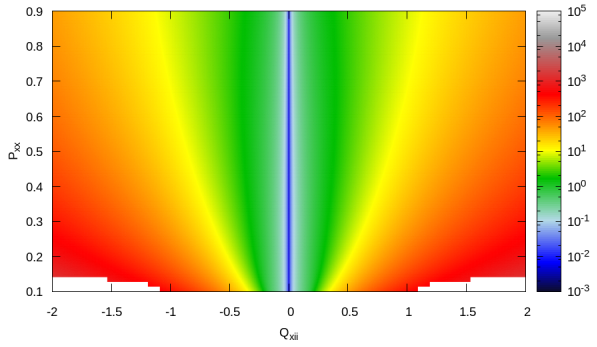

(f) Approximated closing flux S_{xiijj} using the correct value for Q_{xxx}

Figure 4.4: Comparison of the approximated higher-order closing flux calculated using the approximated Q_{xxx} vs the exact Q_{xxx} for a value of $\sigma = 0.55$.

Chapter 5

A New Closed-Form Approximation for the Closing Fluxes of the Twenty-One-Moment Closure

The presently investigated closure is the second in the maximum-entropy hierarchy to contain a treatment for heat-transfer. For this closure, the vector of generating weights is $\boldsymbol{W} = [1, v_i, v_i v_j, v_i v_j v_k, v_i v_i v_j v_j]$, which leads to the following system of twenty-one equations,

$$\frac{\partial}{\partial t}\left[\rho\right] + \frac{\partial}{\partial x_i}\left[\rho u_i\right] = 0 \tag{5.1}$$

$$\frac{\partial}{\partial t}\left[\rho u_i\right] + \frac{\partial}{\partial x_j}\left[\rho u_i u_j + P_{ij}\right] = 0 \tag{5.2}$$

$$\frac{\partial}{\partial t}\left[\rho u_i u_j + P_{ij}\right] + \frac{\partial}{\partial x_k}\left[\rho u_i u_j u_k + u_i P_{jk} + u_j P_{ik} + u_k P_{ij} + Q_{ijk}\right] = C_{ij} \tag{5.3}$$

$$\begin{aligned}&\frac{\partial}{\partial t}\left[\rho u_i u_j u_k + u_i P_{jk} + u_j P_{ik} + u_k P_{ij} + Q_{ijk}\right] \\ &+ \frac{\partial}{\partial x_l}[\rho u_i u_j u_k u_l + u_i u_j P_{kl} + u_i u_k P_{jl} + u_i u_l P_{jk} + u_j u_k P_{il} + u_j u_l P_{ik} + u_k u_l P_{ij} \\ &\quad + u_i Q_{jkl} + u_j Q_{ikl} + u_k Q_{ijl} + u_l Q_{ijk} + R_{ijkl}] = C_{ijk}\end{aligned} \tag{5.4}$$

$$\frac{\partial}{\partial t}\left[\rho u_i u_i u_j u_j + 2u_i u_i P_{jj} + 4u_i u_j P_{ij} + 4u_i Q_{ijj} + R_{iijj}\right] \tag{5.5}$$

$$+\frac{\partial}{\partial x_k}[\rho u_i u_i u_j u_j u_k + 2u_i u_i u_k P_{jj} + 4u_i u_i u_j P_{jk} + 4u_i u_j u_k P_{ij} + 2u_i u_i Q_{kjj} + 4u_i u_k Q_{ijj} + 4u_i u_j Q_{ijk} + 4u_i R_{ijjk} + u_k R_{iijj} + S_{iijjk}] = C_{iijj}$$

As was shown, in the case of the fourteen-moment closure, an expression is needed for all entries of the heat-flux tensor, since they are present in the flux, but are not included in the solution vector. The development of a closed form expression for the heat-flux tensor has proven to be difficult especially in three-dimensional space. Furthermore, the expressions developed for higher-order closing fluxes are functions of the heat-flux tensor. For the fourteen-moment closure, if an accurate expression for the heat-flux tensor cannot be found, then none of the closing fluxes can be approximated accurately. In the case of the twenty-one-moment closure, all entries of the uncontracted heat-flux tensor are part of the solution vector. It is therefore not necessary to propose an expression for them. Unfortunately, it is now necessary to have an expression for the full uncontracted R_{ijkl} tensor. However, more information is known about this tensor since expressions for its once-contracted entries are easily obtained. Furthermore, the developed approximations for the closing fluxes are fully independent of each other. The necessary closing fluxes for the twenty-one moment model are shown in bold in Eq. (5.1)–(5.5).

5.1 Region of Physical Realizability

Like the fourteen-moment model, a necessary condition for the physically realizable space is obtained from performing a Hamburger moment problem, yielding the same condition as obtained for the fourteen-moment model in Eq. (4.7),

$$R_{iijj} \geq Q_{kii} \left(P^{-1}\right)_{kl} Q_{ljj} + \frac{P_{ii}P_{jj}}{\rho}\,.$$

Unfortunately, for the twenty-one-moment model, experience shows that there are states that satisfy this inequality that are not, in fact, realizable. By doing the Hamburger problem with different vectors, $\boldsymbol{M}$, it is found that there are also limits on the non-contracted fourth-order moments that are not relevant in the fourteen-moment case. For example, even if the value of R_{iijj} is above the realizability limit in Eq. (4.7), depending on other entries in the solution vector, it is possible that there are limits on other fourth-order moments, such as R_{xxxx}. This limit can be obtained by doing the Hamburger problem with the vector

$\boldsymbol{M} = [1, v_x, v_y, v_z, v_x v_x]^T$ leading to the Hamburger matrix,

$$\boldsymbol{Y} = \left\langle m\boldsymbol{M}\boldsymbol{M}^T\mathcal{F}\right\rangle = \begin{bmatrix} \rho & 0 & 0 & 0 & P_{xx} \\ 0 & P_{xx} & P_{xy} & P_{xz} & Q_{xxx} \\ 0 & P_{xy} & P_{yy} & P_{yz} & Q_{yxx} \\ 0 & P_{xz} & P_{yz} & P_{zz} & Q_{zxx} \\ P_{xx} & Q_{xxx} & Q_{yxx} & Q_{zxx} & R_{xxxx} \end{bmatrix}.$$

To ensure positive definiteness of the matrix, it is found that the fourth-order moment, R_{xxxx}, must satisfy

$$R_{xxxx} \geq Q_{kxx}\left(P^{-1}\right)_{kl} Q_{lxx} + \frac{P_{xx}^2}{\rho}.$$

This additional constraint, and others like it, must all be simultaneously satisfied for a state to be realizable.

5.2 The Junk Subspace for the Twenty-One-Moment Case

In the currently investigated twenty-one-moment closure, extra degrees of freedom representing all entries of the heat-flux tensor are present, as compared to the fourteen-moment model. It is possible to have a heat-flux tensor where the traces are equal to zero without forcing every entry to be zero. If the Junk subspace of the twenty-one-moment closure were to be the same as the fourteen-moment closure this would be detrimental as the subspace would cover a large region and occupy a volume of moment space. Fortunately, experience shows that, for this investigated closure, the Junk subspace only covers region where *all* entries of the heat-flux tensor are simultaneously zero. The subspace is given by

$$Q_{ijk} = 0 \qquad R_{iijj} > \frac{2P_{ji}P_{ij} + P_{ii}P_{jj}}{\rho}. \tag{5.6}$$

It is therefore possible to have the trace of the heat-flux tensor be zero and $R_{iijj} > \frac{2P_{ji}P_{ij}+P_{ii}P_{jj}}{\rho}$ without being in the Junk subspace. This reduces the span of the Junk subspace for the twenty-one-moment closure quite significantly. As the number of moments is increased from fourteen to twenty-one, the Junk subspace remains infinitely thin, as was obtained for the fourteen-moment closure. All moment-state elements of the Junk subspace for the twenty-

one-moment closure are also elements of the Junk subspace for the fourteen-moment closure. When all entries of the heat-flux tensor are zero, there is a maximum value for the fourth-order moment. The distribution function at that maximum value also corresponds to the ten-moment, Gaussian closure of maximum-entropy.

5.3 Parabolic Mapping of Moment Space

A similar parabolic mapping between the Junk subspace and the physical realizability boundary on R_{iijj} is used in the development of approximate expressions for the closing fluxes. A variable, σ, is defined such that it is equal to zero at the Junk subspace and one at the approximate physical realizability limit. The mapping variable, σ, is defined through the following expression,

$$R_{iijj} = Q_{kii}\left(P^{-1}\right)_{kl} Q_{ljj} + \frac{1-\sigma}{2\sigma} Q_{kij}\left(P^{-1}\right)_{kl} Q_{lij} + \frac{2(1-\sigma)P_{ij}P_{ji} + P_{ii}P_{jj}}{\rho}\,, \tag{5.7}$$

leading to,

$$\sigma = \frac{[A] + \sqrt{[A]^2 + 4\rho P_{ij}P_{ji}Q_{kij}\left(P^{-1}\right)_{kl} Q_{lij}}}{4P_{ij}P_{ji}}\,, \tag{5.8}$$

where,

$$A = \left[\rho Q_{kii}\left(P^{-1}\right)_{kl} Q_{ljj} - \frac{1}{2}\rho Q_{kij}\left(P^{-1}\right)_{kl} Q_{lij} + 2P_{ij}P_{ji} + P_{ii}P_{jj} - \rho R_{iijj}\right]\,.$$

The expression for σ is very similar to the one for the fourteen-moment closure [31]. It is slightly altered so that σ is zero only when *all* entries of the heat-flux tensor are zero.

5.4 Closing Fluxes on the Physical Realizability Boundary

As with the fourteen-moment case, numerical investigation has shown that, on the physical realizability boundary for R_{iijj}, the distribution function exist only on a sphere in velocity space. Once again, since the distribution is only non-zero on a sphere, it is possible to relate

higher-order contracted moments to lower-order moments. It is again possible to obtain expressions for R_{ijkk} and S_{ijjkk} on the boundary of realizability as

$$R_{ijkk} = Q_{ijl}\left(P^{-1}\right)_{lm} Q_{mkk} + \frac{P_{ij}P_{kk}}{\rho}\,, \tag{5.9}$$

$$S_{ijjkk} = P^{-1}_{kn}P^{-1}_{lm}Q_{npp}Q_{mjj}Q_{ikl} + 2\frac{P_{jj}Q_{ikk}}{\rho}\,. \tag{5.10}$$

As opposed to the fourteen-moment model, the closing fluxes, R_{ijkk} and S_{ijjkk}, are only functions of known moments. Unfortunately, the closing flux R_{ijkl} is not a contracted moment and therefore it is not possible to use this technique to obtain a closed form expression on the physical realizability boundary. However, since the form of the once-contracted fourth-order moment is known, extra information is available to base the approximation of the closing flux R_{ijkl}. It is found that R_{ijkl} can be well approximated on the boundary as,

$$\begin{aligned}
R_{ijkl} = \frac{1}{2}\Bigg[&Q_{ijm}\left(P^{-1}\right)_{mn} Q_{nkl} + Q_{ilm}\left(P^{-1}\right)_{mn} Q_{njk} + Q_{ikm}\left(P^{-1}\right)_{mn} Q_{njl} \\
&- \frac{2}{7}\Big(Q_{iom}\left(P^{-1}\right)_{mn} Q_{noj}\delta_{kl} + Q_{iom}\left(P^{-1}\right)_{mn} Q_{nok}\delta_{jl} + Q_{iom}\left(P^{-1}\right)_{mn} Q_{nol}\delta_{jk} \\
&\quad + Q_{jom}\left(P^{-1}\right)_{mn} Q_{nok}\delta_{il} + Q_{jom}\left(P^{-1}\right)_{mn} Q_{nol}\delta_{ik} + Q_{kom}\left(P^{-1}\right)_{mn} Q_{nol}\delta_{ij} \\
&\quad - \frac{1}{5}Q_{pom}\left(P^{-1}\right)_{mn} Q_{nop}(\delta_{ij}\delta_{kl} + \delta_{ik}\delta_{jl} + \delta_{il}\delta_{jk})\Big)\Bigg] \\
&+ \frac{1}{14}\Bigg[Q_{ijm}\left(P^{-1}\right)_{mn} Q_{npp}\delta_{kl} + Q_{ikm}\left(P^{-1}\right)_{mn} Q_{npp}\delta_{jl} + Q_{ilm}\left(P^{-1}\right)_{mn} Q_{npp}\delta_{jk} \\
&\quad + Q_{jkm}\left(P^{-1}\right)_{mn} Q_{npp}\delta_{il} + Q_{jlm}\left(P^{-1}\right)_{mn} Q_{npp}\delta_{ik} + Q_{klm}\left(P^{-1}\right)_{mn} Q_{npp}\delta_{ij} \\
&\quad - \frac{1}{5}Q_{mmn}\left(P^{-1}\right)_{np} Q_{pqq}(\delta_{ij}\delta_{kl} + \delta_{ik}\delta_{jl} + \delta_{il}\delta_{jk})\Bigg] \\
&+ \frac{1}{\rho}\frac{3}{10}\Bigg[P_{ij}P_{kl} + P_{ik}P_{jl} + P_{il}P_{jk} - \frac{2}{7}\Big(\left(P^2\right)_{ij}\delta_{kl} + \left(P^2\right)_{ik}\delta_{jl} + \left(P^2\right)_{il}\delta_{jk} + \left(P^2\right)_{jk}\delta_{il} \\
&\quad + \left(P^2\right)_{jl}\delta_{ik} + \left(P^2\right)_{kl}\delta_{ij} - \frac{1}{5}\left(P^2\right)_{mm}(\delta_{ij}\delta_{kl} + \delta_{ik}\delta_{jl} + \delta_{il}\delta_{jk})\Big)\Bigg] \\
&+ \frac{1}{\rho}\frac{1}{10}\Bigg[P_{ij}P_{mm}\delta_{kl} + P_{ik}P_{mm}\delta_{jl} + P_{il}P_{mm}\delta_{jk} + P_{jk}P_{mm}\delta_{il} + P_{jl}P_{mm}\delta_{ik} + P_{kl}P_{mm}\delta_{ij} \\
&\quad - \frac{1}{5}P_{mm}P_{nn}(\delta_{ij}\delta_{kl} + \delta_{ik}\delta_{jl} + \delta_{il}\delta_{jk})\Bigg]\,.
\end{aligned} \tag{5.11}$$

This is obtained by writing down all expressions that contracts to the correct contracted moments and maintain a linear and rotational invariance.

To better illustrate the process used to build this expression, the building procedure of the first component of Eq. (5.11) is demonstrated as an example. An initial expression is chosen such that it is rotationally and translationally invariant, in this case

$$Q_{ijm}\left(P^{-1}\right)_{mn}Q_{nkl}+Q_{ilm}\left(P^{-1}\right)_{mn}Q_{njk}+Q_{ikm}\left(P^{-1}\right)_{mn}Q_{njl}\,. \tag{5.12}$$

When contracted on the k and l indices, this expression yields,

$$Q_{ijm}\left(P^{-1}\right)_{mn}Q_{nkk}+\boldsymbol{2Q_{ikm}\left(P^{-1}\right)_{mn}Q_{njk}}\,, \tag{5.13}$$

which differs from the contracted form shown in Eq. (5.9). In order for the contraction to be in agreement with the contracted closing flux the second term in bold in Eq. (5.13) must be removed, correction terms are added to the approximation, the first one being,

$$\begin{aligned}-\frac{2}{7}\Big(&Q_{iom}\left(P^{-1}\right)_{mn}Q_{noj}\delta_{kl}+Q_{iom}\left(P^{-1}\right)_{mn}Q_{nok}\delta_{jl}+Q_{iom}\left(P^{-1}\right)_{mn}Q_{nol}\delta_{jk}\\&+Q_{jom}\left(P^{-1}\right)_{mn}Q_{nok}\delta_{il}+Q_{jom}\left(P^{-1}\right)_{mn}Q_{nol}\delta_{ik}+Q_{kom}\left(P^{-1}\right)_{mn}Q_{nol}\delta_{ij}\,.\end{aligned} \tag{5.14}$$

Once contracted Eq. (5.14) has the form,

$$-\frac{2}{7}\left(7Q_{iom}\left(P^{-1}\right)_{mn}Q_{noj}+\boldsymbol{Q_{kom}\left(P^{-1}\right)_{mn}Q_{nok}\delta_{ij}}\right)\,. \tag{5.15}$$

The first term of Eq. (5.15) subtract perfectly the term in bold in Eq. (5.13), however the first correction term also has a term that needs to be removed as shown in bold in Eq (5.15). Therefore, a second correction term is added,

$$-\frac{1}{5}Q_{pom}\left(P^{-1}\right)_{mn}Q_{nop}\left(\delta_{ij}\delta_{kl}+\delta_{ik}\delta_{jl}+\delta_{il}\delta_{jk}\right)\,, \tag{5.16}$$

which contracts to,

$$-Q_{pom}\left(P^{-1}\right)_{mn}Q_{nop}\delta_{ij}\,. \tag{5.17}$$

When added together, this yield an expression that contracts to the contracted expression in Eq. (5.9). The same process is then repeated for various rotationally and translationally invariant expressions as well as for the analogous pressure components. From those expressions, a combination is carefully selected such that it yields the closest fit to the exact solution for the closing flux. That selection and combination is done through thorough experimentations, observations and fittings of these expression. The obtained expression is both translationally and rotationally invariant and also contracts to the correct form, recovering

expressions for the contracted fourth-order moments.

5.5 Closing Fluxes at the Gaussian Level

At the Gaussian level it is possible to integrate R_{ijkk} and R_{ijkl} analytically,

$$R_{ijkk} = \frac{1}{\rho}\left(P_{ij}P_{kk} + 2P_{ik}P_{kj}\right) , \tag{5.18}$$

$$R_{ijkl} = \frac{1}{\rho}\left(P_{ij}P_{kl} + P_{ik}P_{jl} + P_{il}P_{jk}\right) . \tag{5.19}$$

Again, since for the Gaussian distribution function all odd random velocity moments are zero, the expression for S_{ijjkk} is simply zero, however it is possible to find its derivative. Again, this is shown in more detail by M$^{\text{c}}$Donald and Torrilhon [31] and yields

$$\begin{aligned}\frac{\partial S_{ijjkk}}{\partial Q_{mnn}} = \frac{1}{\rho}\Big[&2P_{il}\left(P_{\alpha\alpha}\right)^3 + 12P_{il}\left(P^3\right)_{\alpha\alpha} + 14\left(P^2\right)_{\alpha\alpha}\left(P^2\right)_{il} + 20P_{\alpha\alpha}\left(P^3\right)_{il} \\ &+ 20\left(P^4\right)_{il} - 2\left(P^2\right)_{\alpha\alpha}P_{\beta\beta}P_{il} - 6\left(P_{\alpha\alpha}\right)^2\left(P^2\right)_{il}\Big]B^{-1}_{lm} \\ = W_{im} ,\end{aligned}$$

where,

$$B_{lm} = 2P_{lm}\left(P^2\right)_{\alpha\alpha} + 4\left(P^3\right)_{lm} .$$

It is then possible to approximate the value of S_{ijjkk} near a Gaussian as,

$$S_{ijjkk} = W_{im}Q_{mnn} . \tag{5.20}$$

5.6 Closing Fluxes Approximation

By using the expressions for the closing fluxes at the realizability boundary and at the Gaussian level, as well as the modified parabolic mapping, it is possible to develop expressions for all closing fluxes in all moment space. The approximations for the fourth-order closing

fluxes are,

$$R_{ijkk} = Q_{ijl}\left(P^{-1}\right)_{lm} Q_{mkk} + \frac{1-\sigma}{2\sigma} Q_{lik}\left(P^{-1}\right)_{lm} Q_{mkj} + \frac{2(1-\sigma)P_{ik}P_{kj} + P_{ij}P_{kk}}{\rho} \tag{5.21}$$

$$\begin{aligned}
R_{ijkl} = \frac{1}{2}\Bigg[& Q_{ijm}\left(P^{-1}\right)_{mn} Q_{nkl} + Q_{ilm}\left(P^{-1}\right)_{mn} Q_{njk} + Q_{ikm}\left(P^{-1}\right)_{mn} Q_{njl} \\
& - \frac{2}{7}\Big(Q_{iom}\left(P^{-1}\right)_{mn} Q_{noj}\delta_{kl} + Q_{iom}\left(P^{-1}\right)_{mn} Q_{nok}\delta_{jl} + Q_{iom}\left(P^{-1}\right)_{mn} Q_{nol}\delta_{jk} \\
& + Q_{jom}\left(P^{-1}\right)_{mn} Q_{nok}\delta_{il} + Q_{jom}\left(P^{-1}\right)_{mn} Q_{nol}\delta_{ik} + Q_{kom}\left(P^{-1}\right)_{mn} Q_{nol}\delta_{ij} \\
& - \frac{1}{5} Q_{pom}\left(P^{-1}\right)_{mn} Q_{nop}(\delta_{ij}\delta_{kl} + \delta_{ik}\delta_{jl} + \delta_{il}\delta_{jk})\Big)\Bigg] \\
& + \frac{1}{14}\Bigg[Q_{ijm}\left(P^{-1}\right)_{mn} Q_{npp}\delta_{kl} + Q_{ikm}\left(P^{-1}\right)_{mn} Q_{npp}\delta_{jl} + Q_{ilm}\left(P^{-1}\right)_{mn} Q_{npp}\delta_{jk} \\
& + Q_{jkm}\left(P^{-1}\right)_{mn} Q_{npp}\delta_{il} + Q_{jlm}\left(P^{-1}\right)_{mn} Q_{npp}\delta_{ik} + Q_{klm}\left(P^{-1}\right)_{mn} Q_{npp}\delta_{ij} \\
& - \frac{1}{5} Q_{mmn}\left(P^{-1}\right)_{np} Q_{pqq}(\delta_{ij}\delta_{kl} + \delta_{ik}\delta_{jl} + \delta_{il}\delta_{jk})\Bigg] \\
& + \frac{1}{\rho}\Bigg[\Big(1+\Big(\frac{3}{10}-1\Big)\sigma\Big)\Big(P_{ij}P_{kl}+P_{ik}P_{jl}+P_{il}P_{jk}\Big) - \sigma\frac{3}{10}\frac{2}{7}\Big(\left(P^2\right)_{ij}\delta_{kl} + \left(P^2\right)_{ik}\delta_{jl} + \left(P^2\right)_{il}\delta_{jk} \\
& + \left(P^2\right)_{jk}\delta_{il} + \left(P^2\right)_{jl}\delta_{ik} + \left(P^2\right)_{kl}\delta_{ij} - \frac{1}{5}\left(P^2\right)_{mm}(\delta_{ij}\delta_{kl} + \delta_{ik}\delta_{jl} + \delta_{il}\delta_{jk})\Big)\Bigg] \\
& + \sigma\frac{1}{\rho}\frac{1}{10}\Bigg[P_{ij}P_{mm}\delta_{kl} + P_{ik}P_{mm}\delta_{jl} + P_{il}P_{mm}\delta_{jk} + P_{jk}P_{mm}\delta_{il} + P_{jl}P_{mm}\delta_{ik} + P_{kl}P_{mm}\delta_{ij} \\
& - \frac{1}{5} P_{mm}P_{nn}(\delta_{ij}\delta_{kl} + \delta_{ik}\delta_{jl} + \delta_{il}\delta_{jk})\Bigg] \\
& + \frac{(1-\sigma)}{14\sigma}\Bigg[Q_{mio}\left(P^{-1}\right)_{mn} Q_{njo}\delta_{kl} + Q_{mio}\left(P^{-1}\right)_{mn} Q_{nko}\delta_{jl} + Q_{mio}\left(P^{-1}\right)_{mn} Q_{nlo}\delta_{jk} \\
& + Q_{mjo}\left(P^{-1}\right)_{mn} Q_{nko}\delta_{il} + Q_{mjo}\left(P^{-1}\right)_{mn} Q_{nlo}\delta_{ik} + Q_{mko}\left(P^{-1}\right)_{mn} Q_{nlo}\delta_{ij} \\
& - \frac{1}{5} Q_{mpo}\left(P^{-1}\right)_{mn} Q_{npo}(\delta_{ij}\delta_{kl} + \delta_{ik}\delta_{jl} + \delta_{il}\delta_{jk})\Bigg] .
\end{aligned} \tag{5.22}$$

The approximation both contract to the correct expression to match the contracted fourth-order tensor and is rotationally invariant. The approximation for the fifth-order closing flux is expressed as,

$$S_{ijjkk} = \frac{1}{\sigma^2} P^{-1}_{kn} P^{-1}_{lm} Q_{npp} Q_{mjj} Q_{ikl} + 2\sigma^{\frac{1}{2}}\frac{P_{jj}Q_{ikk}}{\rho} + \left(1-\sigma^{\frac{1}{2}}\right) W_{im} Q_{mnn} . \tag{5.23}$$

These expressions are developed to match, as closely as possible, the exact closing fluxes for an axisymmetric distribution function in velocity space and one-dimension in physical space.

5.7 Fidelity of the Approximation and Region of Hyperbolicity

To demonstrate the accuracy of the approximation for the closing fluxes, some comparison to the exact maximum-entropy closing fluxes are plotted. Figures 5.1a, 5.1c, and 5.1e show the closing flux, R_{xxxx}, obtained from the approximation on the left as compared to the maximum-entropy value on the right. These are computed for the non-dimensional case where $\rho = 1$ and $P_{ii} = 1$. The results are plotted for a value of $Q_{xii} = 0.1$ for the case where $\sigma = 0.2$ and a value of $Q_{xii} = 0.2$ for the remaining cases. The value of Q_{xxx} is varied such that the set value for Q_{xii} is conserved. The moment P_{xx} is varied from 0.1 to 0.9 in a manner where $P_{ii} = 1$. The values of σ are respectively 0.2, 0.5 and 0.9 for the three graphs. These plots were chosen because they represent a large part of moment space. The approximation shows a good overall agreement with the exact solution for the closing flux.

To conserve the advantages related to the hyperbolic first-order nature of the model it is important to have eigenvalues of the flux Jacobian that are strictly real. If the eigenvalues have a non-zero imaginary part, then hyperbolicity is lost. Figures 5.1b, 5.1d and 5.1f show the largest ratio of the imaginary part of the eigenvalues over its norm. The plots correspond to the previous cases shown, respectively.

While the approximation does not offer a globally hyperbolic closure through all moment space, it does preserve hyperbolicity in most of moment space. Most regions of non-hyperbolicity present only weak imaginary parts and only a limited portion of moment space show strongly non-hyperbolic behaviour.

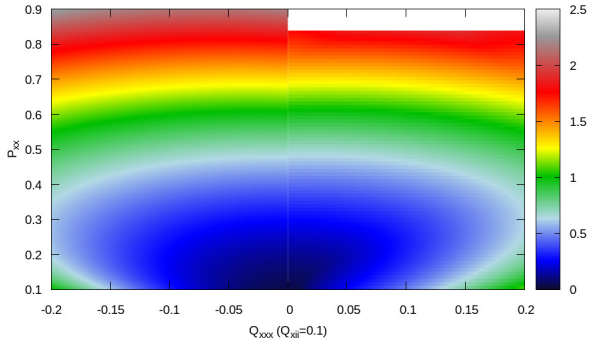

(a) Closing flux R_{xxxx} at $\sigma = 0.2$, exact solution on the right and approximation on the left

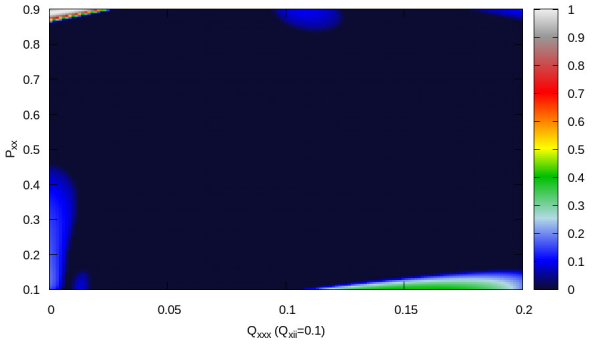

(b) Largest imaginary part of the eigenvalue over its norm for $\sigma = 0.2$

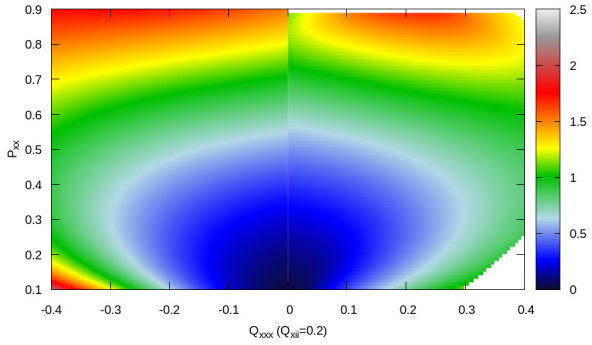

(c) Closing flux R_{xxxx} at $\sigma = 0.5$, exact solution on the right and approximation on the left

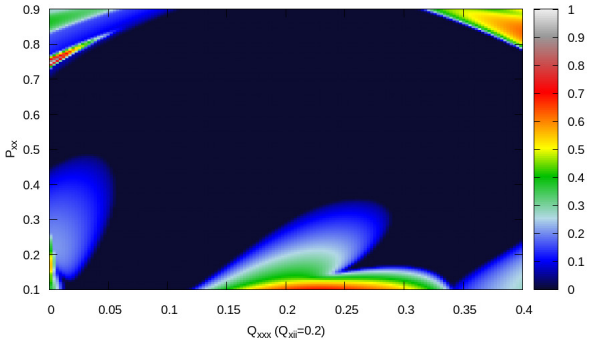

(d) Largest imaginary part of the eigenvalue over its norm for $\sigma = 0.5$

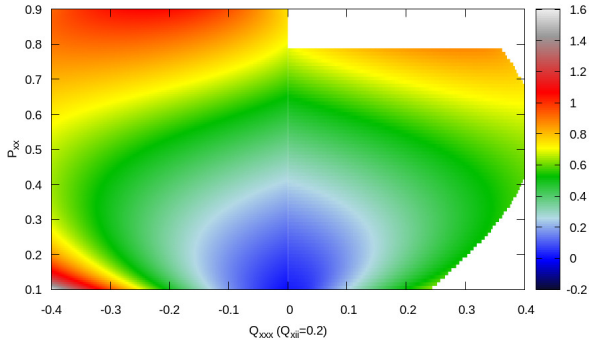

(e) Closing flux R_{xxxx} at $\sigma = 0.9$, exact solution on the right and approximation on the left

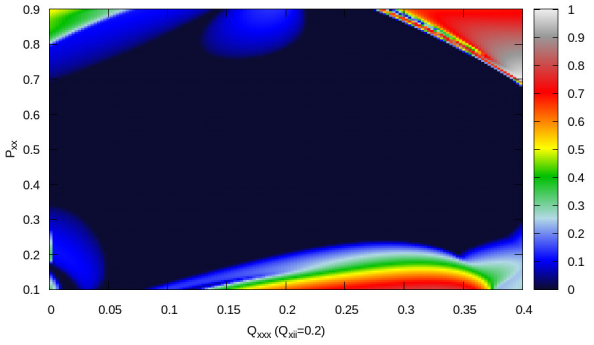

(f) Largest imaginary part of the eigenvalue over its norm for $\sigma = 0.9$

Figure 5.1: Comparison of the approximated closing flux with the exact solution for various sigma and associated hyperbolicity plot.

Chapter 6

Dispersion Analysis of the Twenty-One Moment Closure

Hyperbolic-relaxation system of equations are characterized by a dispersive wave behaviour. When subjected to a perturbation, the apparent speed of propagation and damping rate depends on the frequency and wave number of the disturbance applied. A dispersion analysis is used to asses the reaction of the system to a perturbation and also gives insight into the overall stability of the system. The dispersion analysis yields the apparent wavespeeds of different modes as a function of the Knudsen number, as well as their respective damping rates. The state chosen to perform the analysis is the one where $\rho = 1$, $u_i = 0$, $P_{xx} = P_{yy} = P_{zz} = 1$, $P_{xy} = 0$, and for which the heat flux is zero, this is because that is the equilibrium state where the source term is zero. It is expected that at low Knudsen numbers, corresponding to a collision dominated regime, the Euler wavespeeds be recovered. The technique used to determine the dispersion wave and the amplification factors are shown in details by Hittinger [20] and Brown [6]. In one-dimension, the system of hyperbolic-relaxation equation is

$$\frac{\partial \boldsymbol{U}}{\partial t} + \frac{\partial \boldsymbol{F}}{\partial x} = \boldsymbol{S}\,, \tag{6.1}$$

and since, at the analysis point, the source term, $\boldsymbol{S}$, is zero, and since the analysis relies on small perturbations, it can be linearized as

$$\frac{\partial \boldsymbol{U}}{\partial t} + \boldsymbol{A}\frac{\partial \boldsymbol{U}}{\partial x} = \boldsymbol{Q}\boldsymbol{U}\,, \tag{6.2}$$

where $\boldsymbol{A} = \frac{\partial \boldsymbol{F}}{\partial \boldsymbol{U}}$ and $\boldsymbol{Q} = \frac{\partial \boldsymbol{S}}{\partial \boldsymbol{U}}$. This is expected to well approximate the full non-linear system for small perturbation in $\boldsymbol{U}$. Note that, in this analysis, the solution vector used is,

$$\boldsymbol{U} = \begin{bmatrix} \rho \\ \rho u_x \\ \rho u_y \\ \rho u_x u_x + P_{xx} \\ \rho u_x u_y + P_{xy} \\ \rho u_y u_y + P_{yy} \\ P_{zz} \\ \rho u_x u_x u_x + 3u_x P_{xx} + Q_{xxx} \\ \rho u_x u_y u_y + u_x P_{yy} + 2u_y P_{xy} + Q_{xyy} \\ u_x P_{zz} + Q_{xzz} \\ \rho u_y u_x u_x + u_y P_{xx} + 2u_x P_{xy} + Q_{yxx} \\ \rho u_y u_y u_y + 3u_y P_{yy} + Q_{yyy} \\ u_y P_{zz} + Q_{yzz} \\ \rho(u_x u_x u_x u_x + 2u_x u_x u_y u_y + u_y u_y u_y u_y) \\ +2(u_x u_x + u_y u_y)(P_{xx} + P_{yy} + P_{zz}) + 4(u_x u_x P_{xx} + 2u_x u_y P_{xy} + u_y u_y P_{yy}) \\ +4u_x(Q_{xxx} + Q_{xyy} + Q_{xzz}) + 4u_y(Q_{yxx} + Q_{yyy} + Q_{yzz}) + R_{iijj} \end{bmatrix}. \tag{6.3}$$

It is possible to express Eq. (6.2) as an operator acting on $\boldsymbol{U}$

$$\left(\boldsymbol{I}\frac{\partial}{\partial t} + \boldsymbol{A}\frac{\partial}{\partial x} - \boldsymbol{Q}\right)\boldsymbol{U} = 0\,. \tag{6.4}$$

In order to study the behaviours of different modes of waves, the initial condition can be

chosen to be

$$\boldsymbol{U}(x,0) = \boldsymbol{U_0} e^{-i\kappa x}\,, \tag{6.5}$$

where $\kappa \in \mathbb{R}$ correspond to the wave number. The ansatz solution is then

$$\boldsymbol{U}(x,t) = \boldsymbol{V}(t) e^{-i\kappa x}\,. \tag{6.6}$$

By substituting Eq. (6.6) into Eq (6.4), the problem becomes an ordinary differential equation

$$\frac{d\boldsymbol{V}}{dt} = \left(i\kappa \boldsymbol{A} + \boldsymbol{Q}\right)\boldsymbol{V}\,, \tag{6.7}$$

and the solution for $\boldsymbol{V}(t)$ has the form

$$\boldsymbol{V}(t) = e^{it(\kappa \boldsymbol{A} - i\boldsymbol{Q})}\boldsymbol{U}_0\,. \tag{6.8}$$

The Jordan canonical form of $\kappa\boldsymbol{A} - i\boldsymbol{Q}$ is expressed as,

$$\kappa\boldsymbol{A} - i\boldsymbol{Q} = \boldsymbol{R}\left(\boldsymbol{\Lambda} + \boldsymbol{N}\right)\boldsymbol{R}^{-1}\,, \tag{6.9}$$

where $\boldsymbol{R}$ is the transition matrix, $\boldsymbol{\Lambda}$ is the diagonal matrix of eigenvalues of $\kappa\boldsymbol{A} - i\boldsymbol{Q}$ and where $\boldsymbol{N}$ is the nilpotent matrix which is zero if $\kappa\boldsymbol{A} - i\boldsymbol{Q}$ is diagonizable. The solution for $V(t)$ in Eq. (6.8) can be rewritten as,

$$\begin{aligned}
\boldsymbol{V}(t) &= e^{it\boldsymbol{R}(\boldsymbol{\Lambda}+\boldsymbol{N})\boldsymbol{R}^{-1}}\boldsymbol{U}_0 \\
&= \boldsymbol{R}e^{it(\boldsymbol{\Lambda}+\boldsymbol{N})}\boldsymbol{R}^{-1}\boldsymbol{U}_0 \\
&= \boldsymbol{R}e^{it\boldsymbol{\Lambda}}\left(\boldsymbol{I} + it\boldsymbol{N}\right)\boldsymbol{R}^{-1}\boldsymbol{U}_0\,.
\end{aligned} \tag{6.10}$$

By substituting Eq. (6.10) into Eq. (6.6), the solution to the original system is obtained,

$$\boldsymbol{U}(x,t) = \boldsymbol{R}e^{i(t\boldsymbol{\Lambda} - \kappa x\boldsymbol{I})}\left(\boldsymbol{I} + it\boldsymbol{N}\right)\boldsymbol{R}^{-1}\boldsymbol{U}_0\,. \tag{6.11}$$

To obtain the apparent wavespeeds and the damping rate of the system, it is needed to find the eigenvalues of $\kappa\boldsymbol{A} - i\boldsymbol{Q}$ by solving

$$\det\left(\kappa\boldsymbol{A} - i\boldsymbol{Q} - \lambda\boldsymbol{I}\right) = 0\,. \tag{6.12}$$

In this analysis, κ is proportional to the Knudsen number and the Jacobians are evaluated at equilibrium. The obtained eigenvalues are typically complex in nature, $\lambda = \lambda_R + i\lambda_I$. The

apparent wavespeeds of the system in Eq. (6.8) are described by

$$\omega = \frac{\lambda_R}{\kappa} \,. \tag{6.13}$$

The attenuation rate of the waves is, on the other hand, described by

$$e^{-\lambda_I} \,. \tag{6.14}$$

As shown in Figure 6.1a, the apparent wavespeeds of the system are well behaved. They are finite and show a smooth transition through the Knudsen number domain while maintaining a damping rate between zero and one. Since k is the frequency of the applied perturbation on the system, a low frequency indicates a slow process where the collision have time to impact the state. Conversely, high frequencies indicates a fast process where collisions do not have time to impact the state. On the right-hand side are the apparent wavespeeds for large Knudsen number, corresponding to a free molecular regime. In this collisionless limit, the eleven distinct non-dimensional apparent wavespeeds have values 0.0, ± 0.833523, ± 0.999995, ± 1.30316, ± 1.73132 and ± 2.43564. When redimensionalized, these x-direction wavespeeds are scaled by $\sqrt{P_{xx}/\rho}$. As the Knudsen number is decreased, the maximum and minimum wavespeeds recovered on the left-hand side of the graph correspond the Euler wavespeeds.

Figure 6.1b shows the damping rate of the modes with respect to the Knudsen number. In order to have a stable system it is important that the damping rate remains lower than one. The dispersion analysis obtained with the approximated closure correspond perfectly to the one obtained with the exact closure obtained by solving the entropy maximization problem.

For the five- and ten-moment closure, a detailed analysis of the eigensystem of the flux Jacobian allows one to study the information and physical phenomena carried by each wave. Unfortunately, for both the fourteen- and twenty-one-moment closures, the system is far too complex for a similar analysis.

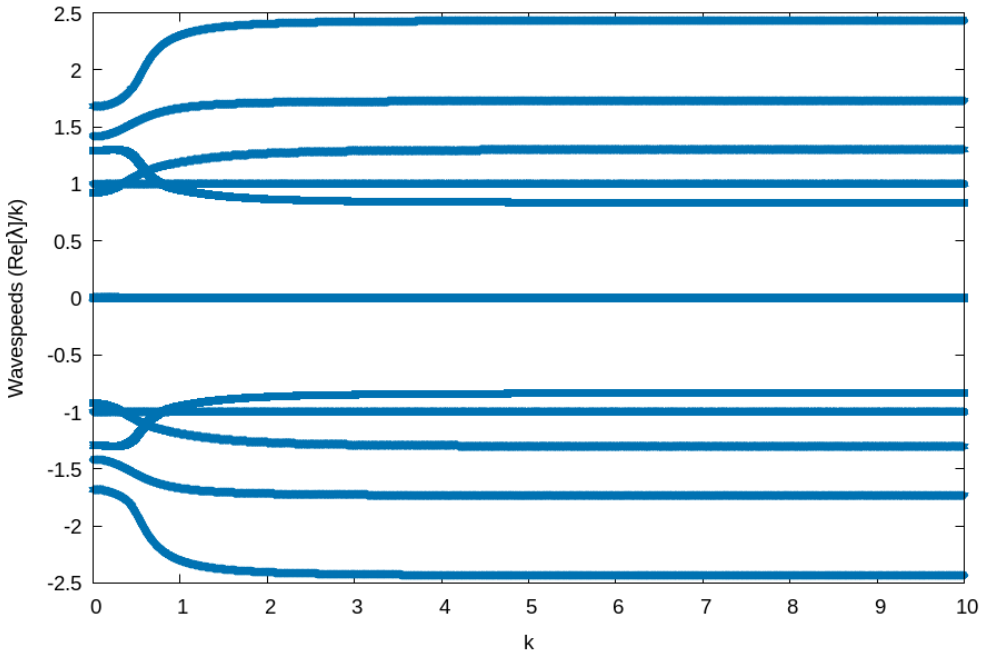

(a) Wavespeeds of different modes.

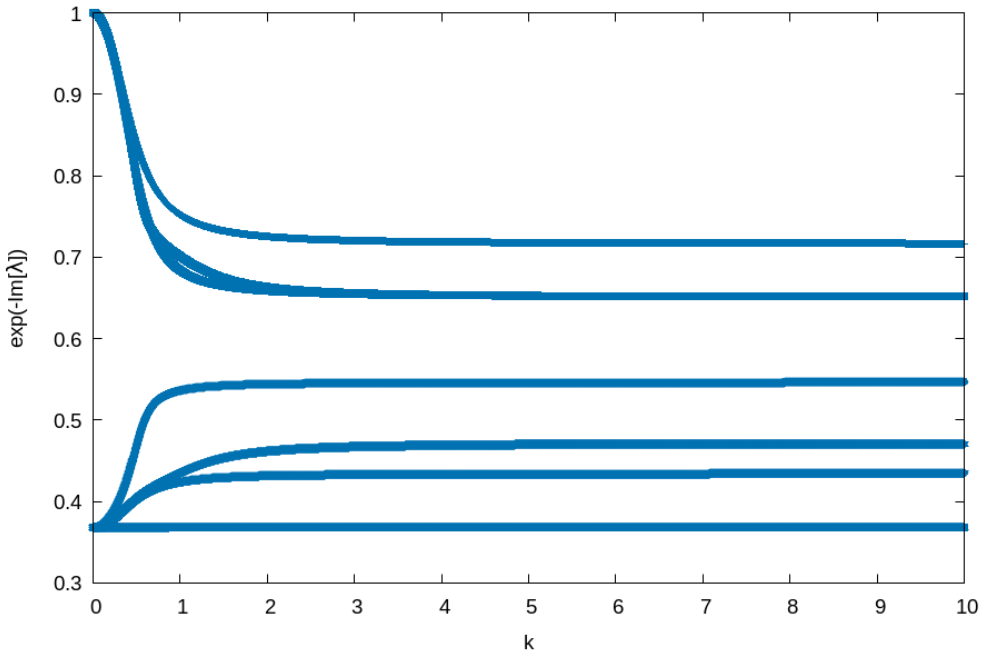

(b) Damping rates of different modes.

Figure 6.1: Dispersion analysis of the proposed twenty-one moment model.

Chapter 7

Novel Approximation for the Knudsen-Layer Boundary-Condition

In order to obtain a physically accurate solution, it is important to have a proper treatment of solid-wall boundary conditions. It is important to recover the proper interaction between the particles and the wall. Appropriate solid-wall boundary-condition for moment-closure models are not trivial. Solutions to the treatment of solid-wall boundary conditions have been proposed, notably the ones by Tensuda [42] and Khieu [26]. A common technique is to assume an infinitesimally thin Knudsen layer at the wall [15]. In this layer, the velocity distribution function of the fluid is described as a combination of the distribution of the particles coming from the interior flow-field and that of the particles reflected from the wall. All particles with a velocity directed towards the wall have statistics described by the distribution function near the wall. For the particles with a velocity directed away from the wall, an accommodation coefficient, α, is defined. A specular reflection is defined to be when α is zero. In this case, the particles are reflected from the wall in a specular manner. On the other hand, a diffusive reflection is obtained when α is one, in which case the particles reflected from the wall are described by a Maxwell-Boltzmann distribution with the wall temperature, T_W, and wall velocity, u_W. For a value of α between zero and one, the reflected particles are expressed by a combination of the reflected incoming distribution and the Maxwell-Boltzmann distribution function. The resulting distribution function in the Knudsen layer for a right vertical solid-wall, as illustrated in Figure 7.1, is therefore

expressed as,

$$\mathcal{F}_{Kn} = \mathcal{F}^{+} + \mathcal{F}^{-} \,, \tag{7.1}$$

where $\mathcal{F}^{+}$ and $\mathcal{F}^{-}$ are

$$\mathcal{F}^{+} = \begin{cases} 0 & v_x < 0 \\ \mathcal{F}(v_x, v_y, v_z) & v_x > 0 \end{cases} \tag{7.2}$$

$$\mathcal{F}^{-} = \begin{cases} \alpha\mathcal{M}(v_x, v_y, v_z) + (1-\alpha)\mathcal{F}(-v_x, v_y, v_z) & v_x < 0 \\ 0 & v_x > 0 \end{cases} \tag{7.3}$$

and where $\mathcal{F}$ is the distribution function of the interior flow and $\mathcal{M}$ is the Maxwell-Boltzmann distribution with velocity and temperature of the wall. The fluxes at the boundary are obtained by computing the following integral,

$$\boldsymbol{F}_{BC} = \int_{-\infty}^{\infty}\int_{-\infty}^{\infty}\int_{-\infty}^{\infty} m v_x \boldsymbol{W} \left(\mathcal{F}^{+} + \mathcal{F}^{-}\right) dv_x dv_y dv_z \,. \tag{7.4}$$

By assuming that the normal bulk velocity to the wall is zero, which means that the net particle flux through the wall is also zero, it is possible to determine the corresponding density of the reflected particles,

$$\int_{-\infty}^{\infty}\int_{-\infty}^{\infty}\int_{-\infty}^{\infty} m v_x \left(\mathcal{F}^{+} + \mathcal{F}^{-}\right) dv_x dv_y dv_z = 0 \,. \tag{7.5}$$

For a Maxwell-Boltzmann distribution with a temperature, T_w, and an accommodation coefficient, α, of one the previous equation gives,

$$\rho_{\mathcal{M}} = \sqrt{\frac{2\pi}{R_s T_w}} \int_{-\infty}^{\infty}\int_{-\infty}^{\infty}\int_{-\infty}^{\infty} m v_x \mathcal{F}^{+} dv_x dv_y dv_z \,. \tag{7.6}$$

Once this density is obtained, all information related to the wall distribution function is known and the boundary fluxes can be computed.

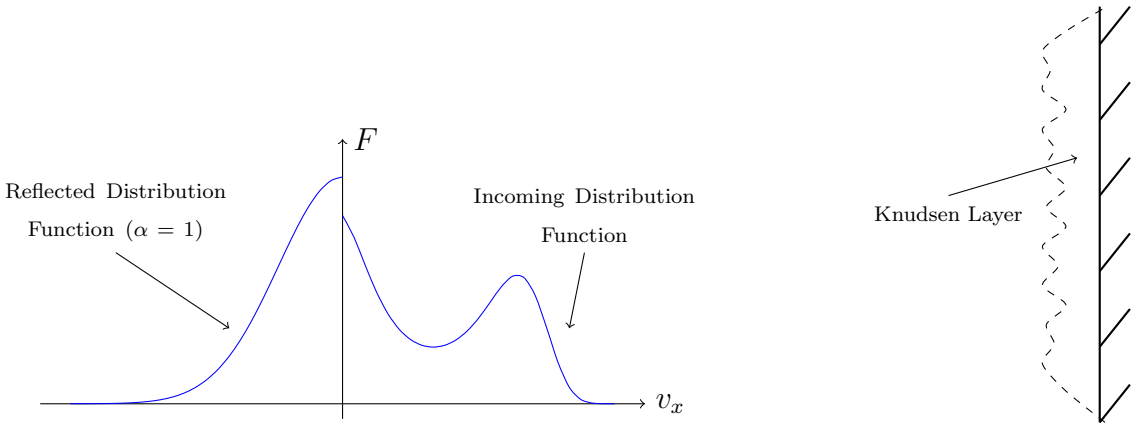

Figure 7.1: Knudsen wall boundary and associated distribution function.

7.1 Approximation for the Half Integral of the Interior Flow Distribution Function

In order to derive the Knudsen layer, the following integral of the interior flow distribution function needs to be performed,

$$\boldsymbol{F}^{+} = \int_{-\infty}^{\infty}\int_{-\infty}^{\infty}\int_{0}^{\infty} mv_x \boldsymbol{W}\mathcal{F} dv_x dv_y dv_z \,. \tag{7.7}$$

For the 5- and 10-moment model of maximum entropy, the distribution function can be integrated analytically in closed form and, further, be used to determine the boundary fluxes associated with a Knudsen layer. However, since for higher-order distribution functions, it is impossible to evaluate the integrals in closed form, a different approach must be developed to approximate the half-flux of these distribution function.

While higher-order distribution functions cannot be integrated in closed form, they can be evaluated at equilibrium. That is, any order moment can be evaluated at equilibrium. To approximate the half flux out of equilibrium, an extrapolation from its value at equilibrium is proposed. The half-flux and the half-flux Jacobian is first evaluated at equilibrium for the same density, bulk velocity, and thermodynamic pressure as the flow and are denoted $\boldsymbol{F}^{+}_{\mathcal{M}}$ and $\frac{d\boldsymbol{F}^{+}}{d\boldsymbol{U}}\Big|_{\mathcal{M}}$ respectively. The half-flux for the higher-order distribution is then linearly extrapolated from the equilibrium half-flux using the flux-Jacobian evaluated at equilibrium as shown in Eq. (7.8).

$$\tilde{\boldsymbol{F}}^{+}_{\mathcal{F}} = \boldsymbol{F}^{+}_{\mathcal{M}} + \frac{d\boldsymbol{F}^{+}}{d\boldsymbol{U}}\bigg|_{\mathcal{M}} (\boldsymbol{U}_{\mathcal{F}} - \boldsymbol{U}_{\mathcal{M}}) \,. \tag{7.8}$$

This insures that the correct boundary flux is recovered when the flow at the wall is at equilibrium. From Eq. 7.4, the fluxes at the boundary can be rewritten as,

$$\boldsymbol{F}_{BC} = \tilde{\boldsymbol{F}}_{\mathcal{F}}^{+} + \int_{-\infty}^{\infty}\int_{-\infty}^{\infty}\int_{-\infty}^{0} mv_x \boldsymbol{W}\mathcal{M}dv_x dv_y dv_z \,, \tag{7.9}$$

where the density of the Maxwellian, $\mathcal{M}$, is found using Eq. 7.6.

7.1.1 Validation of the New Boundary Condition

To assess the performance of the proposed solid-wall boundary condition, a Couette flow is solved for various Knudsen numbers, from the continuum to the rarefied regime. The goal is to compare the normalized shear stress and slip velocity in the continuum and rarefied regimes as well as its transition between the two.

At low Knudsen number, the shear stress is expected to vary linearly with the Knudsen number as predicted by the Navier-Stokes equations. As the Knudsen number is increased past the transition regime, the shear stress is expected to deviate from the Navier-Stokes prediction until it reaches the free-molecular shear stress. That is because the flow is expected to slip at the wall. This should be observable when looking at the slip velocity. For high Knudsen number, the velocity slip is expected to be infinite and the flow to be stagnant.

The normalized shear-stress and slip-velocity for a Couette flow between two plates going at the same constant speed but in opposite directions, is shown in Figure 7.3 for varying Knudsen numbers. While there is a discrepancy in the free-molecular regime, the results follow closely the Lees approximate solution[45] in the continuum and transition regime given by,

$$\bar{P}_{xy} = \frac{2\ \mathrm{Kn}}{1 + 2\ \mathrm{Kn}} \qquad\qquad \bar{u}_{\mathrm{slip}} = \frac{1}{1 + 2\ \mathrm{Kn}} \,. \tag{7.10}$$

The deviation in the free-molecular regime is due to some weakness in the extrapolation of the half-flux from the Maxwellian half-flux but also due to some deficiency in the Knudsen layer treatment of solid-wall boundary conditions. This newly proposed solid-wall boundary condition will be used to solve multi-dimensional cases in the continuum and transition regime.

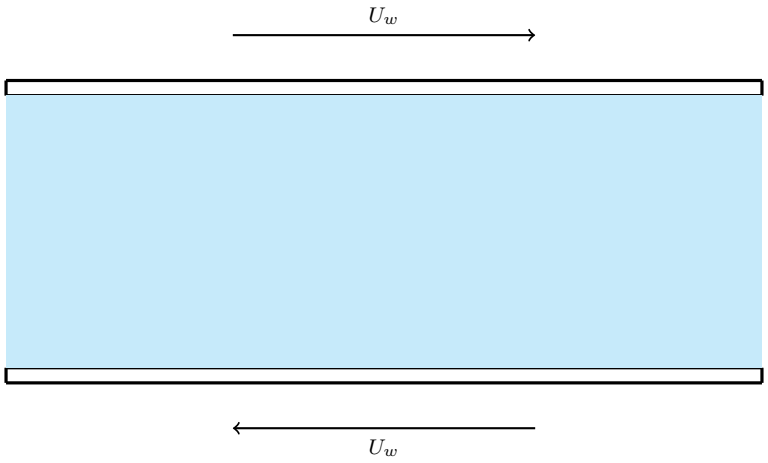

Figure 7.2: Description of the Couette flow problem with the top plate moving at velocity U_w, and the bottom plate moving at velocity $-U_w$.

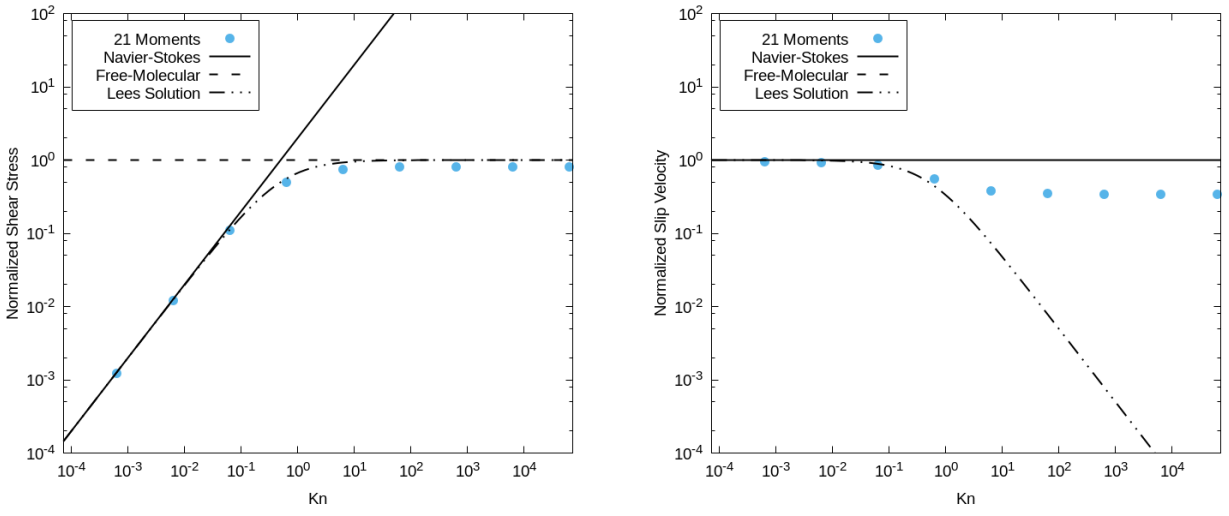

(a) Normalized shear stress

(b) Normalized slip velocity

Figure 7.3: Normalized shear stress and normalized slip velocity at different Knudsen number for the Navier-Stokes, 21-Moment, free-molecular and Lees' solution for a Couette flow.

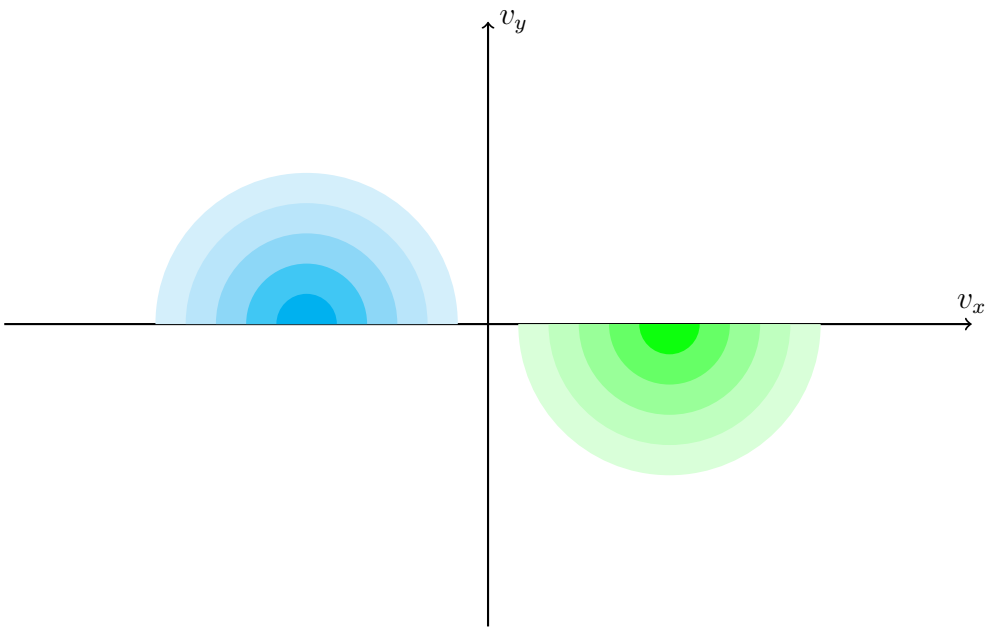

Figure 7.4: Distribution function for the Couette flow in the free-molecular regime.

7.2 Deficiency of the Knudsen Layer Solid-Wall Boundary Condition Method

The treatment of solid-wall boundary conditions through the assumption of a Knudsen layer presents a deficiency for higher Knudsen numbers, where they are inaccurate. To better illustrate the problem, it is easier to go back to the Couette flow problem and use it as an example. In the free-molecular regime, the Couette flow problem shown in Figure 7.2 has a uniform state everywhere between the two plates. The distribution function in this regime is shown in Figure 7.4 and can be described by two half-Maxwellian, where all particles with a positive velocity in the y direction have the distribution function of particles emitted from the bottom plate and all particles with a negative y-direction velocity have the distribution of particles emitted from the top plate. The two half-Maxwellian are centered at $\pm U_{wall}$ and have the same temperature.

The discrepancy between the free-molecular solution and the solution obtained with the 21-moment model in Figure 7.3 was previously mentioned to be, in part, due to some weakness in the approximation for the solid-wall boundary condition. To further investigate this discrepancy, it can be useful to compute the solution for the 10-moment model, since an approximation is not necessary for this associated distribution function. Since the distribution

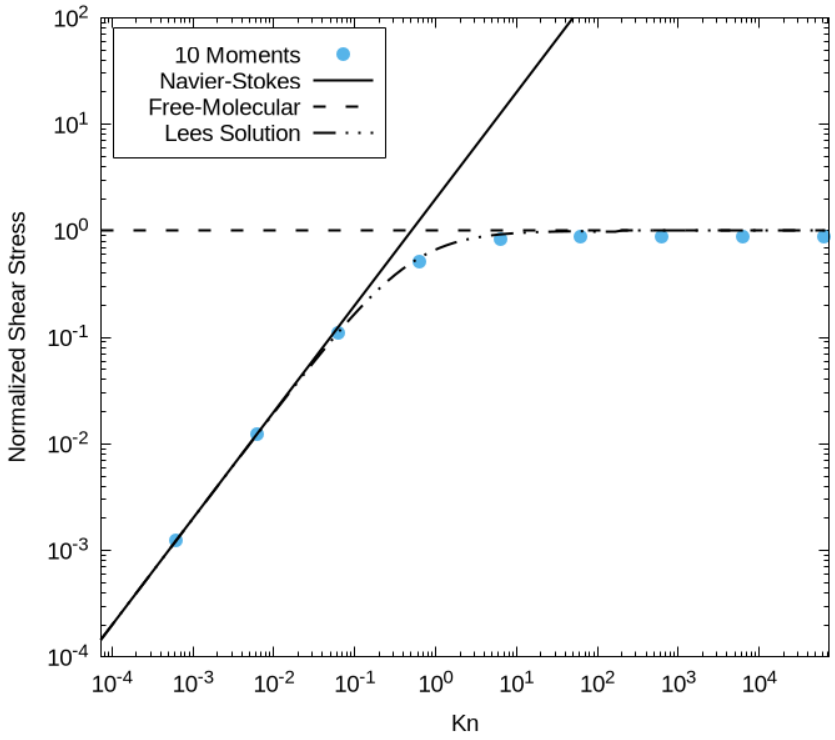

Figure 7.5: Normalized shear stress for the 10-moment model

function associated with this model is an exponential of a second order polynomial, it is possible to integrate it analytically in closed form. The Couette flow solution for the 10-moment model is shown in Figure 7.5. Although no approximation is done to calculate the fluxes at the solid-wall boundaries, there is still a discrepancy in the free-molecular regime between the exact solution and the one obtained with the 10-moment model. When using the Gaussian distribution to approximate the two half-Maxwellian distribution shown in Figure 7.4, it is possible to find a distribution that satisfies not only the macroscopic moments of interest but also the fluxes associated with the two half-Maxwellian. The form of this distribution function is shown in Figure 7.6.

The issue arises when looking at the boundary fluxes. Note that, in the steady-state regime, the value of flux inside the flow must be equal to the boundary fluxes. While the fluxes of the full Gaussian distribution match the ones of the two half-Maxwellian, the boundary fluxes composed of one half-Maxwellian and one half-Gaussian distribution, shown in Figure 7.7, does not match the boundary fluxes for the two half-Maxwellian or the intercells fluxes. In other words, the fluxes associated with the half-Gaussian are not the same as the fluxes of the half-Maxwellian. This translates into an incorrect flux at the boundary and affects the steady-state solution obtained resulting in the obtained discrepancy.

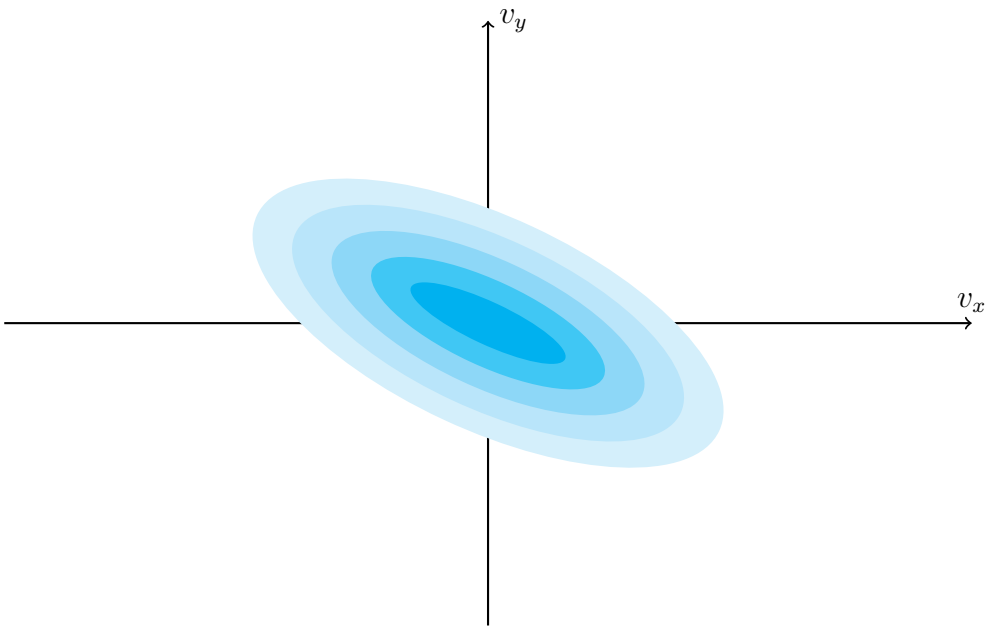

Figure 7.6: Gaussian distribution in agreement with the two half-Maxwellian moments.

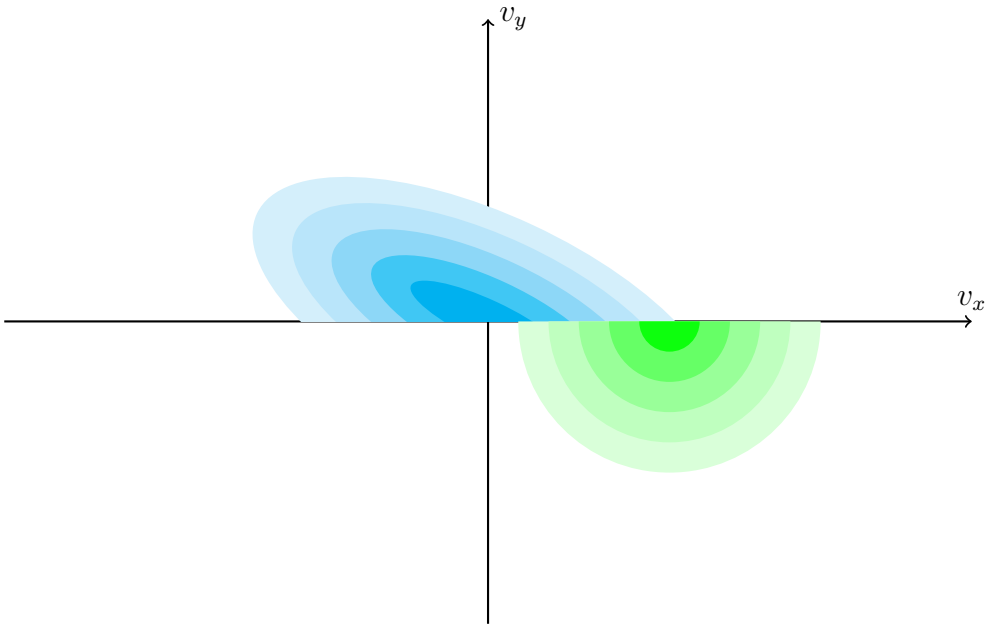

Figure 7.7: Half-Gaussian and half-Maxwellian distribution at the top wall.

Although some deficiency is shown for this treatment of the boundary condition, its effect on the overall solution is minimum. For the purpose of this work, the Knudsen layer approximation is used to treat the boundary condition.

Chapter 8

Numerical Results

To assess the performance and accuracy of the proposed model, some numerical cases are run. The first case shown is a one-dimensional Mach 8 shock where the results are compared with solutions from the Navier-Stokes equations, the 14-moment equations as well as the direct solution of the BGK equation using a discrete-velocity method. This case demonstrates a certain robustness of the model. Furthermore, a Sod shock tube case is run in the continuum and rarefied regimes. The results are compared against the one obtained from directly solving the BGK equation using a discrete-velocity method. Finally, a case of a lid-driven cavity flow is computed for two different Knudsen numbers. At higher Knudsen number, non-equilibrium effect are hoped to be recovered. The results are compared against the solutions obtained for the 14-moment equations and DSMC calculations.

8.1 Stationary Shock

As a preliminary study, to test the robustness and accuracy of the newly developed approximate model, a one-dimensional shock calculation is performed. A stationary shock wave with an incoming Mach number of 8 is simulated using a standard Godunov-type first-order finite-volume solver. The upstream density and pressure are 1.225 kg/m^3 and 101325 Pa respectively and the flow is in local equilibrium. In one-dimension the semi-discrete form

of the finite-volume scheme is expressed as

$$\frac{\partial U_i}{\partial t} + \frac{F_{i+\frac{1}{2}} - F_{i-\frac{1}{2}}}{L} = S_i \tag{8.1}$$

where the index i indicates the number of the cell and L is the length of the cell. To compute the fluxes at each edge, the Harten-Lax-van Leer (HLL) flux function [19] is used,

$$F_{HLL} = \begin{cases} F_L, & \text{if } \lambda_L \geq 0 \\ \frac{\lambda_R F_L - \lambda_L F_R + \lambda_R \lambda_L (U_R - U_L)}{\lambda_R - \lambda_L}, & \text{if } \lambda_L \leq 0 \leq \lambda_R \\ F_R, & \text{if } \lambda_R \leq 0 \end{cases}, \tag{8.2}$$

where λ_L is the wave with the most negative velocity out of both states and λ_R is the wave with the most positive velocity. The solution is advanced in time using explicit-Euler time marching for the fluxes, while the stiff source term is treated implicitly,

$$U_i^{n+1} = U_i^n + \Delta t \left(\frac{F_{i+\frac{1}{2}} - F_{i-\frac{1}{2}}}{L} \right)^n + S_i^{n+1}, \tag{8.3}$$

where n denotes the time step at which the term is evaluated. Treating the source term implicitly allows for a larger time-step to be taken. The flux Jacobian is computed using algorithmic differentiation, the eigenvalues of the flux Jacobian are then computed numerically and are therefore not approximated. The derivatives of each entry of the solution vector with respect to the solution vector are known. Since the closing fluxes are only functions of the solution vector, their derivatives with respect to the solution vector can be tracked as they are being computed. This process is known as algorithmic differentiation. The derivatives of all elements of the solution and flux vector are known and can be used to determine the eigenvalues of the flux Jacobian.

The results obtained are compared to those obtained from a simple first-order discrete-velocity scheme solving the BGK equation [33]. This allows one to validate the degree to which the proposed model is a good approximation to the BGK equation. The fluxes for the BGK solver are chosen using the upwinding flux. The time evolution is done using explicit-Euler while the source term is again treated implicitly. For the discrete-velocity scheme, 400 cells are used in physical space while 100 cells per dimension are used in velocity space. For the 21-moment solver, 2000 cells in physical space are used for the simulation. In both cases, the simulation is run until it reaches steady state. Figures 8.1a, 8.1b, 8.1c, and 8.1d show the density, the pressures, the heat transfer, and the temperatures across a shock with a Mach

number of 8. Although some overshoots are present in the prediction of some of the flows properties, it does show good agreement with the results obtained from solving the BGK equation directly. More importantly, when observing the temperature and pressure profile across the shock, the jump in the x component occurs before the one in the y component. That is because the pressure and temperature in the direction of the shock are excited first, the pressure and temperature in the other direction are excited later through collisions. This effect is invisible to traditional fluid-mechanics models. In a similar manner, the x-direction heat flux of x-direction energy is larger and occurs earlier than the y-direction heat flux of x-direction energy. That behaviour is well recovered by the twenty-one moment model. Figures 8.2a, 8.2b, 8.2c, and 8.2d show the density, the pressures, the heat transfer and the temperatures across a shock of mach number 8, comparing the BGK equation, the fourteen-moment approximation, the Navier-Stokes equations and the twenty-one-moment approximation. It is clear that the twenty-one-moment model matches more closely the results obtained with the BGK equation. To evaluate the hyperbolicity of the model, the largest imaginary part of the eigenvalues normalized by the real part is plotted in Figure 8.2a. As it can be seen, the model only present non-hyperbolicity on a small portion of the domain and, for which, the imaginary part is relatively small compared to the real part.

8.2 The Discontinuous-Galerkin Hancock Method

For the multi-dimensional cases a Discontinuous-Galerkin Hancock Method is used instead of a typical finite-volume scheme. The Discontinuous-Galerkin Hancock scheme (DGH), originally proposed by Suzuki and Van Leer [40], is a coupled space-time method ideal for solving hyperbolic balance law with a stiff source term. It also proves to be advantageous for parallel implementation as a consequence of the low amount of communication required between neighbour cells. This scheme also offers third order accuracy in both space and time. The following section describes the numerical scheme, a more detailed explanation as well as an assessment of its performance and accuracy has been done by Kaufmann [25].

Hyperbolic-relaxation balance laws generally have the form,

$$\frac{\partial \boldsymbol{U}}{\partial t} + \frac{\partial \boldsymbol{F}_i}{\partial x_i} = \boldsymbol{S}\,. \tag{8.4}$$

A solution is sought such that the product of the PDE with the chosen set of test functions,

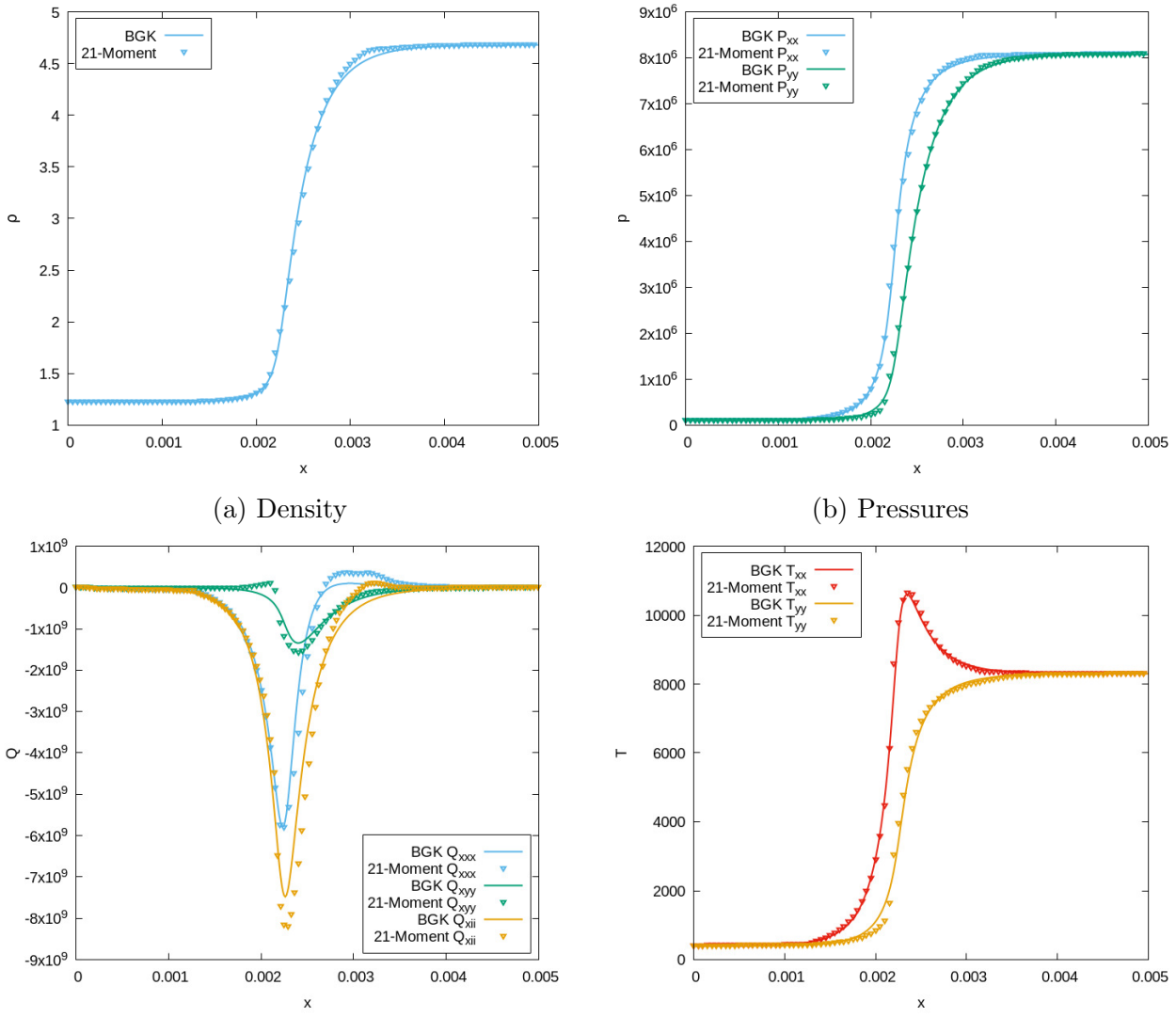

(a) Density

(b) Pressures

(c) Heat transfer

(d) Temperature

Figure 8.1: Mach 8 shock with the BGK equation and the 21-moment approximation.

integrated over the space-time domain, is satisfied. By doing so, the hyperbolic-relaxation set of PDEs can be written as,

$$\iint\limits_{\Omega(t)\times T} \nu(x_j,t)\frac{\partial \boldsymbol{U}}{\partial t}dx_j dt = -\iint\limits_{\Omega(t)\times T} \nu(x_j,t)\frac{\partial \boldsymbol{F}_i}{\partial x_i}dx_j dt + \iint\limits_{\Omega(t)\times T} \nu(x_j,t)\boldsymbol{S}dx_j dt\,, \tag{8.5}$$

where $\Omega(t)\times T$ denotes the space-time domain with a time interval over $[t^n, t^{n+1}]$ and where $\nu(x_j,t)$ is the arbitrary test function. Since the test function is chosen to only be non-zero in one cell, the space domain, $\Omega(t)$, can be reduced to the one of only that cell, $\Omega_k(t)$. By

using integration by part, some terms in Eq. (8.5) can be expressed as,

$$\int_T \nu(x_j,t)\frac{\partial \boldsymbol{U}}{\partial t}dt = \left[\boldsymbol{U}^{n+1}\nu(x_j,t) - \boldsymbol{U}^{n}\nu(x_j,t)\right] - \int_T \boldsymbol{U}\frac{\partial}{\partial t}\nu(x_j,t)dt\,, \tag{8.6}$$

$$\int_{\Omega_k(t)} \nu(x_j,t)\frac{\partial \boldsymbol{F}_i}{\partial x_i}dx_j = \int_{\Gamma_k(t)} \nu(x_j,t)\boldsymbol{F}_i\cdot\hat{n}_i d\Gamma - \int_{\Omega_k(t)} \boldsymbol{F}_i\frac{\partial}{\partial x_i}\nu(x_j,t)dx_j\,, \tag{8.7}$$

where Γ_k is the boundary of the cell and where $\hat{n}_i$ is the outward pointing unit normal on the boundary. By assuming that the spatial domain is fixed in time and that the test functions are only a function of space further simplifications can be made. By substituting Eqs. (8.6) and (8.7) into Eq. (8.5) and using the Fubini theorem allowing a change in the order of integration the following is obtained,

$$\begin{aligned}\int_{\Omega_k} \nu(x_j)\left[\boldsymbol{U}^{n+1} - \boldsymbol{U}^{n}\right]dx_j = &-\iint_{\Gamma_k\times T} \nu(x_j)\boldsymbol{F}_i\cdot\hat{n}_i d\Gamma dt + \iint_{\Omega_k\times T} \boldsymbol{F}_i\frac{\partial}{\partial x_i}\nu(x_j)dx_j dt \\ &+ \iint_{\Omega_k\times T} \nu(x_j)\boldsymbol{S}dx_j dt\,.\end{aligned} \tag{8.8}$$

For the DGH scheme, the chosen set of test functions is of linear nature,

$$\nu(x_j) = [1, x-x_c, y-y_c, z-z_c]\,, \tag{8.9}$$

where x_c, y_c, z_c are the centroid of the cell. The solution in a cell can be written as a function of the average solution, $\overline{\boldsymbol{U}}_k$, the average solution gradient, $(\overline{\Delta_i \boldsymbol{U}})_k$, and the test functions,

$$\boldsymbol{U}_k = \overline{\boldsymbol{U}}_k + (\overline{\Delta_x \boldsymbol{U}})_k(x-x_{c_k}) + (\overline{\Delta_y \boldsymbol{U}})_k(y-y_{c_k}) + (\overline{\Delta_z \boldsymbol{U}})_k(z-z_{c_k})\,, \tag{8.10}$$

where $\overline{\boldsymbol{U}}_k$, $(\overline{\Delta_x \boldsymbol{U}})_k$, $(\overline{\Delta_y \boldsymbol{U}})_k$ and $(\overline{\Delta_z \boldsymbol{U}})_k$ are called the degrees of freedom. By substituting Eq. (8.10) into Eq. (8.8), and by integrating with each test function, a formula for the update of the degrees of freedom is obtained,

$$\overline{\boldsymbol{U}}_k^{n+1} = \overline{\boldsymbol{U}}_k^{n} - \frac{1}{V_k}\iint_{\Gamma_k\times T} \boldsymbol{F}_i\cdot\hat{n}_i d\Gamma dt + \frac{1}{V_k}\iint_{\Omega_k\times T} \boldsymbol{S}dx_j dt\,, \tag{8.11}$$

$$\begin{bmatrix} (\overline{\Delta_x \boldsymbol{U}})_k^{n+1} \\ (\overline{\Delta_y \boldsymbol{U}})_k^{n+1} \\ (\overline{\Delta_z \boldsymbol{U}})_k^{n+1} \end{bmatrix} = \begin{bmatrix} (\overline{\Delta_x \boldsymbol{U}})_k^{n} \\ (\overline{\Delta_y \boldsymbol{U}})_k^{n} \\ (\overline{\Delta_z \boldsymbol{U}})_k^{n} \end{bmatrix} + \boldsymbol{K}_k \Bigg(- \iint\limits_{\Gamma_k \times T} \begin{bmatrix} x - x_{c_k} \\ y - y_{c_k} \\ z - z_{c_k} \end{bmatrix} \boldsymbol{F}_i \cdot \hat{n}_i d\Gamma dt + \iint\limits_{\Omega_k \times T} \begin{bmatrix} \boldsymbol{F}_x \\ \boldsymbol{F}_y \\ \boldsymbol{F}_z \end{bmatrix} dx_j dt + \iint\limits_{\Omega_k \times T} \begin{bmatrix} x - x_{c_k} \\ y - y_{c_k} \\ z - z_{c_k} \end{bmatrix} \boldsymbol{S} dx_j dt \Bigg) , \tag{8.12}$$

where V_k is the volume of the cell and $\boldsymbol{K}_k$ is the inverse matrix of the cell's area moment of inertia,

$$\boldsymbol{K}_k = \begin{bmatrix} I_{xx} & I_{xy} & I_{xz} \\ I_{xy} & I_{yy} & I_{yz} \\ I_{xz} & I_{yz} & I_{zz} \end{bmatrix}^{-1} . \tag{8.13}$$

To perform an update of the degrees of freedom, some numerical approximations are needed for the evaluation of the interface flux, the surface and volume integral of the flux, the volume integral of the source term and the time integral of the both the flux and the source term.

8.2.1 Interface Flux and Surface Integral

At the interface between two cells, the solution is discontinuous and an approximation is needed to evaluate the fluxes. Flux functions such as the Roe [37] and the HLLE [18] are used for that effect, they serve as an approximate Riemann solver.

To approximate the surface integral of the interface flux in Eq. (8.11), a two-points Gaussian quadrature is used,

$$\iint\limits_{\Gamma_k \times T} \boldsymbol{F}_i \cdot \hat{n}_i d\Gamma dt \approx \int\limits_T \sum_\xi w_\xi \tilde{\boldsymbol{F}}_\xi dt \, , \tag{8.14}$$

where $\tilde{\boldsymbol{F}}_\xi$ is the flux at quadrature point ξ approximated with the flux function and where w_ζ are the associated weights. To integrate in time, the midpoint rule is used as an approx-

imation leading to,

$$\iint\limits_{\Gamma_k \times T} \boldsymbol{F}_i \cdot \hat{n}_i d\Gamma dt \approx \Delta t \sum_{\xi} w_\xi \tilde{\boldsymbol{F}}_\xi^{n+\frac{1}{2}} \,. \tag{8.15}$$

The same quadrature rule and midpoint approximation in time is used to numerically integrate the surface integral in Eq. (8.12),

$$\iint\limits_{\Gamma_k \times T} \begin{bmatrix} x - x_{c_k} \\ y - y_{c_k} \\ z - z_{c_k} \end{bmatrix} \boldsymbol{F}_i \cdot \hat{n}_i d\Gamma dt \approx \Delta t \begin{bmatrix} \sum\limits_{\xi} w_\xi (x_\xi - x_{c_k}) \tilde{\boldsymbol{F}}_\xi^{n+\frac{1}{2}} \\ \sum\limits_{\xi} w_\xi (y_\xi - y_{c_k}) \tilde{\boldsymbol{F}}_\xi^{n+\frac{1}{2}} \\ \sum\limits_{\xi} w_\xi (z_\xi - z_{c_k}) \tilde{\boldsymbol{F}}_\xi^{n+\frac{1}{2}} \end{bmatrix} . \tag{8.16}$$

The fluxes $\tilde{\boldsymbol{F}}_\xi^{n+\frac{1}{2}}$ are evaluated at time $t^{n+\frac{1}{2}}$. In order to approximate the value at a half time step, a Hancock predictor step is taken. This technique is explained in more details one of the coming section.

8.2.2 The Hancock Predictor Step

To approximate the solution at fractional timesteps, the Hancock predictor step is used. The equation is essentially the same as Eq. (8.11) but without the consideration of interface quadratures,

$$\overline{\boldsymbol{U}}_k^{n+\psi} = \overline{\boldsymbol{U}}_k^n - \frac{1}{V_k} \iint\limits_{\Gamma_k \times T'} \hat{\boldsymbol{F}}_i \cdot \hat{n}_i d\Gamma dt + \frac{1}{V_k} \iint\limits_{\Omega_k \times T'} \boldsymbol{S} dx_j dt \,, \tag{8.17}$$

where $\hat{\boldsymbol{F}}_i$ is the flux vector evaluated using only quadratures and solution within the element. The time interval, T', is over $[t^n, t^\psi]$ where ψ is either $\frac{1}{2}$ or $\frac{1}{6}$. To further simplify, the fluxes are treated explicitly in time while the source is treated implicitly,

$$\overline{\boldsymbol{U}}_k^{n+\psi} = \overline{\boldsymbol{U}}_k^n - \frac{\psi \Delta t}{V_k} \left[\int\limits_{\Gamma_k} \hat{\boldsymbol{F}}_i^n \cdot \hat{n}_i d\Gamma + \int\limits_{\Omega_k} \boldsymbol{S}^{n+\psi} dx_j \right] . \tag{8.18}$$

The volume integral of the source term in Eq. (8.18) is approximated by a single quadrature point at the cell centroid while the surface integral of the fluxes is approximated by using a two-points Gaussian quadrature rule. Once the cell-average is updated at a fractional timestep, the solution at any location in the volume can be obtained by extrapolating from

the average using the slopes at time t^n,

$$\boldsymbol{U}_k^{n+\psi} = \overline{\boldsymbol{U}}_k^{n+\psi} + \phi_k^n \begin{bmatrix} (\overline{\Delta_x \boldsymbol{U}})_k^n & (\overline{\Delta_y \boldsymbol{U}})_k^n & (\overline{\Delta_z \boldsymbol{U}})_k^n \end{bmatrix} \begin{bmatrix} x - x_{c_k} \\ y - y_{c_k} \\ z - z_{c_k} \end{bmatrix}, \tag{8.19}$$

where ϕ_k^n is a slope limiter used to prevent the introduction of new extremas.

8.2.3 Volume Integral of Flux and Source Term

In the cell average and slope update, Eqs. (8.11) and (8.12), there are three volume and time integrals. Two of them for the source term and one for the fluxes. Due to the stiffness of the source term, the Radau IIA method is used for time integration. This method is a third order implicit time-marching scheme that has a general form,

$$\begin{aligned} y^{n+\frac{1}{3}} &= y^n + \Delta t \left[\frac{5}{12} \left(\frac{dy}{dt} \right)^{n+\frac{1}{3}} - \frac{1}{12} \left(\frac{dy}{dt} \right)^{n+1} \right], \\ y^{n+1} &= y^n + \Delta t \left[\frac{3}{4} \left(\frac{dy}{dt} \right)^{n+\frac{1}{3}} + \frac{1}{4} \left(\frac{dy}{dt} \right)^{n+1} \right]. \end{aligned} \tag{8.20}$$

This adds the requirement for the state at timestep $t^{n+\frac{1}{3}}$.

The volume integral of the flux, is approximated using an eight-point Gaussian quadrature in space. For the integration in time, A Radau IIA two-point quadrature is used. The volume integral of the source term is approximated by a single point quadrature in space and by, again, a Radau IIA approximation in time. Finally, the volume integral of the moment of the source term is treated the same way as the one for the source term. A single point quadrature is used to approximate the integration in space while the Radau IIA method is used to approximate the integration in time.

8.2.4 Discrete Update Formula

By inserting all chosen space-time integration approximations into Eqs. (8.11) and (8.12), two discrete update formulas are obtained. For the cell average update,

$$\begin{bmatrix} \overline{\boldsymbol{U}}_k^{n+\frac{1}{3}} \\ \overline{\boldsymbol{U}}_k^{n+1} \end{bmatrix} = \begin{bmatrix} \overline{\boldsymbol{U}}_k^{n} \\ \overline{\boldsymbol{U}}_k^{n} \end{bmatrix} - \frac{\Delta t}{V_k} \begin{bmatrix} \frac{1}{3} \sum\limits_{\xi} w_\xi \tilde{\boldsymbol{F}}^{n+\frac{1}{6}} \\ \sum\limits_{\xi} w_\xi \tilde{\boldsymbol{F}}^{n+\frac{1}{2}} \end{bmatrix} + \Delta t \begin{bmatrix} \frac{5}{12}\boldsymbol{I} & -\frac{1}{12}\boldsymbol{I} \\ \frac{3}{4}\boldsymbol{I} & \frac{1}{4}\boldsymbol{I} \end{bmatrix} \begin{bmatrix} \overline{\boldsymbol{S}}^{n+\frac{1}{3}} \\ \overline{\boldsymbol{S}}^{n+1} \end{bmatrix}, \tag{8.21}$$

where $\boldsymbol{I}$ is the identity matrix. For the slope update, the obtained discrete update formula takes the form of,

$$\begin{bmatrix} (\overline{\Delta_x \boldsymbol{U}})_k^{n+\frac{1}{3}} \\ (\overline{\Delta_y \boldsymbol{U}})_k^{n+\frac{1}{3}} \\ (\overline{\Delta_z \boldsymbol{U}})_k^{n+\frac{1}{3}} \\ (\overline{\Delta_x \boldsymbol{U}})_k^{n+1} \\ (\overline{\Delta_y \boldsymbol{U}})_k^{n+1} \\ (\overline{\Delta_z \boldsymbol{U}})_k^{n+1} \end{bmatrix} = \begin{bmatrix} (\overline{\Delta_x \boldsymbol{U}})_k^{n} \\ (\overline{\Delta_y \boldsymbol{U}})_k^{n} \\ (\overline{\Delta_z \boldsymbol{U}})_k^{n} \\ (\overline{\Delta_x \boldsymbol{U}})_k^{n} \\ (\overline{\Delta_y \boldsymbol{U}})_k^{n} \\ (\overline{\Delta_z \boldsymbol{U}})_k^{n} \end{bmatrix} + \Delta t \boldsymbol{\Upsilon} \begin{bmatrix} \frac{1}{3} \sum\limits_{\xi} w_\xi (x_\xi - x_{c_k}) \tilde{\boldsymbol{F}}_\xi^{n+\frac{1}{6}} \\ \frac{1}{3} \sum\limits_{\xi} w_\xi (y_\xi - y_{c_k}) \tilde{\boldsymbol{F}}_\xi^{n+\frac{1}{6}} \\ \frac{1}{3} \sum\limits_{\xi} w_\xi (z_\xi - z_{c_k}) \tilde{\boldsymbol{F}}_\xi^{n+\frac{1}{6}} \\ \sum\limits_{\xi} w_\xi (x_\xi - x_{c_k}) \tilde{\boldsymbol{F}}_\xi^{n+\frac{1}{2}} \\ \sum\limits_{\xi} w_\xi (y_\xi - y_{c_k}) \tilde{\boldsymbol{F}}_\xi^{n+\frac{1}{2}} \\ \sum\limits_{\xi} w_\xi (z_\xi - z_{c_k}) \tilde{\boldsymbol{F}}_\xi^{n+\frac{1}{2}} \end{bmatrix}$$

$$+ \Delta t \boldsymbol{\Upsilon} \begin{bmatrix} \frac{1}{3} \sum\limits_{\chi} w_\chi \left[\frac{1}{2} (\boldsymbol{F}_x)_\chi^{n} + \frac{1}{2} (\boldsymbol{F}_x)_\chi^{n+\frac{1}{3}} \right] \\ \frac{1}{3} \sum\limits_{\chi} w_\chi \left[\frac{1}{2} (\boldsymbol{F}_y)_\chi^{n} + \frac{1}{2} (\boldsymbol{F}_y)_\chi^{n+\frac{1}{3}} \right] \\ \frac{1}{3} \sum\limits_{\chi} w_\chi \left[\frac{1}{2} (\boldsymbol{F}_z)_\chi^{n} + \frac{1}{2} (\boldsymbol{F}_z)_\chi^{n+\frac{1}{3}} \right] \\ \sum\limits_{\chi} w_\chi \left[\frac{3}{4} (\boldsymbol{F}_x)_\chi^{n+\frac{1}{3}} + \frac{1}{4} (\boldsymbol{F}_x)_\chi^{n+1} \right] \\ \sum\limits_{\chi} w_\chi \left[\frac{3}{4} (\boldsymbol{F}_y)_\chi^{n+\frac{1}{3}} + \frac{1}{4} (\boldsymbol{F}_y)_\chi^{n+1} \right] \\ \sum\limits_{\chi} w_\chi \left[\frac{3}{4} (\boldsymbol{F}_z)_\chi^{n+\frac{1}{3}} + \frac{1}{4} (\boldsymbol{F}_z)_\chi^{n+1} \right] \end{bmatrix}$$

$$+\Delta t \begin{bmatrix} \frac{5}{12}\boldsymbol{I} & -\frac{1}{12}\boldsymbol{I} \\ \frac{3}{4}\boldsymbol{I} & \frac{1}{4}\boldsymbol{I} \end{bmatrix} \begin{bmatrix} \frac{\partial \boldsymbol{S}}{\partial \boldsymbol{U}}^{n+\frac{1}{3}} (\overline{\Delta_x \boldsymbol{U}})_k^{n+\frac{1}{3}} \\ \frac{\partial \boldsymbol{S}}{\partial \boldsymbol{U}}^{n+\frac{1}{3}} (\overline{\Delta_y \boldsymbol{U}})_k^{n+\frac{1}{3}} \\ \frac{\partial \boldsymbol{S}}{\partial \boldsymbol{U}}^{n+\frac{1}{3}} (\overline{\Delta_z \boldsymbol{U}})_k^{n+\frac{1}{3}} \\ \frac{\partial \boldsymbol{S}}{\partial \boldsymbol{U}}^{n+1} (\overline{\Delta_x \boldsymbol{U}})_k^{n+1} \\ \frac{\partial \boldsymbol{S}}{\partial \boldsymbol{U}}^{n+1} (\overline{\Delta_y \boldsymbol{U}})_k^{n+1} \\ \frac{\partial \boldsymbol{S}}{\partial \boldsymbol{U}}^{n+1} (\overline{\Delta_z \boldsymbol{U}})_k^{n+1} \end{bmatrix}, \tag{8.22}$$

where, once again, $\boldsymbol{I}$ is the identity matrix and $\boldsymbol{\Upsilon}$ is a block matrix defined as,

$$\boldsymbol{\Upsilon} = \begin{bmatrix} \boldsymbol{K}_k & 0 & 0 \\ 0 & \boldsymbol{K}_k & 0 \\ 0 & 0 & \boldsymbol{K}_k \end{bmatrix}. \tag{8.23}$$

8.3 Sod Shock Tube

The Sod shock-tube problem consist essentially of a Riemann problem in one dimension. A left and right state are set as initial conditions and are time marched to a desired time. The set left state has a density of 4.696 kg/m^3, a velocity 0 m/s and a pressure of 404400 Pa while the right state has a density of 1.408 kg/m^3, a velocity of 0 m/s and a pressure of 101100 Pa. The solution is time marched until a final time of 0.007 s is reached. The domain is 12 m long and the left and right state are discontinuous at the center. The case is run with collision and without collisions by turning off the source term. For the colissionless case, the relaxation time is set to $\tau = 1 \times 10^{100}$ where as for the transition regime and continuum regime the relaxation time is set to $\tau = 1.5 \times 10^4$ and $\tau = 1 \times 10^{-10}$ respectively. A resolution of 500 cells is used to compute the solution for the 21-moment model using the Discontinuous-Galerkin-Hancock method. For the discrete-velocity scheme, 400 cells are used in physical space while 100 cells per dimension are used in velocity space.

In the collision dominated regime, shown in Figures 8.3a, 8.3b, 8.3c and 8.3d, the solutions from the 21-moment model and the BGK equation both recover the Euler solution. That is because the source term is dominating. Both the BGK and the 21-moment solution are in agreement. In the collisionless regime, shown in Figures 8.4a, 8.4b, 8.4c and 8.4d, the BGK solution is expected to be smooth over the domain with no apparent discontinuities. The 21-moment solution is approximating the BGK solution with the presence of discontinuity

associated with its different wavespeeds. This is expected since the 21-moment model is a continuum treatment of the flow. The 21-moment solution still follows the BGK solution relatively closely. In the transition regime, shown in Figures 8.5a, 8.5b, 8.5c and 8.5d, the solution from the 21-moment model is able to predict the same solution as the BGK solution. This supports the accuracy of the proposed model in predicting flow solutions in the transition regime.

8.4 Lid-Driven Cavity Flow

The lid-driven cavity flow, as shown in Figure 8.6 consist of a square domain where all boundaries are solid-walls that are stationary except for the top wall which moves at a velocity of 50 m/s along the x-direction. The initial conditions for the argon gas are atmospheric pressure and ambient temperature of 273 K with a density of 1.78 kg/m^3. The wall temperature is also set to be 273 K. A Cartesian mesh of 150 cells by 150 cells is used for the computational domain. The Knudsen-wall boundary condition from Section 7 is used to model the solid walls. The simulation is run using the third-order Discontinuous-Galerkin-Hancock method.

The results computed with the 21-moment model is compared against the 14-moment model and a DSMC solution by John, Gu, and Emerson [21, 22] for a Knudsen number of 0.1 and 0.05. The BGK collision model is used for the 14 and 21-moment models. The solution for a Knudsen number of 0.05 is shown in Figures 8.7, 8.8 and 8.9 while Figures 8.10, 8.11 and 8.12 show the solution for a Knudsen number of 0.1. For a Knudsen number of 0.05, the Mach number close to the lid is higher in the 14-moment and 21-moment solution than in the DSMC solution. This could be attributed to the treatment of the solid-wall. For the rest of the domain, all three solutions are in close agreement. The same can be said for a Knudsen number of 0.1, where even at the lid the temperature is in better agreement with the DSMC results. The DSMC plots for the temperature with the heat flux contour show a heat flux that goes from the cold gas to the hot gas. This is a non-equilibrium effect that contradicts Fourier's law and therefore cannot be recover using the traditional Navier-Stokes equation. This non-equilibrium effect is recovered by both the 14-moment and 21-moment model for a Knudsen of 0.05 and 0.1. The temperature in the 14-moment and 21-moment solution is higher than the DSMC solution especially near the lid in the case of the 14-moment model. Once again, this is most likely due to the treatment of the solid-wall boundary condition.

Finally, all three model are in fair agreement for the prediction of shear pressure for all Knudsen number.

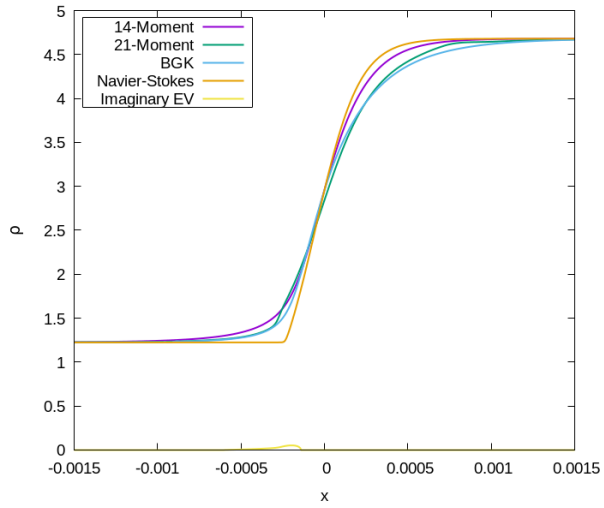

(a) Density and normalized imaginary part of associated eigenvalues

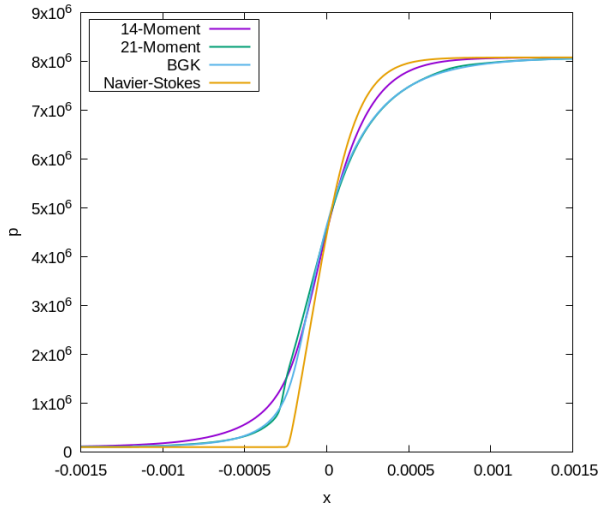

(b) Pressures

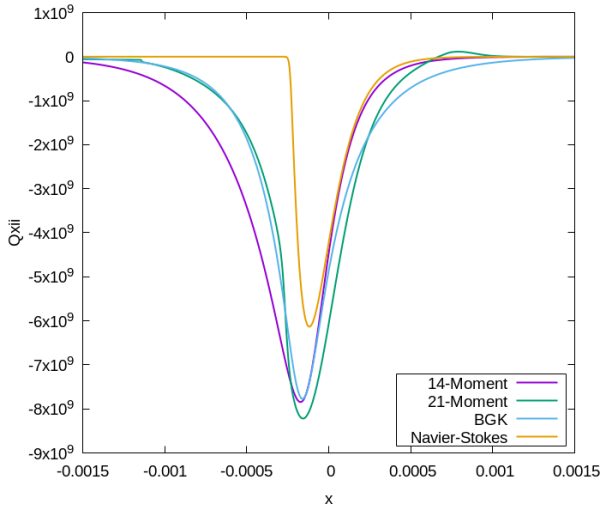

(c) Heat transfer

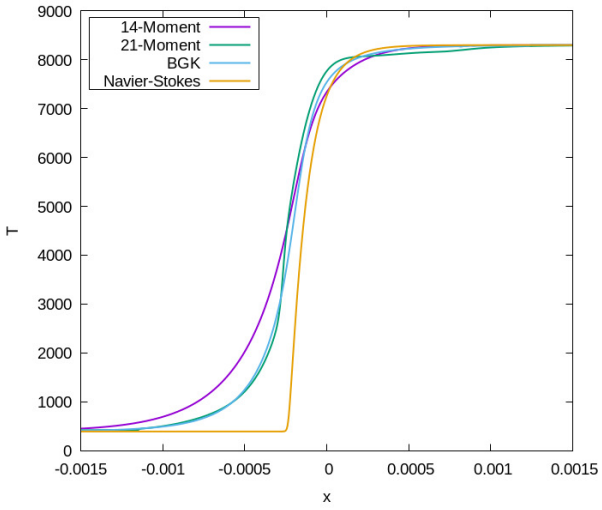

(d) Temperature

Figure 8.2: Mach 8 shock with the BGK equation, the 14-moment approximation, the Navier-Stokes equations and the 21-moment approximation.

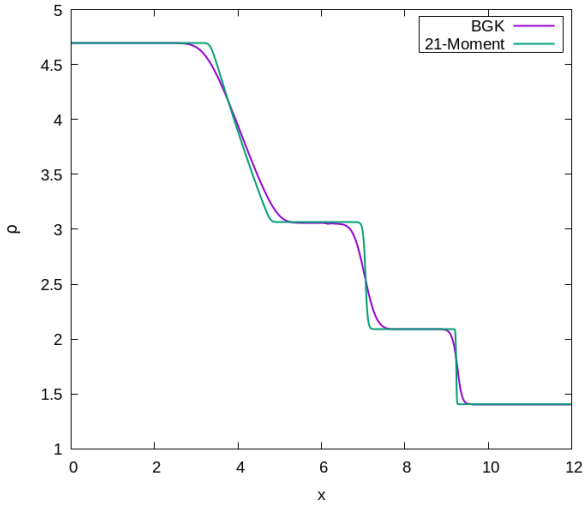

(a) Density

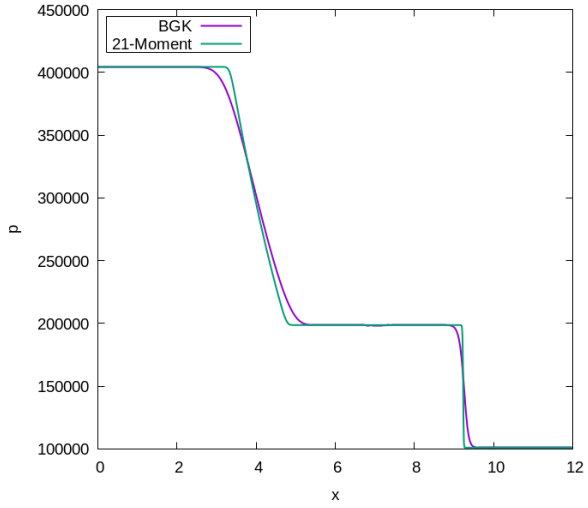

(b) Pressure

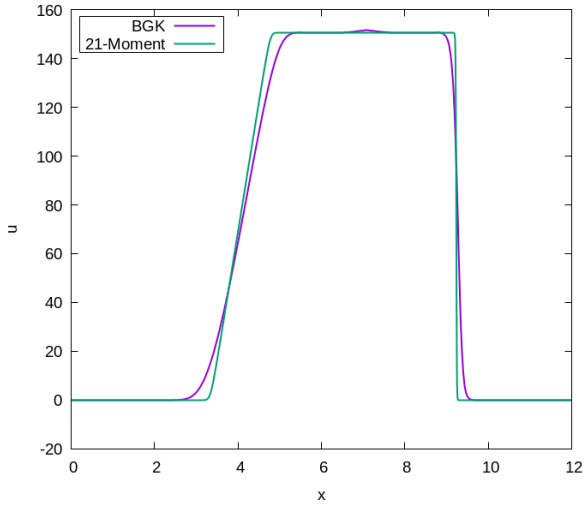

(c) Velocity

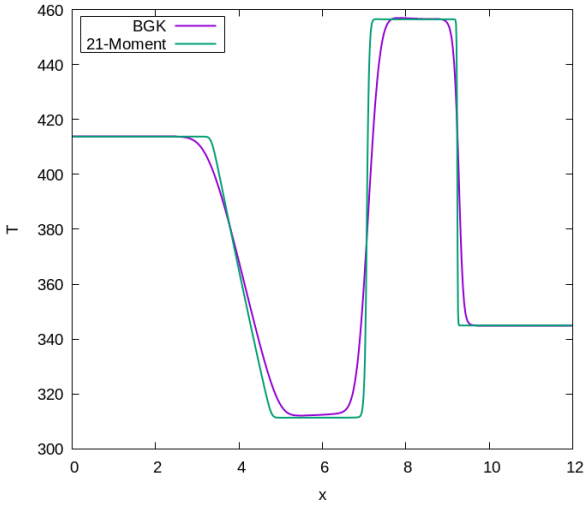

(d) Temperature

Figure 8.3: Sod problem at low Knudsen number with the BGK equation and the 21-moment approximation.

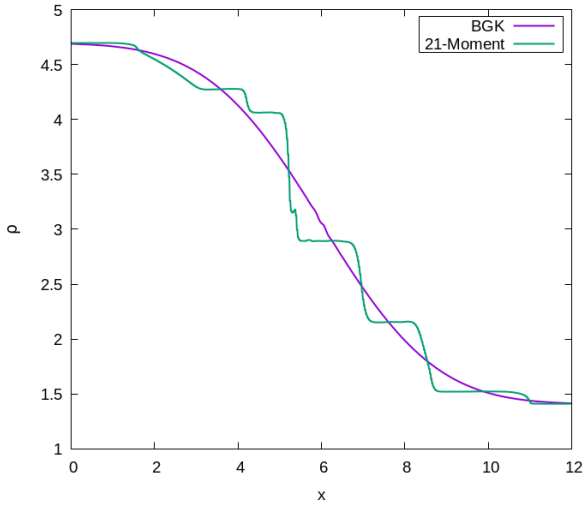

(a) Density

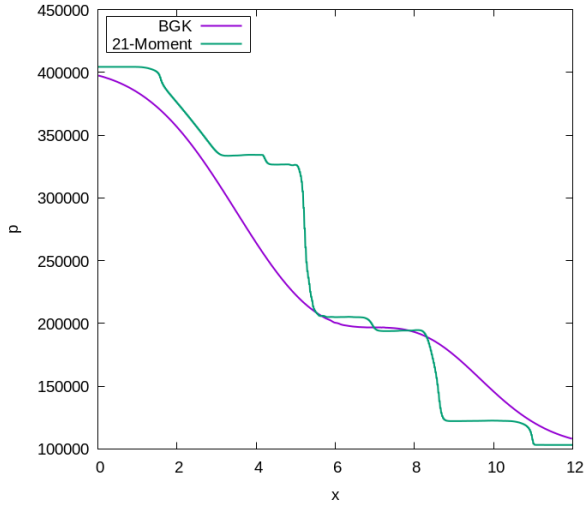

(b) Pressure

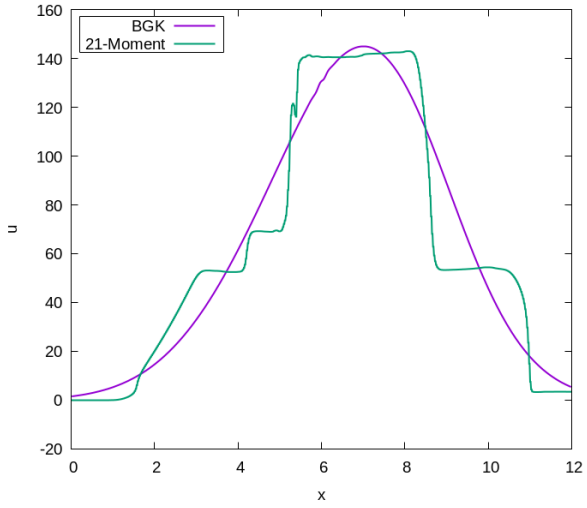

(c) Velocity

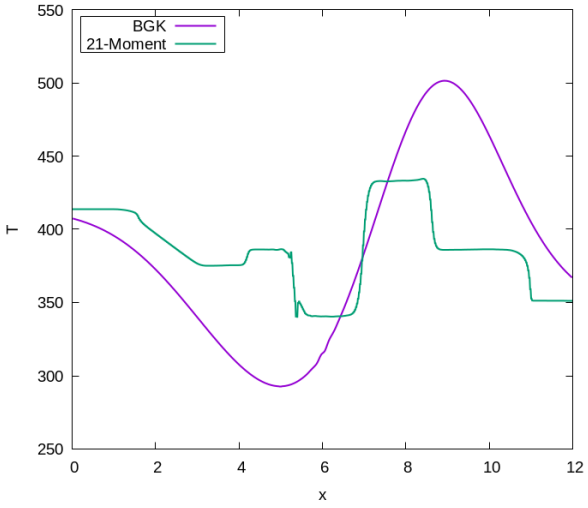

(d) Temperature

Figure 8.4: Sod problem at high Knudsen number with the BGK equation and the 21-moment approximation.

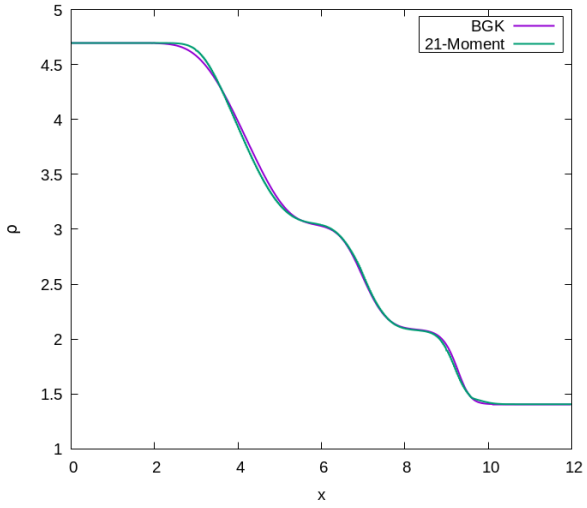

(a) Density

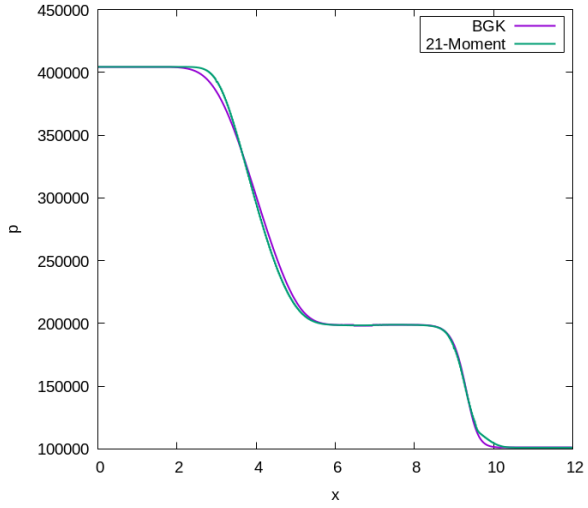

(b) Pressure

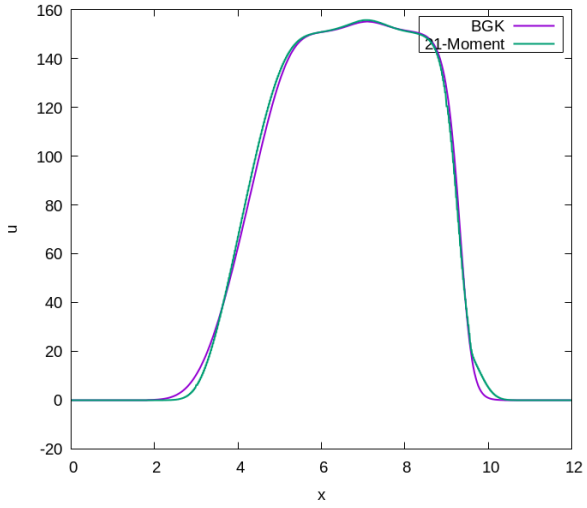

(c) Velocity

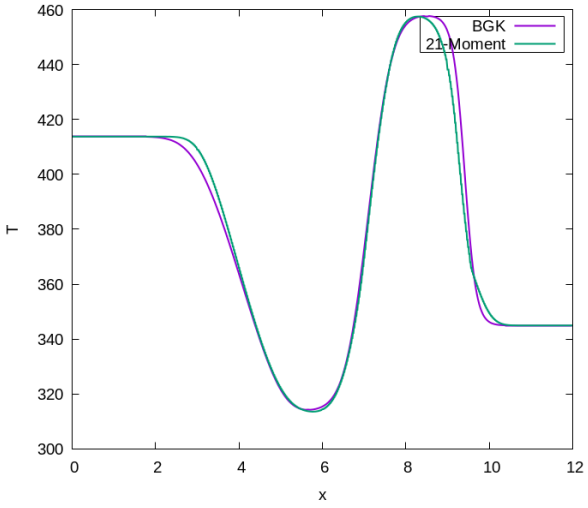

(d) Temperature

Figure 8.5: Sod problem at transition Knudsen number with the BGK equation and the 21-moment approximation.

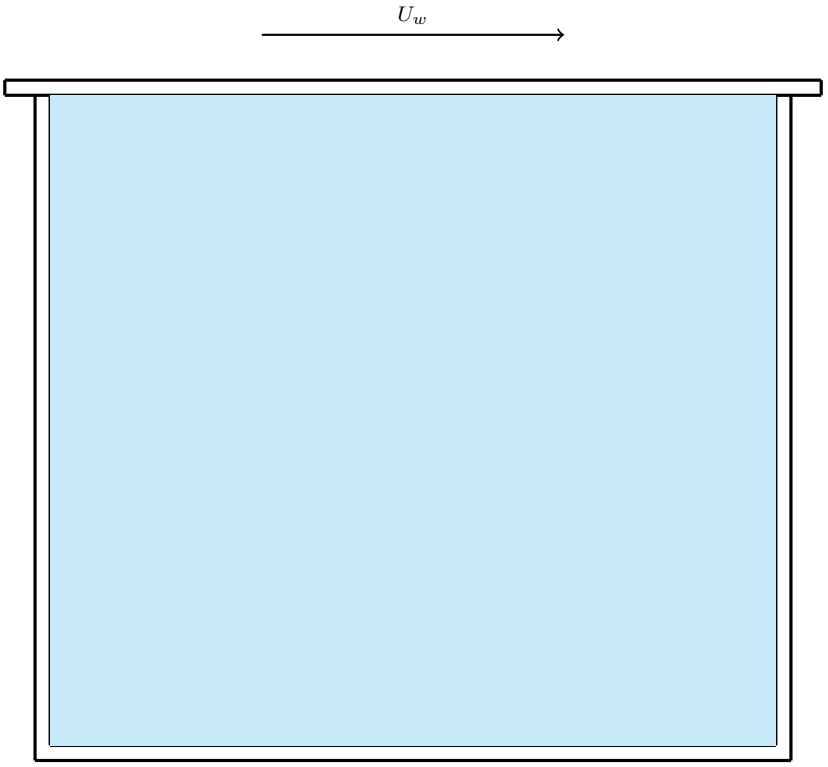

Figure 8.6: Description of the lid-driven cavity problem with the top wall moving at velocity U_w.

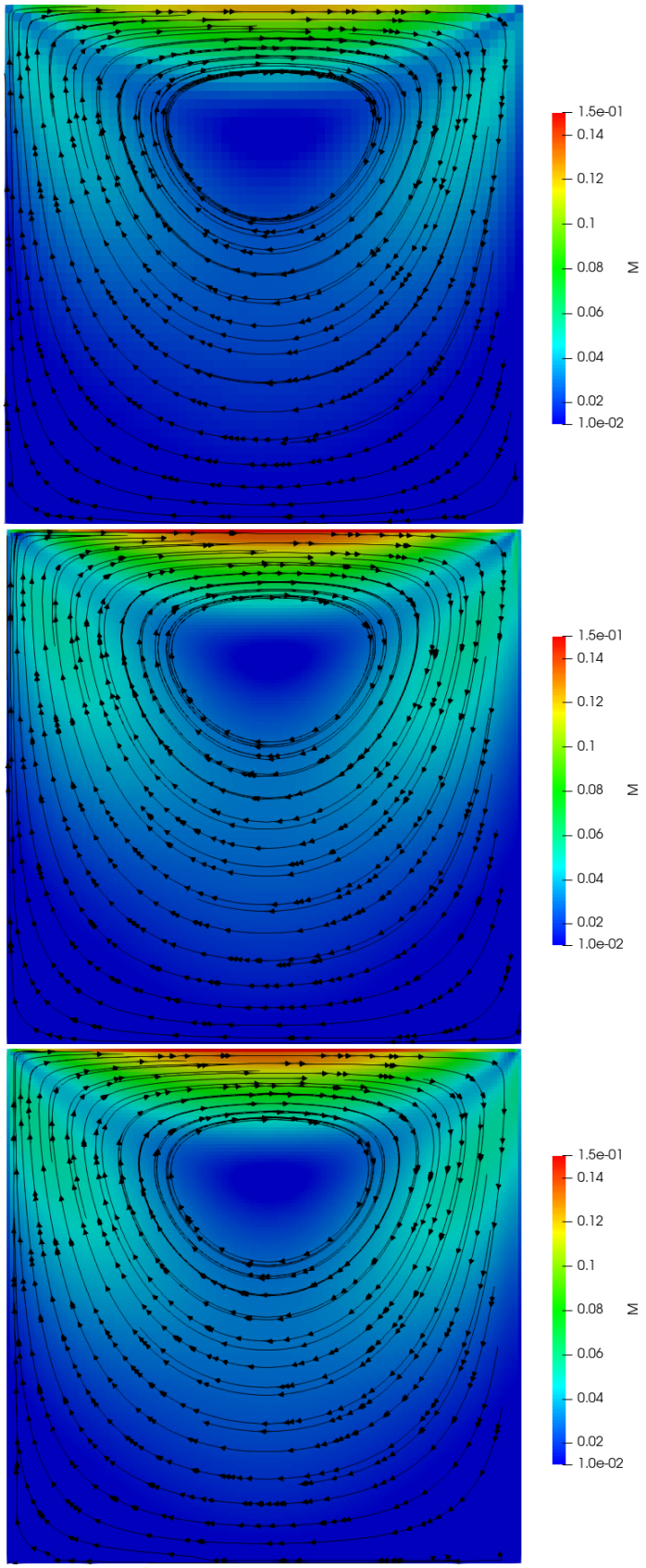

Figure 8.7: Mach number contour for the lid-driven cavity flow at $Kn = 0.05$ for DSMC (top), 14-moment closure (middle) and 21-moment closure (bottom).

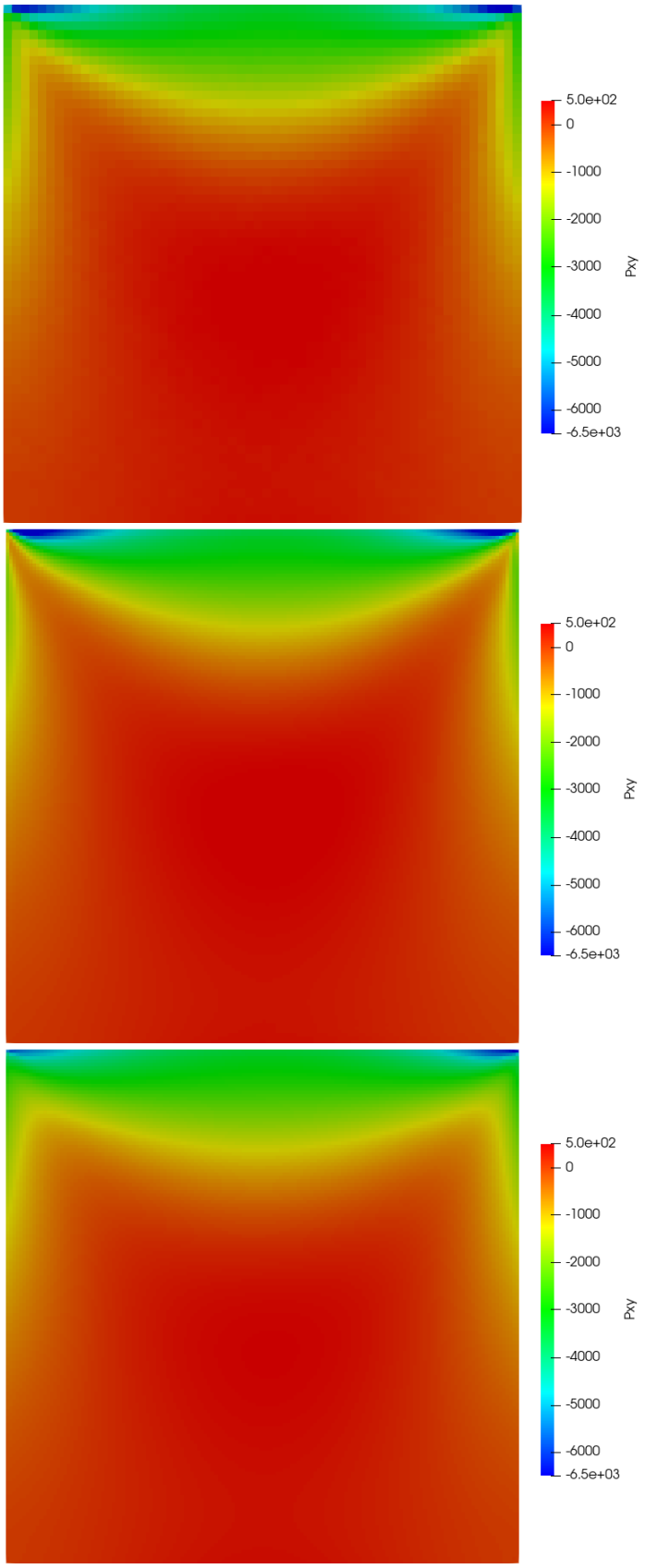

Figure 8.8: P_{xy} contour for the lid-driven cavity flow at $Kn = 0.05$ for DSMC (top), 14-moment closure (middle) and 21-moment closure (bottom).

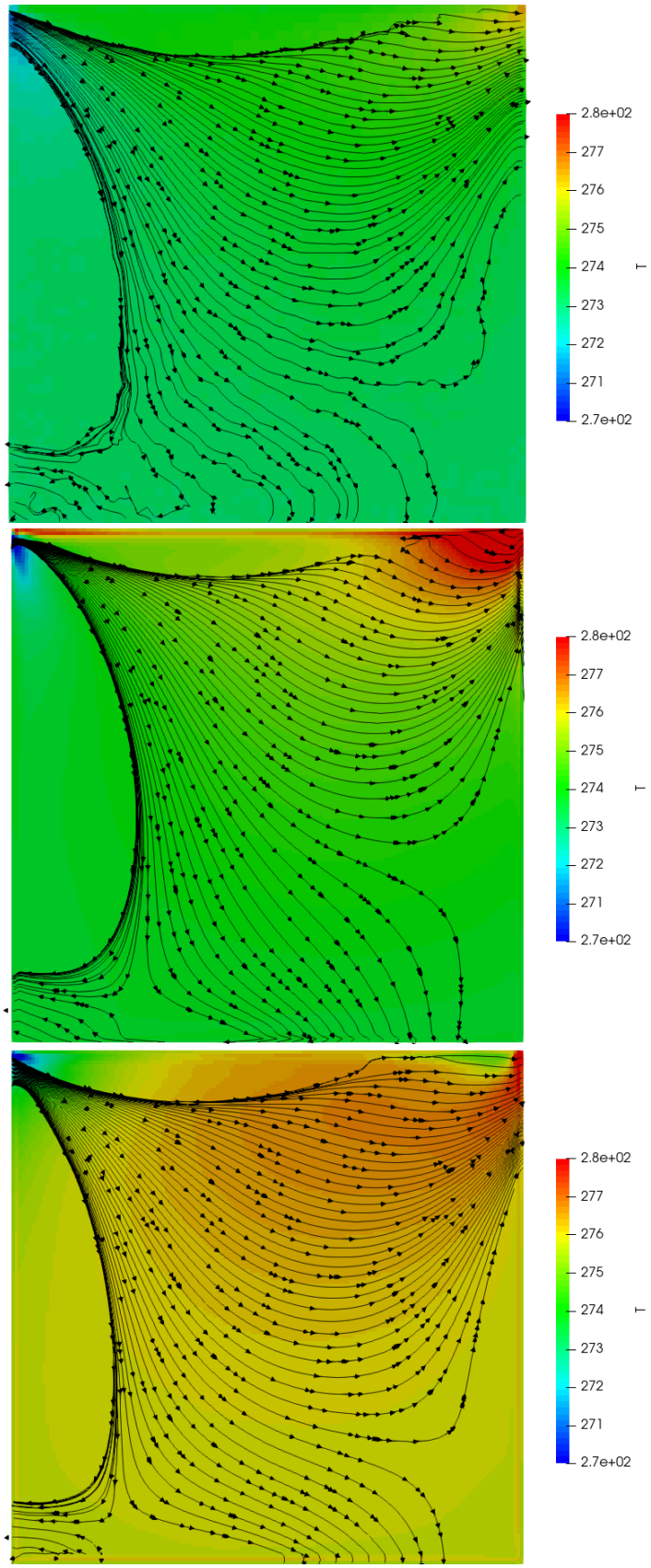

Figure 8.9: Temperature contour with heat-transfer streamline for the lid-driven cavity flow at $Kn = 0.05$ for DSMC (top), 14-moment closure (middle) and 21-moment closure (bottom).

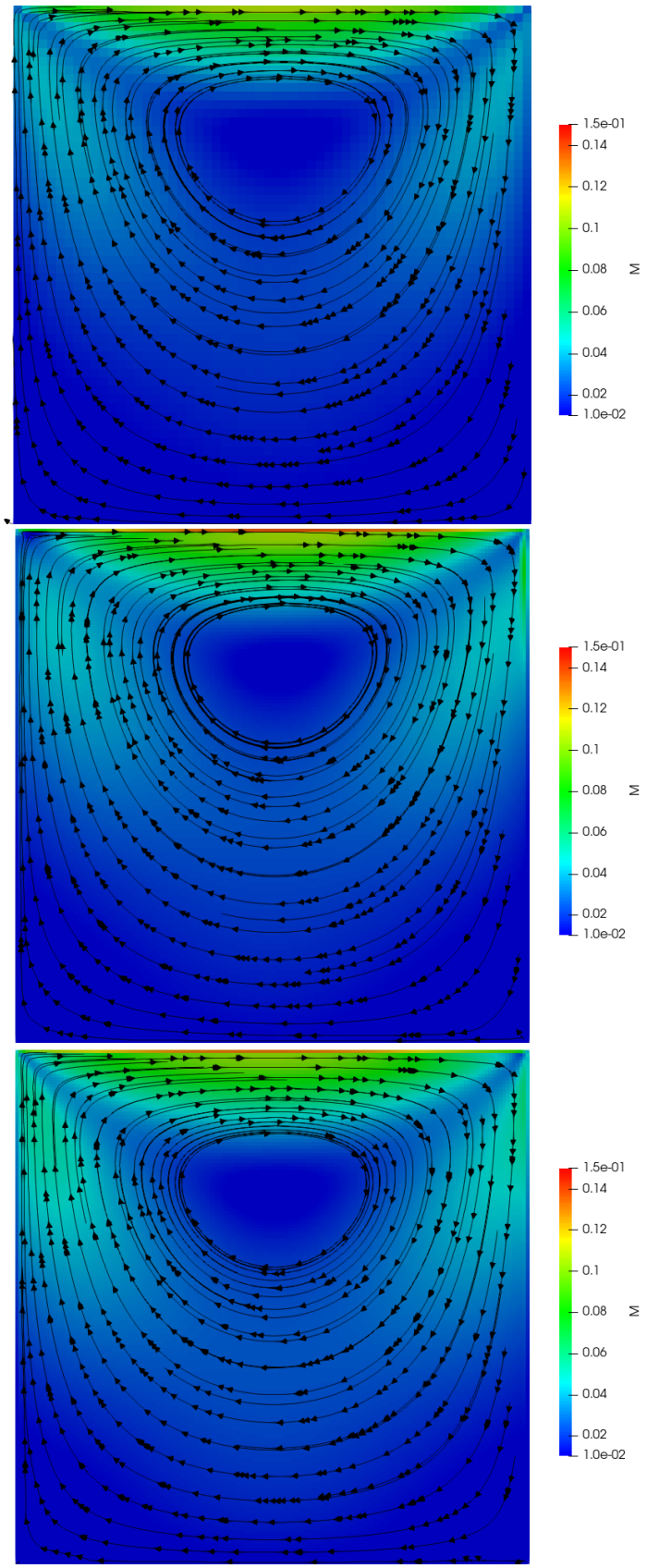

Figure 8.10: Mach number contour for the lid-driven cavity flow at $Kn = 0.1$ for DSMC (top), 14-moment closure (middle) and 21-moment closure (bottom).

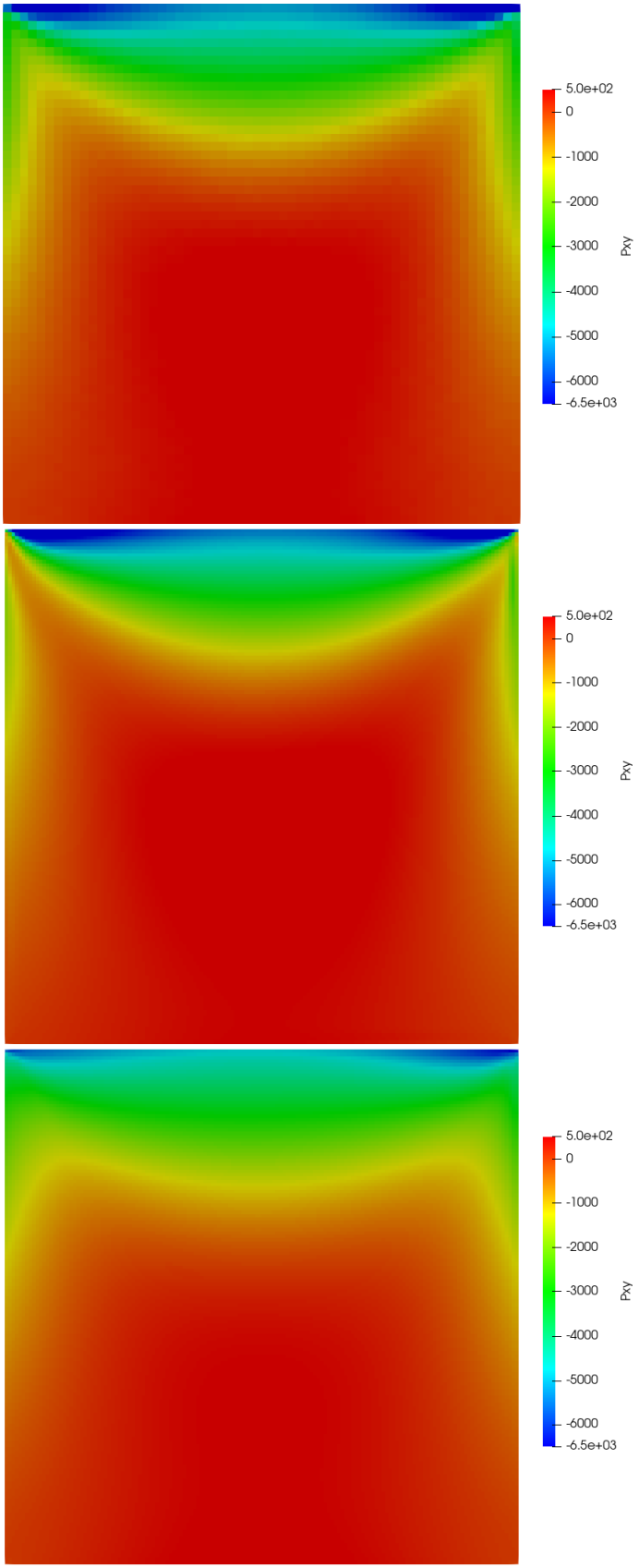

Figure 8.11: P_{xy} contour for the lid-driven cavity flow at $Kn = 0.1$ for DSMC (top), 14-moment closure (middle) and 21-moment closure (bottom).

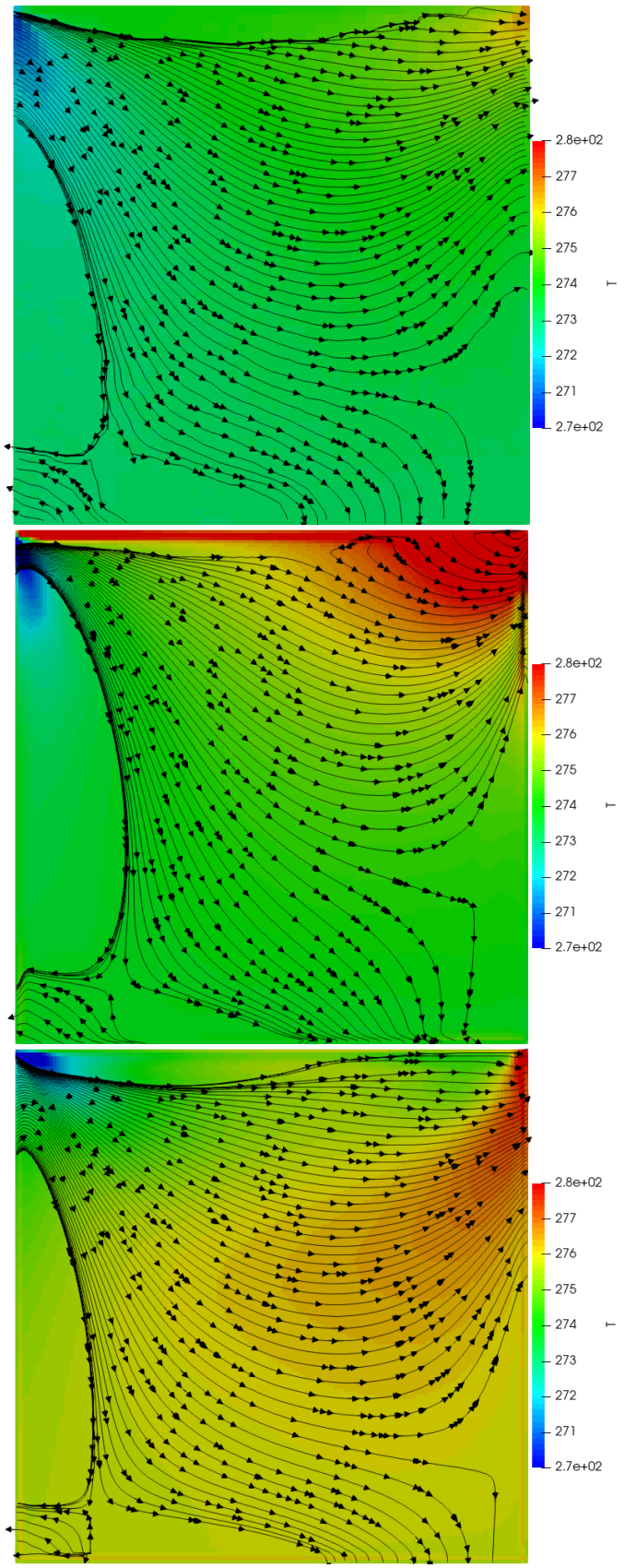

Figure 8.12: Temperature contour with heat-transfer streamline for the lid-driven cavity flow at $Kn = 0.1$ for DSMC (top), 14-moment closure (middle) and 21-moment closure (bottom).

Chapter 9

Conclusion

9.1 Summary

In this work, an approximation for the closing fluxes of the 21-moment model from maximum-entropy is proposed. The previous fourteen-moment approximation has a poor fit for the heat-flux tensor. By moving to twenty-one moments, the full heat-flux tensor is added to the solution vector. This leads to a far superior approximation to the maximum-entropy closure. In computing a stationary shock profile, the proposed model has shown to predict the solution more accurately than the Navier-Stokes equation. It also showed to be in very good agreement with the prediction obtained from directly solving the BGK equation. When computing the lid-driven cavity case, non-equilibrium effects were recovered in agreement with the DSMC solution. A reverse heat-transfer, contradicting Fourier's law, was observed.

Although the proposed approximation is shown to be robust and stable, it, unfortunately, does not present global hyperbolicity through all moment space. Furthermore, the necessity to numerically compute the associated eigenvalues at every timesteps renders the proposed model expensive in computation time. Finally, as explained, issues with the solid-wall boundary condition take away from the accuracy of the solution computed with higher-order maximum-entropy closures.

9.2 Future Work

Some future advancements could be undertaken to provide significant improvement to the proposed model. An approximation for the eigenvalue of the model would provide much lower computation time. This is even more important if three-dimensional cases are to be computed. Also, the development of a more accurate method for the description of solid-wall boundary condition would provide more physical accuracy to the solution. Finally, the development of a Roe average [37] for the 21-moment model would allow the use of superior more accurate flux functions.

Bibliography

[1] M. R. A. Abdelmalik and E. H. van Brummelen. Moment closure approximations of the boltzmann equation based on φ-divergences. *J. Stat. Phys.*, 164, 2015.

[2] T. J. Barth. On discontinuous Galerkin approximations of boltzmann moment systems with Levermore closure. *Comp. Meth. Appl. Mech. Engrg.*, 195:3311–3330, 2006.

[3] P. L. Bhatnagar, E. P. Gross, and M. Krook. A model for collision processes in gases. I. small amplitude processes in charged and neutral one-component systems. *Physical Rev.*, 94(3):511–525, 1954.

[4] G. A. Bird. *Molecular Gas Dynamics and the Direct Simulation of Gas Flows*. Clarendon Press, Oxford, 1994.

[5] L. Boltzmann. Weitere studien über das wärmegleichgewicht unter gasmolekülen. *Sitz. Math.-Naturwiss. Cl. Akad. Wiss. Wien*, 66:275–370, 1872.

[6] S. L. Brown. *Approximate Riemann Solvers for Moment Models of Dilute Gases*. PhD thesis, University of Michigan, 1996.

[7] S. L. Brown, P. L. Roe, and C. P. T. Groth. Numerical solution of a 10-moment model for nonequilibrium gasdynamics. Paper 95-1677, AIAA, June 1995.

[8] Z. Cai, Y. Fan, and R. Li. Globally hyperbolic regularization of Grad's moment system in one dimensional space. *Commun. Math. Sci.*, 11(2):547–571, 2013.

[9] Z. Cai, Y. Fan, and R. Li. Globally hyperbolic regularization of Grad's moment system.

Commun. Pure Appl. Math., 67(3):464–514, 2014.

[10] Z. Cai, Y. Fan, and R. Li. On hyperbolicity of 13-moment system. *Kinetic and Related Models*, 7:415 – 432, 2014.

[11] W. Dreyer. Maximization of the entropy in non-equilibrium. *Journal of Physics A: Mathematical and General*, 20:6505–6517, 1987.

[12] R. O. Fox and F. Laurent. Hyperbolic quadrature method of moments for the one-dimensional kinetic equation. *SIAM J. Appl. Math.*, 82(2):750–771, 2022.

[13] S. K. Godunov. An interesting class of quasilinear systems. *Sov. Math. Dokl.*, 2:947–949, 1961.

[14] T. I. Gombosi. *Gaskinetic Theory*. Cambridge University Press, Cambridge, 1994.

[15] H. Grad. On the kinetic theory of rarefied gases. *Commun. Pure Appl. Math.*, 2:331–407, 1949.

[16] C. P. T. Groth and J. G. McDonald. Towards physically-realizable and hyperbolic moment closures for kinetic theory. *Continuum Mech. Thermodyn.*, 21(6):467–493, 2009.

[17] H. L. Hamburger. Hermitian transformations of deficiency-index $(1, 1)$, jacobian matrices, and undetermined moment problems. *Amer. J. Math.*, 66:489–552, 1944.

[18] A. Harten. High resolution schemes for hyperbolic conservation laws. *J. Comput. Phys.*, 49:357–393, 1983.

[19] A. Harten, P. D. Lax, and B. van Leer. On upstream differencing and Godunov-type schemes for hyperbolic conservation laws. *SIAM Rev.*, 25(1):35–61, 1983.

[20] J. A. Hittinger. *Foundations for the Generalization of the Godunov Method to Hyperbolic Systems with Stiff Relaxation Source Terms*. PhD thesis, University of Michigan, 2000.

[21] B. John, X.-J. Gu, and D. R. Emerson. Investigation of heat and mass transfer in a lid-driven cavity under nonequilibrium flow conditions. *Numer. Heat Trans.*, 58:287–303,

2010.

[22] B. John, X.-J. Gu, and D. R. Emerson. Effects of incomplete surface accommodation on non-equilibrium heat transfer in cavity flow: A parallel dsmc study. *Computers and Fluids*, 45:197–201, 2011.

[23] M. Junk. Domain of definition of Levermore's five-moment system. *J. Stat. Phys.*, 93(5/6):1143–1167, 1998.

[24] M. Junk and A. Unterreiter. Maximum entropy moment systems and Galilean invariance. *Continuum Mech. Thermodyn.*, 14:563–576, 2002.

[25] W. Kaufmann. Extended hydrodynamics using the discontinuous-galerkin hancock method. Master's thesis, University of Ottawa, August 2021.

[26] L. Khieu, B. van Leer, and Y. Suzuki. An analysis of a space-time discontinous-Galerkin method for moment equations and its solid-boundary treatment. Paper 2009–3874, AIAA, June 2009.

[27] J. Köllermeier and M. Torrilhon. Numerical study of partially conservative moment equations in kinetic theory. *Commun. Comput. Phys.*, 21:981–1011, 2017.

[28] C. D. Levermore. Moment closure hierarchies for kinetic theories. *J. Stat. Phys.*, 83:1021–1065, 1996.

[29] D. Marchisio and R. Fox. *Computational Models for Polydisperse Particulate and Multiphase Systems*. Cambridge University Press, Cambridge, 2013.

[30] J. G. McDonald, J. S. Sachdev, and C. P. T. Groth. Gaussian moment closure for the modelling of continuum and micron-scale flows with moving boundaries. In H. Deconinck and E. Dick, editors, *Proceedings of the Fourth International Conference on Computational Fluid Dynamics, ICCFD, Ghent, Belgium, July 10–14, 2006*, pages 783–788, Heidelberg, 2009. Springer-Verlag.

[31] J. G. McDonald and M. Torrilhon. Affordable robust moment closures for CFD based on the maximum-entropy hierarchy. *J. Comput. Phys.*, 251:500–523, 2013.

[32] R. McGraw. Description of aerosol dynamics by the quadrature method of moments. *Aerosol Science and Technology*, 27(2):255–265, 1997.

[33] L. Mieussens. Discrete velocity model and implicit scheme for the BGK equation of rarefied gas dynamics. *Mathematical Models and Methods in Applied Sciences*, 10(8):1121–1149, 2000.

[34] S. Mizzi, X. J. Gu, D. R. Emerson, R. W. Barber, and J. Reese. Computational framework for the regularized 20-moment equations for non-equilibrium gas flows. *Int. J. Numer. Meth. Fluids*, 56:1433–1439, 2008.

[35] I. Müller. *Thermodynamics*. Pitman Publishing, Boston, 1985.

[36] I. Müller and T. Ruggeri. *Extended Thermodynamics*. Springer-Verlag, New York, 1993.

[37] P. L. Roe. Approximate Riemann solvers, parameter vectors, and difference schemes. *J. Comput. Phys.*, 43:357–372, 1981.

[38] H. Struchtrup. *Macroscopic Transport Equations for Rarefied Gas Flows*. Springer-Verlag, Berlin, 2005.

[39] H. Struchtrup and M. Torrilhon. Regularization of Grad's 13 moment equations: Derivation and linear analysis. *Phys. Fluids*, 15(9):2668–2680, 2003.

[40] Y. Suzuki. *Discontinuous Galerkin Methods for Extended Hydrodynamics*. PhD thesis, University of Michigan, 2008.

[41] Y. Suzuki and B. van Leer. Application of the 10-moment model to MEMS flows. Paper 2005-1398, AIAA, January 2005.

[42] B. R. Tensuda, J. G. McDonald, and C. P. T. Groth. Multi-dimensional validation of a maximum-entropy-based interpolative moment closure. *AIP Conference Proceedings*, 1786(1):14008, 2016.

[43] M. Torrilhon. Convergence study of moment approximations for boundary value problems of the boltzmann-bgk equation. *Communications in Computational Physics*,

18(3):529557, 2015.

[44] C. Tsallis. *Introduction to Nonextensive Statistical Mechanics*. Springer, New York, 2009.

[45] W. G. Vincenti and C. H. Kruger. *Introduction to Physical Gas Dynamics*. R. E. Krieger Publishing, Huntington, NY, 1975.

[46] C. Yuan and R. Fox. Conditional quadrature method of moments for kinetic equations. *Journal of Computational Physics*, 230(22):8216–8246, 2011.

[47] C. Yuan, F. Laurent, and R. Fox. An extended quadrature method of moments for population balance equations. *Journal of Aerosol Science*, 51:1–23, 2012.